Magnetism and interactions within the single domain limit: reversal, logic and information storage

Zheng Li

A dissertation

Submitted in partial fulfillment of the requirement for the degree of

Doctor of Philosophy

University of Washington

2015

Reading Committee:

Dr. Kannan M. Krishnan, Chair

Dr. Karl F. Bohringer

Dr. Marjorie Olmstead

Program Authorized to Offer Degree:

Materials Science & Engineering

ABSTRACT

Magnetism and interactions within the single domain limit:

reversal, logic and information storage

Zheng Li

Chair of the Supervisory Committee:

Dr. Kannan M. Krishnan

Materials Science & Engineering

Magnetism and magnetic material research on mesoscopic length scale, especially on the size-dependent scaling laws have drawn much attention. From a scientific point of view, magnetic phenomena would vary dramatically as a function of length, corresponding to the multi-single magnetic domain transition. From an industrial point of view, the application of magnetic interaction within *the single domain limit* has been proposed and studied in the context of magnetic recording and information processing. In this thesis, we discuss the characteristic lengths in a magnetic system resulting from the competition between different energy terms. Further, we studied the two basic interactions within *the single domain limit*: dipole interaction

and exchange interaction using two examples with practical applications: magnetic quantum-dot cellular automata (MQCA) logic and bit patterned media (BPM) magnetic recording.

Dipole interactions within the single domain limit for shape-tuned nanomagnet array was studied in this thesis. We proposed a 45° clocking mechanism which would intrinsically eliminate clocking misalignments. This clocking field was demonstrated in both nanomagnet arrays for signal propagation and majority gates for logic operation. Correct output and robust performance were detected for both configurations. Further, more complicated design, two digital binary full adder, was carried out. This novel design provides high stability for logic operation of MQCA and potentially paves way for its application.

In addition, the magnetization reversal in perpendicular magnetic anisotropy (PMA) system and its dependence on scaling law were studied. High quality epitaxial $L1_0$ FePdPt and FePt thin films on MgO (001) substrate was fabricated. For FePd binary alloy thin films, we observed that Pt addition and low temperature post annealing would facilitate $L1_0$ chemical ordering. For FePt thin film samples, reversal process and magnetic behavior were studied for both continuous film and patterned dots array. Further, patterned dots arrays within different length scale were developed to reveal the multi/single domain transition, which is observed to be around 200 nm for our $L1_0$ FePt thin film. Finally, sub-100 nm dots array in a large area was carried out for both $L1_0$ FePt monolayer and FePt/Co bilayer heterostructure. The high patterning quality was demonstrated in the uniform dot size distribution, and the magnetic properties of the dots array indicates a good candidate for the application of bit-patterned media (BPM) exchange coupled composite (ECC) magnetic recording.

ACKNOWLEDGEMENTS

I would like to thank Professor Kannan Krishnan for giving me the opportunity to join his group and work in the exciting field of nanomagnetic materials. His support and guidance have always been critical for me to make progress and get to be the man I am today. Michelangelo once said, *every block of stone has a statue inside it and it is the task of the sculptor to discover it*. Professor Krishnan is one of the most remarkable and important sculptors in my life. I feel grateful every day to have the opportunity to work with him and learn from him during the last 5 years.

Also, I would like to thank my committee members, Prof. Jihui Yang, Prof. Karl Bohringer, and Prof. Marjorie Olmstead, for their time and insight, which helped to make this work complete. For helpful technical guidance of this project, I want to thank Dr. Wei Zhang and Dr. Yufeng Hou; for help with measurements and technical advice, many thanks are owed to my collaborators, Dr. Mark Bowden, Prof. Alexandru Stancu, Prof. Vaithiyalingam Shutthanandan *et al*. My group colleagues have also given me tremendous help in the past five years. I want to express the same gratitude to them, especially Dr. Matt Ferguson, Dr. Tianlong Wen, Dr. Amit

Khandhar, Byung Seok Kwon, Mark Brunson, Hamed Arami, Olivia Lenz, Eric Teeman and Ryan Hufschmid, for their helpful suggestions and support.

Part of this work was conducted at the Washington Nanofabrication Facility / Molecular Analysis Facility, a National Nanotechnology Coordinated Infrastructure (NNCI) site at the University of Washington, which is supported in part by funds from the Molecular Engineering & Sciences Institute, the Clean Energy Institute, the Washington Research Foundation, the M. J. Murdock Charitable Trust, the National Science Foundation and the National Institutes of Health.

Finally, my deepest appreciation belongs to my family. Without their unconditional support through the years, I would not have been able to go this far.

TABLE OF CONTENTS

Chapter 1

INTRODUCTION, BACKGROUND, AND MOTIVATION

1.1 Size-dependent scaling law

Magnetism and magnetic material research on mesoscopic length scale has met a rapid increase in recent years, owing to the discovery of new phenomena [A1,A2], development in fabrication [A3] and advance in characterizations [A4]. Based on the size-dependent scaling laws, novel architectures [A5] and devices [A6] have been proposed, designed and characterized, especially in the form of magnetic thin films. Most notably, the interplay between size and fundamental physical correlation, such as proximity effect [A7], exchange coupling effect [A8], dipole interaction [A9] and interfacial coupling [A10], plays a key role in both scientific study [A11] and technology application [A12]. In all these cases, some phenomena dominate at certain size and vanish on other length scale. For example, the Ruderman-Kittel-Kasuya-Yosida (RKKY) effect [A13], referring to a coupling mechanism of magnetic moments, may fade out rapidly when the two interacting elements are separated by several nanometers; while the dipole interaction remains in long range. Thus, to explore new phenomena and enable new science, a

comprehensive study of the size-dependent scaling laws and related magnetization and magnetic behavior is required.

1.2 Intrinsic characteristic length

Several types of interactions together determine the magnetic configuration of elements. One of them is exchange interaction, which states that adjacent spins or local magnetic moments would couple in order to achieve parallel alignment of the spins in ferromagnetic materials. The corresponding exchange energy, E_{ex}, would be minimized where exchange interaction dominates. The schematic of exchange coupling is shown in fig 1.1(a). Reduction of E_{ex} requires parallel alignment which may locally increase other types of energy, such as magnetostatic energy and anisotropy energy [A14], as will be discussed below.

Second, magnetostatic energy, E_{ms}, comes from dipole interaction through the magnetostatic fields, which are caused by the magnetic moments. This interaction favors anti-parallel aligned magnetic moments. Dipole interaction plays a major role in longer distance and with weaker strength than exchange interaction does. As shown in fig 1.1(b), the magnetic state of an element could break down to multi-domains if E_{ms} dominates.

Besides, anisotropy energy, E_a, is corresponding to certain directions or axis that are energetically more favorable for the magnetic moment to rest, possibly caused by either element shape asymmetry or material crystalline structure. In summary, the competition between these different energy terms results in several characteristic lengths for magnetic elements; some of them are related to the intrinsic properties of a given material, while others would depend on the processing.

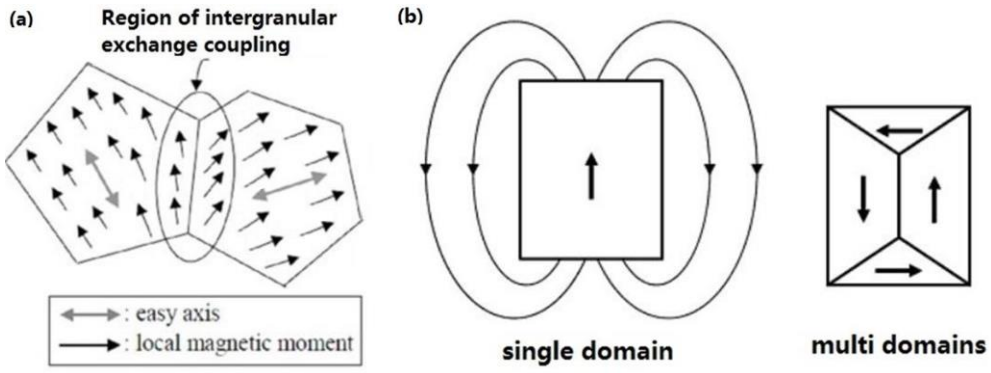

Fig 1.1 (a) Schematic of exchange coupling. E_{ex} exists at the interface where the local magnetic moments are not aligned at the same direction. (b) Transition of magnetization state depending on the exchange length. The left one (*size* $D < L_{ex}$) managed to minimize E_{ex}; the right one ($D > L_{ex}$) favors magnetostatic energy.

The first intrinsic characteristic length is the exchange length, L_{ex}, resulting from the competition between exchange energy, E_{ex}, and E_{ms} (or E_a). It can be expressed as

$$L_{ex} \approx \sqrt{A/K} \ldots\ldots (1.1)$$

where $A = 10^{-6}$ ergs/cm is the exchange constant, representing the spacial spin interactions. The anisotropy constant, K, comes from the magnetostatic energy, equal to $2\pi M_S^2$ in the Gaussian unit system (as will be used in the rest of this thesis) [A15], where M_S represents the saturation magnetization of the material, or the material itself, or even both of them. In a few words, the exchange length represents a correlation length of the ferromagnetic interaction in a magnetic system that manages to minimize its exchange energy. Let us take polycrystalline permealloy nanowire as an example. When the wire's width exceeds L_{ex}, dipole interaction would dominate, leading to an inhomogeneous switching where magnetic moments reverse sequentially in favor of E_{ms} [A16].

The second intrinsic characteristic length is magnetic domain wall width, D_{dw}. Similar to exchange length, domain wall width has an expression of

$$D_{dw} \approx \pi\sqrt{A/K} = \pi\, L_{ex} \ldots\ldots (1.2)$$

where A and K are defined the same as in equation(1.1). A domain wall (DW) is an interface that separates different magnetic domains through an angular displacement of the spin orientation, usually 90° or 180°. The spacial size of the angular displacement determines the DW width. On one hand, E_{ex} favors a wide DW since it prefers spins to be parallel; on the other hand, anisotropy energy prefers a narrow DW, since it favors spins to have a specific alignment relative to the sample or crystal structure. As a consequence, the system settles at the balance state where domain wall energy, $E_{dw} = E_{ex}+E_a$ is minimized at

$$E_{dw}(\min) = 4\sqrt{AK} \ldots\ldots (1.3)$$

Domain walls are divided into two catogories: Néel wall and Block wall, as shown in fig 1.2. More details will be discussed in chapter 4.

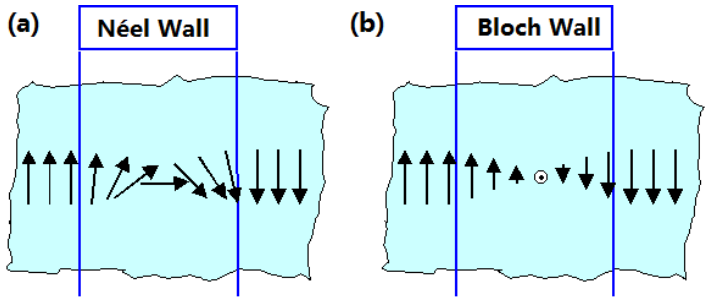

Fig 1.2 Schematic of (a) Néel domain wall and (b) Block domain wall. Néel wall lies within the plane of the wall while Block wall is out of the plane of the wall

The third intrinsic characteristic length is the single domain particle size, or the *single domain limit*, D_{sd}. As the size of magnetic elements reduces, single domain becomes energetically more favorable than the multi-domain state. The transition occurs when the magnetostatic energy, E_{ms}, and domain wall energy, E_{dw}, are comparable to each other; the corresponding characteristic length is called the *single domain limit*. It can be expressed [A17] as

$$D_{sd} = 1.4\frac{E_{dw}}{{M_s}^2} = 5.6(\frac{\sqrt{AK}}{{M_s}^2})\ldots\ldots(1.4)$$

where E_{dw} and M_s represent the domain wall energy and saturation magnetization, respectively. Table 1.1 is a chart of magnetic parameters for different materials of Fe, Co, $L1_0$ (face centered tetragonal, *fct*) FePd and FePt.

Tab 1.1 (Adapted from ref A17) Magnetic parameters of amorphous Fe, Co and $L1_0$ FePd, FePt.

	K_1[a] (10^7ergs/cc)	M_s (emu/cc)	L_{ex}[b] (nm)	D_{dw} (nm)	E_{dw} (ergs/cm^2)	D_{sd} (nm)
Fe	--	1714	2.4	7.5	16.7	10
Co	--	1414	3.4	10.7	11.7	56
$L1_0$ FePd	1.8	1100	2.4	7.5	17	200
$L1_0$ FePt	6.6	1140	1.2	3.9	32	340

[a] K_1 and M_S stand for the uniaxial anisotropy and saturation magnetization at room temperature (300 K), respectively. [b] L_{ex}, D_{dw}, E_{dw} and D_{sd} are calculated by expressions above using $A = 10^{-6}$ ergs/cm

1.3 Structural characteristic lengths

Other than the intrinsic characteristic lengths, there are several structural characteristic lengths that are also important in understanding the size-dependent scaling law. They rely not only on the intrinsic material properties, but are also dependent on the processing, such as the deposition, nanofabrication and annealing. One example is the dimensionality effects on the

magnetic reversal in a FePt wire [A11]. The mean distance between pinning defects within a FePt thin film is called *disorder length*. For narrow FePt wires with width smaller than *disorder length*, the available paths for DW propagation would be suppressed, forcing DW to cross the pinning defects one by one. The pinning defects have reversal field higher than normal, and thus the overall coercivity (H_c) would increase. Besides pinning defects that comes from thin film deposition process, edge roughness, which is attributed to the nanofabrication process, would also affect the magnetic reversal in a lithographically patterned element. The *mean edge roughness* reveals the roughness of pattern edges and raises the coercivity when it is comparable to patterning feature size. The comparison between *disorder length* and *mean edge roughness* is shown in figure 1.3. In a word, the size-dependent scaling law is determined by the combination of both intrinsic material properties and the processing.

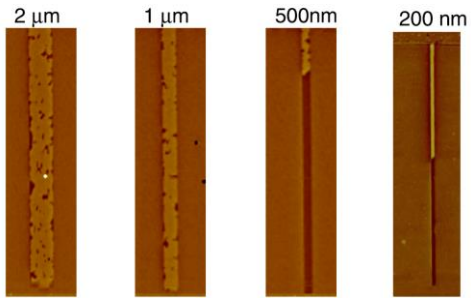

Fig 1.3 (adapted from ref A11) Comparison between *disorder length* and *mean edge roughness* by magnetic force microscopy (MFM), where the contrast indicates magnetic domains oriented in opposite directions. The magnetic reversal process in the FePt wires changes with the width, *w*, of the wires; for wide wire (w > 500 nm), it is in a uniform manner, while propagation of a single DW dominates in narrow wires.

1.4 Single domain limit

Among all these characteristic lengths, the *single domain limit* is of the most interest. From a scientific point of view, down-scaling the size of magnetic elements to the *single domain*

limit would fundamentally change the magnetization reversal process. Magnetic elements within the *single domain limit* would experience the reversal as a coherent rotation of all magnetic moments, that exchange interaction would hold all magnetic moments parallel to each other all the time. The magnetic reversal within such a system is best described by the well-known Stoner-Wohlfarth model [A18].

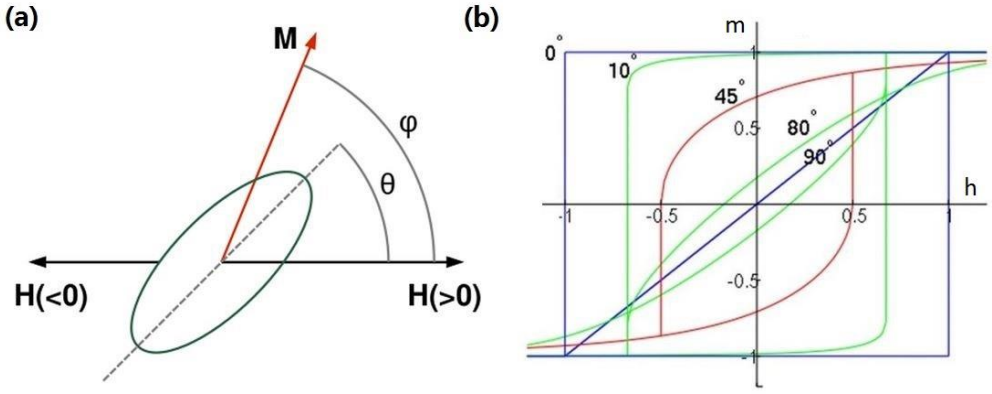

Fig 1.4 (Adopted from Wikipedia) (a) Illustration of the variables used in the Stoner–Wohlfarth model. The dashed line is the easy axis of the element. (b) Angular dependence of the hysteresis loop, with the minimized H_{sw} reached at θ =45°. In fig b, *m* and *h* represent the normalized magnetization and applied field against saturation magnetization and coercivity at θ = 0°, respectively.

In the Stoner−Wohlfarth model, the magnetization is assumed to remain uniform within the element and is represented by a vector, ***M***. It rotates as the magnetic field, *H*, varies along a specific axis with an angle, θ, off the easy axis of the element. As the magnetic field varies, the magnetization is represented by the angle between the magnetization and the field, φ, as shown in fig 1.4(a) [A19]. The energy of the system is expressed as

$$E = K_1 V sin^2(\varphi - \theta) - M_s V H cos\varphi \ldots\ldots (1.5)$$

where V and K_1 represent the volume of the element and the uniaxial anisotropy, respectively. The first term is the magnetic anisotropy energy, E_a; while the second one represents the Zeeman energy, $-\vec{M} \cdot \vec{H}$, when an external magnetic field is applied. The magnetization direction, φ, is determined by the equilibrium state due to the competition between both energy terms. Mathematically, the first derivative of the energy with respect to φ should be zero whilst its second derivative should be positive to be stable against perturbations at the equilibrium state. Therefore, a series of hysteresis loops could be drawn as a function of θ. It is worth mentioning that the θ-dependence of the switching field H_{sw} follows the so-called Stoner-Wohlfarth astroid, where the minimized H_{sw} value could be reached at $\theta = 45°$ [fig 1.4(b)], Application of the Stoner-Wohlfarth astroid will be discussed in more details in chapter 3.

Besides the scientific interests to study magnetism within the single domain limit, the technological imperatives are also clear. In recent years, magnetic phenomena within the single domain limit have been exploited for both logic functionality [A6] and information storage [A9] using different lithographically defined nanostructures. Two of the most significant applications and related motivations for the pursuit of single domain limit will be discussed below.

1.5 MQCA logic

To help realize logic functionality using lithographically patterned nanostructures is the concept of Magnetic Quantum-dot Cellular Automata (MQCA) [A20], which aims to process information and perform Boolean logic operations via nearest-neighbor dipole coupling of nano-elements in a coordinative arrangement, as shown in fig 1.5(a). The nano-sized elements are tailored to be within their *single domain limit* in order to ensure a coherent rotation for the

magnetic reversal. MQCA logic has many advantages over conventional Si CMOS technology, such as low heat dissipation, non-volatility and high integration density.

There are two basic MQCA architectures: (a) *nanomagnet arrays* where the signal propagates, and (b) *majority gates* where logic operates through a 3-input voting mechanism. Figure 1.5(b) shows the schematic of these two basic architectures. For both architectures, a clocking field is required to bring the elements to their NULL state such that (i) the magnetization aligns along the hard axis [fig 1.5(c)]. After the field is removed, the elements would (ii) rest into one of the two ground states (either 0 or 1, as predefined by the magnetic state of either up or down) when triggered by the adjacent element through dipole coupling. This process is further illustrated in fig 1.5(d). The clocking field provides the energy so that the element can switch between two local grounding states in spite of the barrier introduced by the shape anisotropy. The dipole interaction would ensure that the element falls into the global grounding state, which favors antiparallel alignment with the adjacent magnetic moments. In practice, however, it has been reported that a field misalignment of ±1° would lead to incorrect logic operation 75% of the time, and makes such MQCA logic practically challenging [A20].

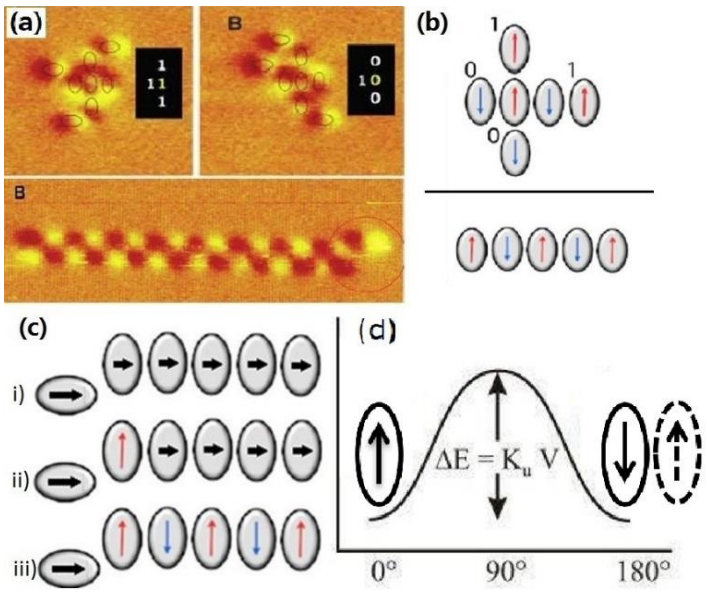

Fig 1.5 (a) (adapted from ref A-20) MQCA logic examples. The upper majority gates perform logic operation, and the lower nanowire shows signal propagation. (b) Two basic MQCA architectures where the arrows indicates the magnetic state of elements. (c) Schematic of the clocking process. The field aligns magnetization of all elements along their hard axis (NULL state) (i) is then removed, allowing signal to propagate (ii, iii). (d) The energy barrier ΔE defined by the shape anisotropy, K_1, and the volume, V, of the element. When a clocking field is removed, the magnetization will fall to the ground state favoring the dipole interaction with adjacent elements.

To overcome this limitation, many approaches have been tested to enhance the stability. For example, a biaxial anisotropy is proposed to enhance the hard axis stability [A21], as shown in fig 1.6(a). Alternatively, different shaped nanomagnets, such as S-shaped [A22], edge-slanted [A23], and concaved [A24] elements, have been examined [fig 1.6 (b)-(d)]. These designs facilitate signal propagation to some extent, in that the energy barrier between two ground states is modified in favor of logic operation in multiple clocking cycles. However, they all rely on a high accuracy of field alignment. As a result, a further study on the MQCA logic and dipole interaction in the single domain limit is desired to establish a misalignment-free mechanism with high tolerance and robust logic performance.

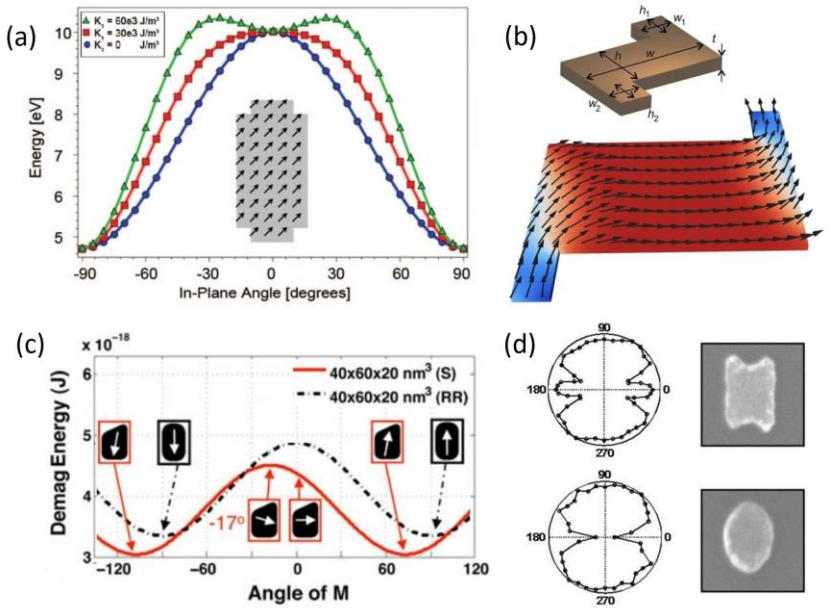

Fig 1.6. (Adapted from ref A21-A24) (a) The modified energy barrier showing that biaxial anisotropy is introduced in the patterned element to enhance the hard axis stability, (b) S-shaped, (c) edge-slanted and (d) concaved magnetic elements facilitating signal propagation in different manners. All of these established designs rely on a high accuracy of clocking field alignment.

To solve this problem, we propose and demonstrate a novel architecture— a reversal clocking mechanism with field direction at 45° off the hard axis of the element. This 45° mechanism, as will be discussed in detail in chapter 3, combines a progressively tuned shape anisotropy of elements and enforces both signal propagation and logic operation. It intrinsically enhances the misalignment tolerance, resulting in robust signal propagation and logic operation.

Further study of MQCA logic requires more complicated functions, such as full adder, in order to achieve both integration with electrical circuit and efficient data management [A25]. A binary full adder works to add up binary numbers and accounts for values carried in/ out [A26]. Although it is straightforward to design such a MQCA full adder based on blocks of *nanomagnet arrays* and *majority gates*, there are few experimental attempts due to the misalignment issue

[A26-A29]. As shown in fig 1.7, for example, error in data-flow directionality occurs, because the clocking misalignment triggers the elements in later clocking stage to flip early [A27]. Thus, it is of interest to redesign a full adder that is stable against clocking misalignment.

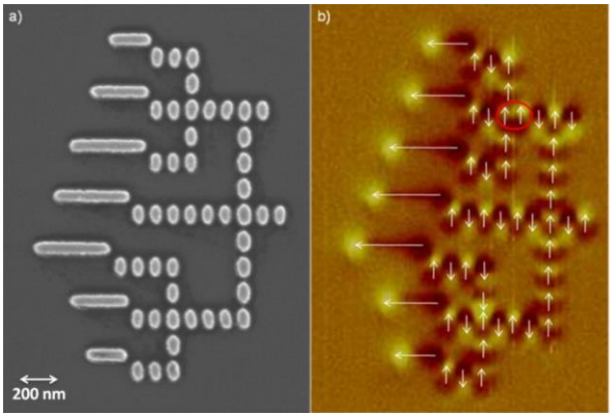

Fig 1.7 (Adapted from ref A27) Traditional design for full adder: (a) SEM image and (b) MFM image. The red circle highlights the failure in logic operation due to the clocking field misalignment.

To achieve a robust performance of a MQCA adder, we demonstrates a novel architecture of 3-input full adder based on 45° clocking mechanism, as will be discussed in *chapter 3*. The field alters between 0° and 45°-off the hard axis to separate input writing from logic operation. This novel clocking mechanism facilitates stable logic operations. Further, it favors unidirectional signal flow and hence requires only 1/3 the number of elements of a traditional full adder design [A27].

1.6 PMR recording

The concept of utilizing materials with perpendicular magnetic anisotropy (PMA) for superhigh density magnetic recording [A30][A31] has been tantalizing researchers for decades [A32-A35]. Compared to the traditional *longitudinal recording* where the magnetic moments stay in the

plane of the recording disc, the *perpendicular magnetic recording* (PMR) has several advantages (fig 1.8), because of the nature that the magnetic moments rest perpendicular to the disc plane. First, the demagnetizing field for the longitudinal recording is largest in the transition region, the domain wall between adjacent bits of information, and it causes the transition jitter (the deviation of transition location); while perpendicular recording is advantageous in giving a sharp transitions [A36]. Further, the transition width of PMA recording media is determined by the grain size and is independent of material properties [A37], suggesting a higher areal density.

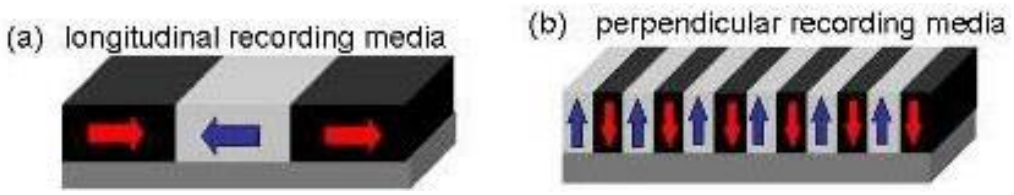

Fig 1.8 Comparison between longitudinal (a) and perpendicular (b) recording from a media point of view.

From a media point of view, PMR requires stable magnetic properties. For example, a robust performance of recording media is desired against thermal fluctuation in that either the size of grains be large enough or the anisotropy be high enough against the so-called *superparamagnetic limit*. The *superparamagnetic limit* defines the energy barrier for single grains required to prevent the spontaneous reversal due to thermal fluctuation. As a result, higher magnetocrystalline anisotropy, K_1, is required for higher recording density in order to maintain a constant energy barrier [A38][A39].

Among all the promising candidates that have high K_1, the $L1_0$ epitaxial systems (such as FePt and FePd), with the *c*-axis of the tetragonal unit cell being the easy axis of magnetization, have generated most interest [A40-A42]. Take $L1_0$ FePt as an example: it has $K_1 = 6.6\times10^7$ ergs/cc at

room temperature (300 K) [A43]. Normally deposited at elevated temperatures (780°C for $L1_0$ FePd, for instance [A41]) they are not efficient for mass production; further, high-temperature growth may lead to larger grain size, thus lower potential recording density [A44]. In response, different methods, such as ion bombardment [A44,A46] and the addition of a third element [A47-A51], have been proposed to lower the growth temperature. Although several additive elements, such as Zr [A47], Cu [A48,A50], Ni [A49] and Cr [A51], have been examined in the literature, materials with properties similar to FePt, such as $L1_0$ FePd (K_1=1.8×10^7 ergs/cc; M_S=1100 emu/cc [A44]), draw little attention. For example, $L1_0$ FePd has a lower ordering temperature as well as relative inexpensive price, both of which make it advantageous over FePt for recording media [A52]. Only a few studies of $L1_0$ FePd films and even fewer of $L1_0$ FePdX ternary system [A53,A54] have been reported. In light of that, we studied the FePd binary system with Pt additions (~5 atomic %) in this thesis. We observed that the addition leads to a better chemical ordering and perpendicular anisotropy using advanced magnetic measurement methods, such as first order reversal curve (FORC) diagrams [A55,A56], details of which can be found in Appendix-1.

However, utilizing PMA materials for even higher density magnetic recording (>5 Tb/in^2) has become more and more challenging, because the projected upper limit of ~1 Tb/in^2 is expected to be reached soon due to the *trilemma of magnetic recording* [A57]. What is the *trilemma of magnetic recording*? As discussed above, the *superparamagnetic limit* demands an increase in magnetocrystalline anisotropy as a compensation for higher recording density and smaller grain size. However, higher K_1 would accordingly result in a higher switching field which will eventually meet the limit of the writing head capability of about 10 kOe [A57]. These three factors of grain size, anisotropy and writability together contribute to the so-called *trilemma of magnetic recording*, as illustrated in fig 1.9.

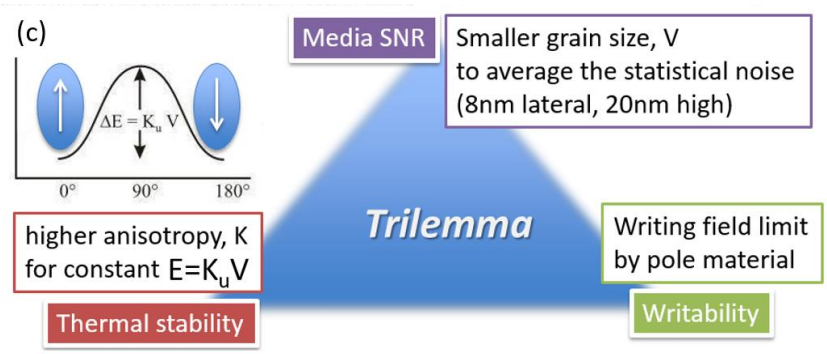

Fig 1.9 Illustration of the *trilemma of magnetic recording*. Higher areal density requires smaller grain size, which is associated with an increase in anisotropy constant and media coercivity, which triggers a larger writing field. Unfortunately, the maximum field a writing head can generate is limited by the current technology. The trilemma of magnetic recording provides an upper limit for the recording density of 1 Tb/in^2 [A57].

To overcome this trilemma, several approaches have been proposed, including heat-assisted magnetic recording (HAMR) [A58], exchange-coupled composite (ECC) [A59] media and bit-patterned media (BPM) [A60]. HAMR uses a short pulse of laser to heat up the recording media locally in order to lower the switching field within the capability of the writing head [A58]. After the writing process is finished, the heat dissipates rapidly and the local magnetic state remains stable because of the high anisotropy at room temperature. On the other hand, ECC media achieves the reduction in switching field by introducing a heterostructure of soft/hard magnetic multilayers [A59]. During the writing process, the field first reverses the soft magnetic layer with lower H_c, which then exerts a torque on the hard magnetic layer through interface exchange coupling. As a result, a lower writing field is achieved. Figure 1.10 shows the schematic of both HAMR and ECC recording.

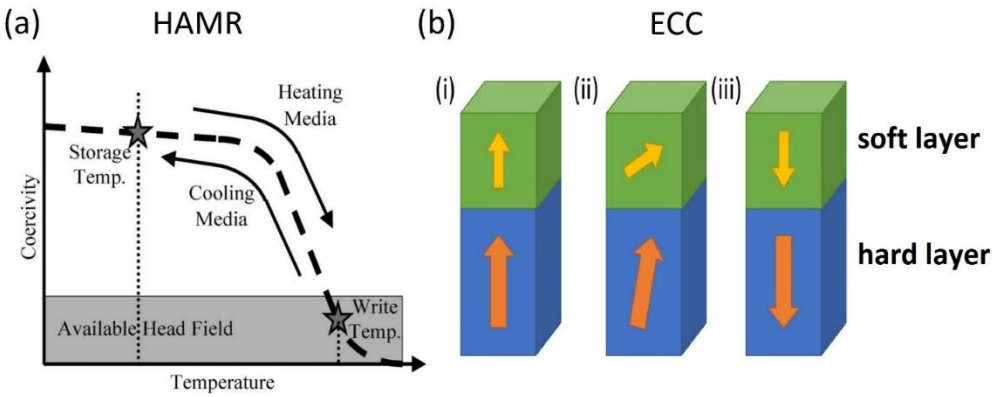

Fig 1.10 Schematic of both (a) (adopted from ref A58) HAMR and (b) ECC magnetic recording. For HAMR, a pulse laser is used to raise up the temperature of the local media, so that its coercivity would drop, lower than the available head field to ensure its writability. After that, the heat dissipates rapidly, and the high anisotropy at room temperature remains. For ECC, the recording media is composed of at least two layers (i). The external magnetic field will first reverse the soft layer with lower Hc (ii), which will exert a torque on the hard layer through exchanging coupling and assist its reversal (iii).

Among these approaches, BPM appears to be promising for ultrahigh-density towards 5 Tb/in^2. For traditional PMR, a "bit" of information is stored by a collection of grains, where the signal to noise ratio (SNR) is given by $SNR=10\times log(N)\ dB$, with N being the average number of grains per bit [A61]. For BPM, however, each bit is represented by only one predefined dot. Thus, the volume of each individual bit/dot determines the energy barrier against thermal fluctuation and enables a much higher storage density. The schematic of BPM recording is shown in fig 1.12.

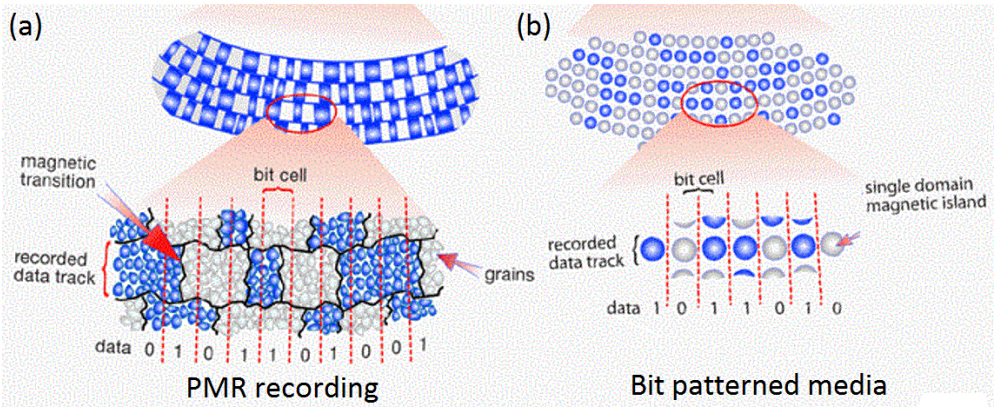

Fig 1.12 Schematic of the BPM recording (adopted from ref A62). (a) For traditional PMR recording, each bit of information is represented by a collection of grains, while (b) in BPM it is defined by a lithographically patterned dot.

From the media point of view, there are two critical issues facing BPM, both of which rely not only on the intrinsic properties of thin films [A63], but also on the processing. First, magnetic material with a high magnetocrystalline anisotropy is required. However, $L1_0$ FePt is normally deposited under elevated temperatures around 800°C [A64] in order to achieve good chemical ordering and high anisotropy. Such high growth temperature is unfavorable for mass production in practice. Further, it introduces large surface roughness during the grain growth [A64], which would in turn, generate unfavorable boundary and surface pinning sites. Thus, a process of low temperature FePt fabrication, ensuring both high anisotropy and low surface roughness, is desired.

Second, the top-down design and fabrication of BPM requires a high-quality and low-cost lithographical patterning method [A65] in order to achieve narrow dot size distribution, less shape variations, and high throughput in a wafer scale. However, with each bit represented by only one patterned dot, any fabrication defects would be more fatal compared to the traditional PMR recording, and will be reflected directly into a higher bit-error rate (BER) [A60]. As a result,

a high quality patterning technique is required. It has been reported that any dot *shape* fluctuation only contribute a second-order disturbance and can be neglected [A60]. However, the dot *size* fluctuation is predicted to be critical [A57] and narrow distribution (dot-size standard deviation, σ < 10%) is required for densities larger than 1 Tb/in^2 [A66].

One promising approach for the patterning is nanoimprint lithography (NIL) [A67], with advantages such as high resolution, low cost and high throughput in wafer scale [A68]. However, few studies [A64][A69-A71] have been reported on high quality, NIL fabricated, epitaxial $L1_0$ FePt dots array with good control over dot-size distribution. More details about the NIL technique will be discussed in chapter 2.

Given that, it is important to study the PMA system within the *single domain limit* using NIL patterning, not only to achieve lower growth temperature of $L1_0$ FePt with high chemical ordering, but also to enable high quality nano-patterning in a cost efficient way. In this thesis, we demonstrate the fabrication of $L1_0$ FePt thin films at a lower growth temperature (450 °C), with high crystalline quality and perpendicular magnetic anisotropy using high vacuum ion beam sputtering with low sputtering rate and post annealing process. Further, large-area (0.75 cm×0.75 cm) dots array of $L1_0$ FePt demonstrates high coercivity and presents a good candidate for bit patterned-media (BPM) recording.

1.7 Brief outline of the thesis

In this thesis, we study the magnetism and interactions within the *single domain limit*. Two of the most fundamental magnetic interactions, dipole interaction and exchange interaction, are discussed in depth, motivated by both scientific understanding and industrial application.

In chapter 1, we reviewed different characteristic lengths within a magnetic system through the competition between dipole and exchange interactions. Phenomena within the *single domain limit* are discussed. Based on the underlying physics, we further introduced two applications: *magnetic quantum-dot cellular automata* (MQCA) logic, and *perpendicular magnetic recording* (PMR), both of which are further discussed in following chapters.

In chapter 2, we discussed the principle experimental and simulation methods employed within this project: (i) thin film deposition, (ii) patterning method aimed at *single domain limit*, (iii) different material characterization techniques, and (iv) micromagnetic simulation.

Then in chapter 3, dipole interaction within the *single domain limit* is discussed. The behavior of *nanomagnet dots array* opens the door for non-volatile logic device— MQCA logic. We propose and demonstrate a 45° clocking mechanism which would help intrinsically eliminate errors due to clocking misalignment. Both basic logic units (such as *nanomagnet arrays* and *majority gates*) and complicated design (such as *full adders*) are demonstrated. This novel clocking mechanism facilitates stable operation of MQCA logic and paves way for its potential application.

In chapter 4, exchange interaction within the *single domain limit* is studied within a perpendicular anisotropy system, aimed at the application for high areal density magnetic recording. Epitaxial $L1_0$ FePdPt and FePt thin films demonstrate high chemical ordering and perpendicular anisotropy. A multi domain to single domain transition for $L1_0$ FePt is observed at ~250 nm which corresponds to its *single domain limit*. High quality $L1_0$ FePt thin films are then patterned to sub-100 nm dots array with robust performance. Further, exchange-coupled FePt/Co bilayer heterostructure shows a uniform switching process in dots array, and potentially paves the way for exchange coupled composite-BPM (ECC-BPM) recording.

Finally in chapter 5, future possibilities are explored: (a) integration of MQCA logic into the electrical circuit in order to serve for more complicated systematic architecture, and (b) spin-stand test for the sub-100 nm $L1_0$ FePt dots array, aiming at BPM recording density over 5 Tb/in^2.

Chapter 2

METHODS

In this chapter, we discuss: (i) thin film deposition methods with ion beam sputtering system, (ii) nanofabrication by electron-beam lithography, nanoimprint lithography and focused ion beam milling, (iii) characterization for crystalline structure, micro/nano-structure, composition, magnetic state and reversal, and (iv) numerical modeling using micromagnetic simulation.

2.1 Thin film deposition

2.1.1 Physical deposition

The act of transporting a thin film material to a substrate surface is called thin film deposition, which has a long history that can be traced back to the ancient time when the craft of gold beating has been practiced for the purpose of protection and ornamentation [B1]. In modern time, thin film technology has been widely applied in the Si CMOS technology, medical surface coating, etc. Typically, thin film deposition can be classified as chemical deposition and physical

deposition, depending on whether or not the deposition process involves a chemical reaction [B2]. In the former case of chemical deposition, there are chemical reaction of different precursors at the thin film surface. Chemical deposition includes atomic layer deposition and chemical vapor deposition [B3]. For physical deposition, on the other hand, no chemical reaction is performed. Different types of process, such as mechanical, electromagnetic and thermodynamic means, are employed during thin film deposition [B4]. In this thesis, we mainly focus on the physical deposition methods.

During the physical deposition process, a vacuum environment is critical to ensure a high quality thin film, for two reasons. First, the atomic particles for the thin film material have to avoid collision with residual air molecules when moving from source to substrate. The average traveling path before impacts (collisions) [B5] for atoms is highly related to the vacuum level in the chamber, and better vacuum leads to less chance of collision with residual air molecules. Second, impurities, such as oxygen and moisture particles from the residual air, may attach onto the sample surface before and during the thin film deposition and hence change the chemical phase or purity of the desired thin film. It can be calculated that even within a vacuum in the range of 10^{-5} torr, the air molecules could accumulate at the rate of ~2.4 monolayers per second [B4]. Given that, we used ultra-high vacuum (UHV) system for all the sample fabrication in this thesis, with base pressure better than 8×10^{-8} torr.

There are many different types of physical depositions, such as thermal evaporation, electro-hydrodynamic deposition and pulsed laser deposition. Among all these is sputtering, where atoms from the solid source are extracted by collision of highly energized particles. During sputtering, the target material is physically removed through bombardment with gaseous ions, such as Ar^+, which is accelerated by strong electric field within an ion gun (for example,

Kaufman ion gun in our ion beam sputtering system). After that, the target material is deposited onto the sample surface, forming a thin film.

2.1.2 Ion beam sputtering system

In this thesis, an ion beam sputtering (IBS) system was used for thin film deposition. The IBS system uses accelerated Ar^+ ions to knock off the desired material from the target. First, argon ions, Ar^+, are generated in the source by collisions of neutral Ar atoms with electrons from a hot filament, following acceleration by the electric field emanating from a grid toward a target. Then, the accelerated Ar^+ ions are neutralized by electrons emitted from a second filament. With a high dynamic energy, the Ar atoms bombards the target surface and knocks off the desired material, which is then deposited onto the substrate surface [B6].

The IBS system we use is a home-built ultra-high vacuum IBS (UHV-IBS) system [B7][B8] with a base pressure better than $5x10^{-8}$ torr. It can reach a temperature range from ambient temperature to 480°C and is capable of *in situ* annealing. Figure 2.1 shows the schematic of our IBS system. A modified electron gun is employed to generate the Ar^+ ions [B9] where the target is separate from the ion source. Our IBS system has several advantages over other sputtering system. (i) The energy and flux of ions can be controlled independently. (ii) Either insulating or conducting targets can be sputtered since the flux that strikes the target is composed of neutral Ar atoms. A deposition rate, as low as 0.5 Å/sec, can be achieved by tuning the source beam voltage. This low deposition rate would help ensure high epitaxial quality with desired chemical ordering.

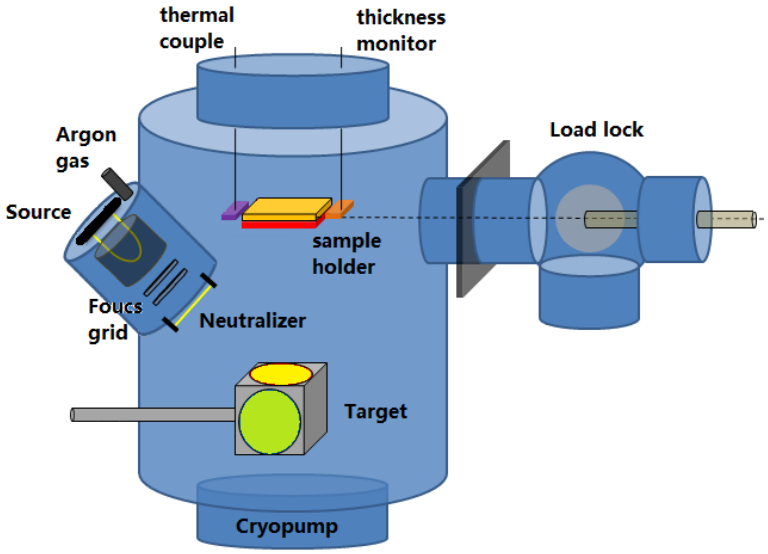

Fig 2.1 Schematic of the home-built UHV IBS system. The Argon atoms are ionized, accelerated, neutralized, before bombardment onto the target. Desired material is knocked off and deposits on the surface of the substrate attached to the sample holder that can be heated up to 450 °C.

2.2 Nanofabrication

Here, we discuss different nanofabrication techniques we employed in the thesis. From a scientific point of view, in order to study the magnetic behavior within the *single domain limit*, nanofabrication techniques is needed to pattern continuous thin film down to nanostructures within different length scale. From an industrial point of view, the application of both MQCA logic and PMR recording requires robust patterning techniques, including different types of lithography and etching methods.

Depending on the lateral size of the nano-features, different types of patterning techniques have been employed in this thesis, including electron-beam lithography, nanoimprint lithography and focused ion beam milling.

2.2.1 Electron-beam lithography

Electron-beam lithography (EBL) is a patterning technique using a focused electron beam to draw custom-designed nanostructure on substrate covered by a polymer resist [B10]. The exposure of resist under electron beam changes its solubility in the developer solution, enabling selective removal by the subsequent developing process.

In this thesis, poly (methyl methacrylate) (PMMA), a polymer material which is sensitive to high-energy electrons is employed. PMMA normally comes into two molecular weights, 495K and 950K. For our samples, the 950K resist diluted in 3 % anisole (950-A3) [B11] was used. Following spin coating the PMMA resist onto the substrate surface, a highly customized writing process under the control of the Nanometer Pattern Generation System (NPGS) software and the electron-beam writer was carried out, with a typical exposure dosage between 50 ~ 500 $\mu C/cm^2$. Next, the substrate was immersed into the developer (1:3 MIBK to IPA) for 70 sec to remove the exposed portion of polymer for developing. After that, desired thin film materials were deposited before the sample was immerged in Remover-PG [B12] for lift-off.

The primary advantage of EBL is its high resolution (<20 nm). One can achieve features in nanoscale with the help of EBL, because of the intrinsic advantages of electrons over traditional photolithography, such as high energy and low wavelength. However, the tradeoff of low throughput limits its usage to small scale patterning compared to other lithography techniques, such as photolithography and nanoimprint lithography. Hence, EBL was used as the patterned method for the MQCA logic demonstration in this thesis where the feature size is about 100 nm.

Fig 2.2 FEI XL-30 SEM for the EBL process in this thesis.

Our EBL experiments were carried out at the NanoTech User Facility (NTUF), at the University of Washington, using the FEI XL-30 scanning electron microscope (SEM), as shown in fig 2.2. We developed a recipe for Polymethyl-methacrylate (PMMA)/ LOR 1A (MicroChem Corp., Newton, MA) bilayer resist to achieve an undercut profile. This bilayer structure would prevent sidewall deposition during sputtering and facilitate the lift-off process (fig 2.3). A detailed standard operation procedure (SOP) for this process can be found in Appendix-2 of this thesis.

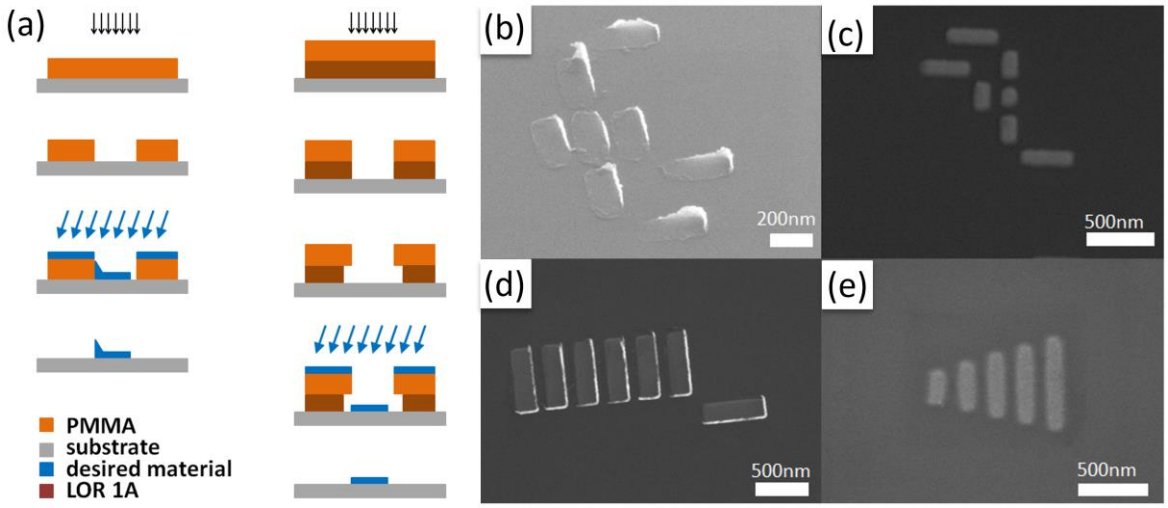

Fig 2.3 (a) Comparison between the monolayer resist and the bilayer resist through the lithography process. The bilayer resist prevents side-wall deposition by introducing an undercut profile. SEM images after lift-off (b)&(d) using monolayer resist and (c)&(e) with PMMA/ LOR 1A bilayer resist. The undercut structure leads to a clear and sharp edge.

2.2.2 Nanoimprint lithography

Nanoimprint lithography (NIL) uses stamps [B13] to mechanically deform the imprint resist on the substrate surface. The imprint resist was uniformly spin coated onto the substrate surface and followed by the physical imprinting. The imprinting process is usually combined with curing by either heat (thermal imprint), or UV light (UV imprint), or both of them. Conventionally, surface treatments, such as hydrophobic layer coating, are carried out beforehand to ensure proper release of the stamp. After the release, different etching and liftoff techniques are employed before thin film deposition in order to achieve the correct nanostructure.

A mask transfer technique is employed in our NIL patterning process to both prevent damage of the mother mold, which is relatively expensive, and realize mass production of

patterned samples. The hard mother stamp (Silicon or Quartz) is first used to generate multiple negative daughter stamps. For feature size larger than 100 nm, ethylene tetrafluoroethylene (ETFE) is used as a soft stamp to minimize the influence of defects, enabling both high imprint-yield and low cost. For sub-100 nm features, ormostamp (Microresist, Berlin, Germany) is used because it can achieve higher resolution (< 10 nm) and thus smaller feature size.

The NIL nanofabrication has several advantages, such as high throughput, high resolution, and low cost. On the one hand, similar to EBL, it eliminates the wavelength's limitation on feature size due to its mechanical imprinting nature. On the other hand, its simplicity enables low cost fabrication while the majority cost is associated with stamp fabrication, which can spread out over the stamp replication process, as mentioned above. All these advantages make NIL technique promising for the industrial applications where both high yield and low cost are desired, such as bit patterned media (BPM) recording, which is a promising candidate for next generation of high density magnetic recording [B14].

The conventional NIL process includes (i) imprinting; (ii) dry-etching; (iii) developing, (iv) deposition, and (v) lift-off, as shown in fig 2.4(a). Other than that, our group developed different variations of NIL for different purpose [B15-B17]. First, a recipe using a bilayer resist of NXR-1025 (Nanonex, Monmouth Junction, NJ)/ LOR 1A is employed to achieve the undercut profile, similar to the EBL process discussed in section 2.2.1 [fig 2.4(b)]. Second, for epitaxial deposition, elevated temperatures are required, where polymer resists are unstable. To solve this problem, a mask transfer from polymer to metal mask is required. We first employ Molybdenum deposition and polymer lift-off. It is then followed by another round of deposition of desired material and Mo lift-off by H_2O_2. Next, post-patterning using ion-milling is carried out for fabrication of sub-100nm dots of epitaxial material. The schematic of Mo mask-transfer and

post-patterning techniques using ion-milling are shown in fig 2.4(c)&(d). Further to fabricate the sub-100 nm dots array, we developed the combination of Mo mask-transfer and ion milling [fig 2.4(e)], as will be discussed in *chapter 4*. Our NIL experiments were carried out using the Nanonex NX-B100 nanoimprinter (fig 2.5) at the University of Washington – Washington Nanofabrication Facility (UW WNF).

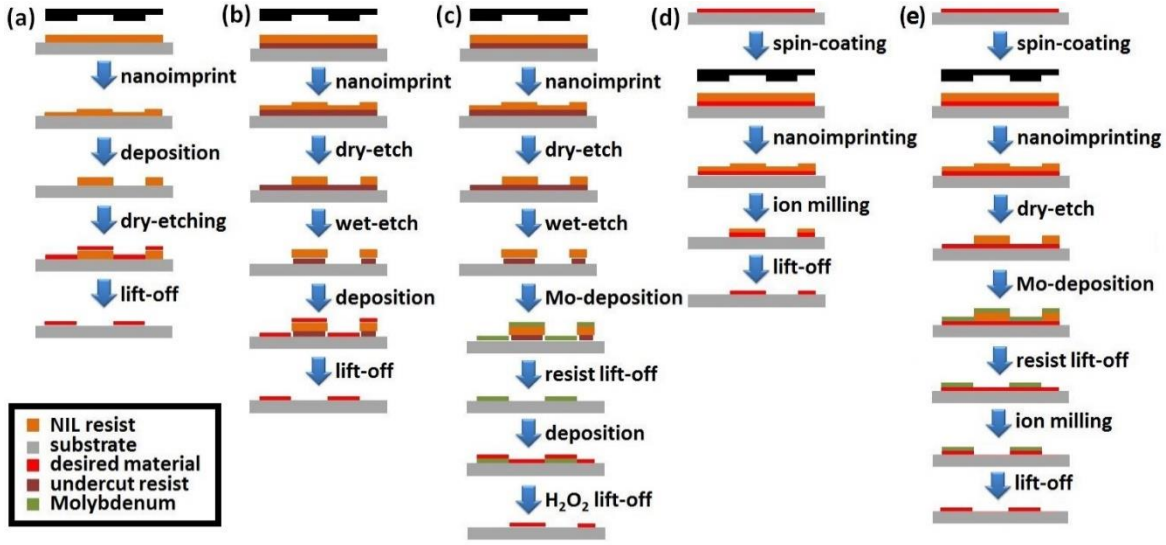

Fig 2.4 Schematic of NIL processes: (a) Conventional NIL process, (b) bilayer resist NIL to achieve undercut profile, (c) Mo mask-transfer, (d) post-patterning using ion milling, and (e) combination of Mo mask-transfer and ion milling for sub-100 nm dots array fabrication. Process (c), (d) and (e) are developed in this thesis.

Fig 2.5 Nanonex NX-B100 nanoimprinter at the UW WNF cleanroom.

2.2.3 Focused ion beam milling

Focused ion beam (FIB) resembles a scanning electron microscope (SEM), except that it uses beam of Ar^+ ions instead of electrons. It also includes an electron beam facilitating investigation using either/ both of the beams [B18]. Gallium liquid-metal ion sources (LMIS) are used, where Ga metal in contact with a tungsten needle melts after heating and flows to the tip of the needle forming a cusp shaped tip called a Taylor cone, following ionization and field emission of the gallium atoms. Source ions are then accelerated and focused onto the sample surface. One drawback of FIB is that it causes specimen destruction by surface bombardment and Ga implantation, which can be prevented by introducing a thicker protection layer on top of the wanted material of the thin film samples.

Our FIB experiments were carried out at the NanoTech User Facility (NTUF), at the University of Washington, with the FEI XL830 dual beam workstation. The XL830 workstation is a single platform for both high-resolution electron/ ion imaging and site specific milling. The ion milling was performed using a current of 150 pA, magnification of 20,000X, dwell time of 2 μs, resolution of 350 pixel ×350 pixel. We set the milling time as 30 sec for 10 nm thick FePt epitaxial samples capped with 3 nm-thick gold.

2.3 Characterization

2.3.1 Crystalline structure: x-ray diffraction

The chemical ordering and epitaxy quality of materials in this thesis were examined using X-ray diffraction (XRD). X-ray is a type of electromagnetic radiations generated by bombardment of electrons onto a target material [B19-B21]. Taking the Rigaku XRD in our lab as

an example, an electron beam, accelerated by a high field, bombards on a rotating Cu target. The high energetic electron beam hits on copper atoms and kicks out electrons in their inner shell (K shell) and correspondingly introduce vacancies in the inner shells. After that, these vacancies in the inner shells are filled by electrons from an outer shell (L shell). To compensate the energy difference between L and K shells, a characteristic X-ray is released. For the Cu target, this X-ray has a wavelength of 1.54 Å. Since this wavelength is comparable to the atomic periodicity in most crystals, X-ray can be used for probing the atomic structure of most materials.

When exposed to the X-ray, the sample material would scatter the incident beam, as the parallel atomic planes generates an interference pattern in the diffracted beam. This pattern is associated with the angular variation of the diffracted radiation with respect to the incident beam. Thus, its angular position and intensity could be used as a fingerprint to identify the atomic structure of the sample material. As Bragg's law describes, a diffraction peak would occur when certain conditions are met. For a given set of lattice planes with an inter-plane distance of d, it is written as:

$$n\,\lambda = 2\,d\,sin\theta \ldots\ldots \quad (2.1)$$

where n is a integer number, λ is the wavelength of X-ray beam (1.54 Å for Cu), d is the inter-plane spacing of the atomic lattice, and θ is the angle between incident beam and the normal direction. This θ-2θ scan configuration of XRD is shown in fig 2.6.

In this thesis, the crystalline structure of the material was investigated by θ-2θ scans. In a θ-2θ scan, scattered waves from different atomic layers interfere with each other, resulting in an intensity distribution. The sharp interference peaks could be used to identify the atomic structure and phase of the material following Bragg's law.

Next, the texture of thin films is determined by the full width at half maximum (FWHM) of the rocking curves, or the so-called ω-scan. In a rocking curve measurement, the θ is fixed for a certain *d* spacing, while the sample is tilted along the ω direction, as marked in fig 2.6. Typically, a sharp single peak along $\omega = 0$ would be observed, indicating that most grains are grown along the normal direction of the thin film surface. However, for some grains the diffraction relationship could only be satisfied when the sample plane tilts, so that their normal axis could be aligned to the ideal thin film normal axis. Such a tilting will contribute to a distribution of the normal direction for grains; a sharper peak with lower FWHM suggests better epitaxial quality.

Third, the in-plane Φ-scan, or so-called pole figure, was employed to confirm the epitaxial relationship between the single crystal MgO (001) substrate and our epitaxial thin film. In the in-plane Φ-scan mode, the θ is preset to a specific angle to capture the desired crystallographic orientation. Then, the diffraction is measured when the sample rotates along its normal or, Φ direction. Only limited number of intensity peaks can be detected for an epitaxial film, depending on the structural symmetry of the given material. Further, it could help find the distribution in crystalline orientations of grains in a textured sample.

In addition, X-ray reflectivity (XRR) technique was used to extract information on layer thickness and interface roughness. In the XRR geometry, X-ray strikes the thin film surface at only a small angle, typically less than 5°. While XRD depends on the interference of the diffracted X-rays from periodic lattice planes, XRR only relies on the interference of X-rays at interfaces owing to difference in electron density between different layers.

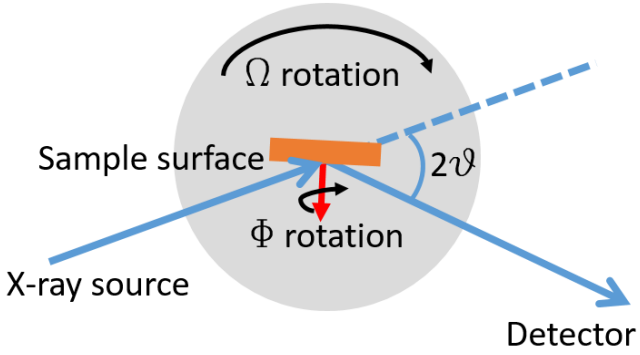

Fig 2.6 XRD configuration and different types of scans to characterize the crystalline structure of samples: (a) by θ-2θ scans, (b) rocking curves, (c) in-plane Φ-scan, and (d) X-ray reflectivity

In this thesis, the X-ray diffraction studies were carried out in both our research lab and at Environmental Molecular Science Laboratory (EMSL) at Pacific Northwest National Laboratory (PNNL). We used all these types of scans to analyze the crystalline structure of the samples with the help of Cu K_α radiation.

2.3.2 Magnetic reversal: vibrating sample magnetometer

Vibrating sample magnetometer (VSM) is one of the most common methods to measure the hysteresis loop of a magnetic element. As Faraday's law states, a changing magnetic flux will generate an electric voltage across a close loop. This voltage could be measured and linked to the magnetic moment within the sample. During VSM measurements, the sample, driven by a motor, is vibrated in sinusoidal motion. The induced electrical signal is recorded by a pickup coil. By correlating the pickup coil and the external magnetic field measured by a gauss meter, we could generate the magnetic hysteresis loop.

In this thesis, the magnetization state and reversal process of the sample were studied by VSM installed in a Physical Property Measurement System (Quantum Design Inc). For our PPMS system, a typical thin-film sample has a dimension of 5 mm × 5 mm. The PPMS working station is shown in fig 2.7. The data was further analyzed using C language and Origin software.

In addition to the major hysteresis loop, we carried out several different measurements to further extract information about the magnetic switching, including the first order reversal curve (FORC) [B22][B23] and d.c. demag curves, which are further discussed in Appendix-1.

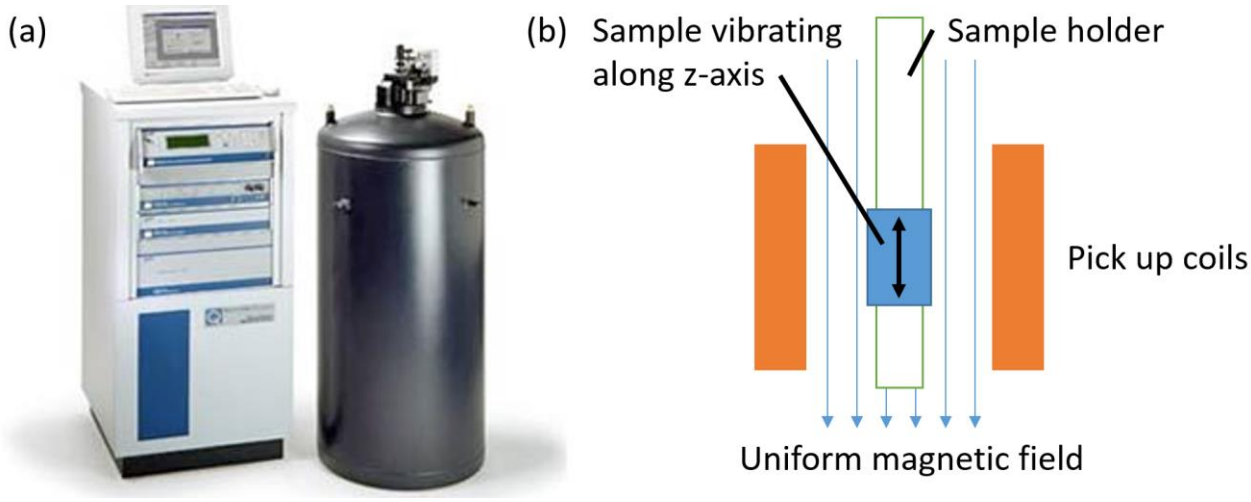

Fig 2.7 (a) PPMS station in our lab. (b) Schematic of the measurement setup.

2.3.3 Magnetic configuration: magnetic force microscopy

Scanning probe microscopy (SPM) is a class of microscopy, which through physically scanning a fine tip over the surface of a sample, investigates properties, such as topology and magnetic domain configuration. In an SPM station, a cantilever with a tip in width of ~10 nm, corresponding to its lateral resolution, is employed. On the other hand, the depth resolution is determined by the height control; the cantilever is connected to a piezoelectric transducer (PZT),

which controls its height, suggesting a height resolution of ~100 pm after fine PZT calibration. The PZT also ensures that the tip is well-engaged with the sample surface— that the tip is close enough to the sample in order to collect the surface signal, but not too close to physically scratch it. Besides the cantilever and the PZT, a super-luminescent diode generates a focused light beam, which is casted on the upper side of the cantilever. The reflection of the beam is collected by a photo-detector. As a result, a deviation of the reflection from the central point of the photo-detector suggests a height change of the tip, which is then transmitted to the PZT through a feedback circuit for height control, as shown in fig 2.8(a).

In this thesis, we use two modes: (a) atomic force microscopy (AFM) mode and (b) magnetic force microscopy (MFM) mode. For AFM, we use the non-contact mode to measure the topology of the sample; the tip oscillates so that the change in amplitude of the oscillation could be measured when the tip is approaching the sample surface. As the tip approaches the sample surface, the cantilever bends and suggests a deviation of the reflected light, according to which the PZT would change its height to ensure a constant and continuous engagement between the tip and the sample surface. On the other hand, in the MFM mode, the tip is coated with a thin magnetic layer. The cantilever scans over the sample surface for a second time with a fixed distance, delta height, to capture the phase signal introduced by the dipole interaction between the sample surface and the magnetic tip. This phase signal is then translated into the magnetic configuration [fig 2.8(b)].

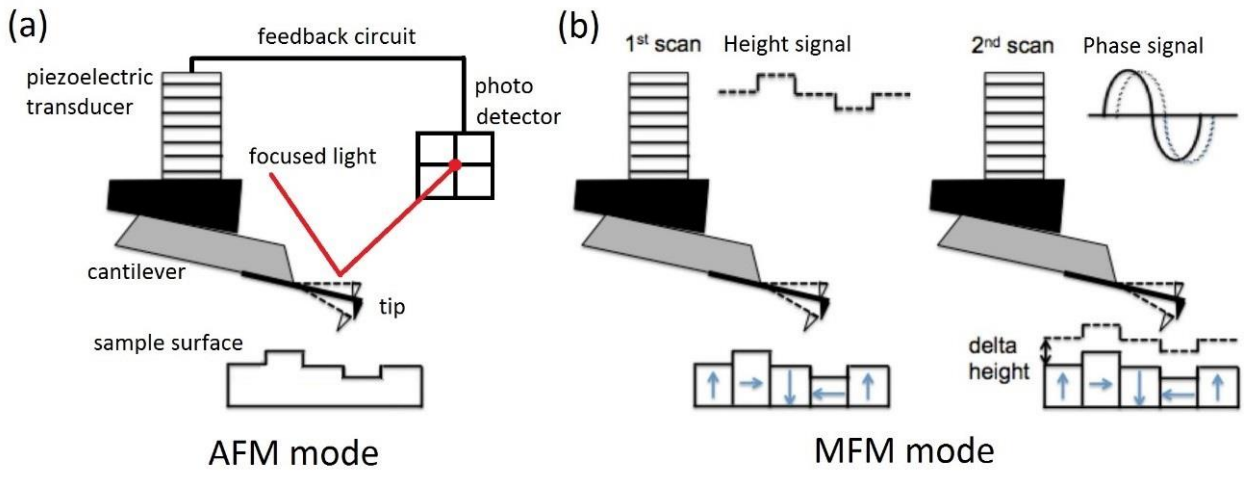

Fig 2.8 Illustration of two modes: (a) the atomic force microscopy mode (AFM), and (b) the magnetic force microscopy mode (MFM).

Here, the surface topology and magnetic configuration of our samples were investigated by both AFM and MFM, by a 15 nm CoCr coated low- moment probes with a lift height of 50 nm [B24]. The low- moment probes are employed because they not only have a high sensitivity in measuring the local magnetic patterns but also ensure that the magnetic field from the tip does not interfere much with the sample surface. Figure 2.9 shows the SPM station in our research lab.

Fig 2.9 Scanning probe microscopy (SPM) station with both AFM and MFM modes.

2.3.4 Chemical composition: Rutherford backscattering spectroscopy

In this thesis, Rutherford backscattering spectroscopy (RBS) analysis was performed to determine the depth profile and the chemical composition of each layer in the thin film samples. RBS is an ion scattering technique used mainly for surface compositional analysis of thin film samples. It is based on elastic collisions between two atomic nuclei, one a high kinetic energy particle from the incident beam (He^{++}, for example) and the other a stationary particle located in the target sample. Both the number and energy of ions of the backscattered beam after the collision are measured at given angles. Since the backscattering pattern for each element is well known, depending on its atomic number, beam angle etc., we can obtain a quantitative compositional depth profile of the thin film samples from the RBS spectrum. The schematic of RBS is shown in fig 2.10.

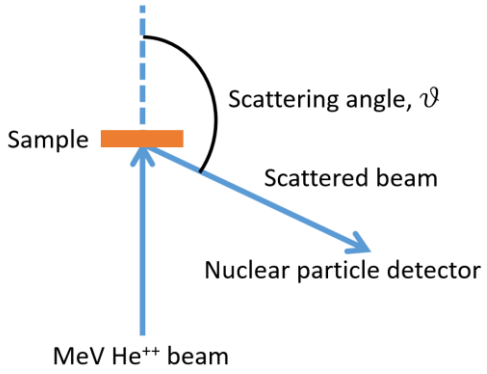

Fig 2.10 Schematic of the Rutherford backscattering spectroscopy. The backscattered He^{++} ions after collision with sample materials is collected and analyzed by a nuclear particle detector.

Here, the experiments were carried out at the Environmental Molecular Sciences Laboratory (EMSL) in Pacific Northwest National Laboratory (PNNL). The high-resolution RBS was performed using National Electrostatic Corporation (NEC) 3MV Electrostatic Tandem Ion Accelerator using 2MeV He^{++} ions at 7° angle of incidence from the sample normal. The

backscattering spectra were collected using a silicon surface barrier detector at a scattering angle of 150°. Data analysis was carried out using the SIMNRA simulation code [B25]. Details of SIMNRA simulation to obtain atomic concentration and stoichiometry in each layer have been outlined in peer reviewed research papers [B26]. Fig 2.11 shows the RBS system used for experiments within this thesis.

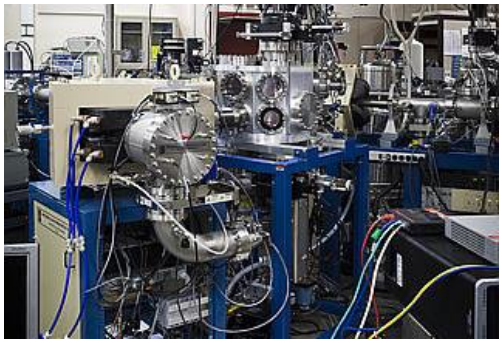

Fig 2.11 The RBS system in Pacific Northwest National Laboratory (PNNL) that is used to determine the depth profile of chemical composition for thin film samples.

2.3.5 Compositional depth profile: X-ray photoelectron spectroscopy

X-ray photoelectron spectroscopy (XPS) observes the chemical composition of a surface using the photoelectric effect. A photon source, such as an X-ray, is directed to the sample, whereas the photons interact with the electrons within the sample material, usually on the surface top layers [fig 2.12(a)]. The photon, which has sufficient energy, causes an electron to be emitted from the sample material, which can be theoretically described as

$$E_{kinetic} = h\upsilon - E_{binding} \ldots\ldots \quad (2.2)$$

where $E_{kinetic}$ represents the kinetic energy of the emitted photoelectron, $h\upsilon$ is the energy of the source photon, and $E_{binding}$ stands for the binding energy for the emitting electron. Since $E_{kinetic}$ could be measured, and $h\upsilon$ is known for the X-rays, $E_{binding}$ could be calculated in

order to probe with what energy the electron was held in its atomic environment, and thus the material composition could be detected.

Here, the XPS experiments were carried out using a Surface Sciences Instruments (SSI) S-Probe at the *Molecular Analysis Facility* [fig 2.12(b)]. The instrument has a monochromatized Al K_α X-ray source and a low energy electron flood gun for charge neutralization. Analysis area for these acquisitions was on the order of 800 µm across, with a pressure in the analytical chamber better than 5 x 10^{-9} torr. Pass energy for survey spectra was 150 eV. The *Service Physics Hawk v7* software program was used for all high resolution peak fitting, in order to determine peak areas and to calculate the elemental compositions from peak areas.

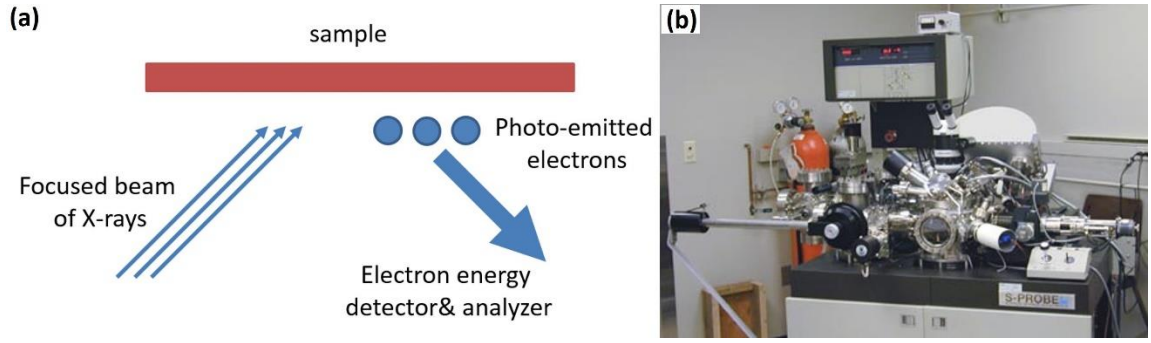

Fig 2.12 (a) Schematic of the XPS using X-rays as the photon source. The photons interact with the electrons within the sample material, and cause electrons to be emitted from the sample material. (b) XPS system at *Molecular Analysis Facility* that is used to determine the depth profile of Ag composition for samples.

2.4 Micromagnetic simulation

Micromagnetic simulation is a powerful modelling tool to study the magnetic domain configurations and the magnetic switching process for elements within micro- and nano-meter scale. Through the process of finding the energy minimum state under given initial state and boundary conditions, micromagnetic simulation solves for the magnetization, $\vec{M}$, as a function of

space and time. In this section, we briefly discuss the working principle of micromagnetic simulation.

2.4.1 Continuum hypothesis and total energy

To describe the magnetic configuration and behavior of a system, the classical *continuum hypothesis* is employed in micromagnetic simulation, which assumes that the magnetization within a system could be represented by a continuous vector field, $\vec{M}(\vec{r})$, where $\vec{r}$ is the position vector [B27,B28]. Thus, we could write:

$$\vec{M}(\vec{r}) = M_S \cdot \vec{m}(\vec{r}) \ldots\ldots \quad (2.3)$$

$$\vec{m} \cdot \vec{m} = 1 \ldots\ldots \quad (2.4)$$

where M_s is the saturation magnetization, and $\vec{m}$ is a unit vector representing the direction of $\vec{M}(\vec{r})$. Based on this description, different energy terms, as discussed in *chapter 1*, could be formulated by the magnetization vector field, $\vec{M}(\vec{r})$, and subsequently minimized in order to simulate the magnetic configuration.

First, the exchange energy, E_{ex}, is formulated by the interaction between two nearest-neighbor spins in a microscopic model, as

$$W_{ij} = -2J\,\vec{S_i} \cdot \vec{S_j} \ldots\ldots \quad (2.5)$$

where J is the exchange integral, and $\vec{S_i}$ is the spin angular momentum of spin *i*. If we assume the spacial angle variation between adjacent spins θ_{ij} to be very small, then we have

$$\vec{S_i} \cdot \vec{S_j} = S^2 cos\theta_{ij} = S^2\left(1 - \frac{1}{2}{\theta_{ij}}^2\right) = S^2\left(1 - \frac{1}{2}\left|\vec{m_i} - \vec{m_j}\right|^2\right) \ldots\ldots \quad (2.6)$$

Given that, the exchange energy per unit volume, w_e, is written as

$$w_e = \frac{1}{2} nJS^2 \sum_j \left[(\overrightarrow{s_j} \cdot \nabla) \overrightarrow{m_i} \right]^2 \ldots\ldots (2.7)$$

where n represents the number of spins per unit volume. For a magnetic system, the total exchange energy, E_{ex}, is defined as

$$E_{ex} = \iiint w_e dv \ \ldots\ldots (2.8)$$

Next, the magnetostatic energy, E_{ms}, caused by the dipole interaction, could be best described by the demagnetization field, $\overrightarrow{H_d}$, that describes the influence of all magnetic moments and its spacial distribution. We have

$$\begin{cases} \nabla \times \overrightarrow{H_d} = 0 \ldots\ldots (2.9) \\ \nabla \cdot \vec{B} = \nabla \cdot \left(\overrightarrow{H_d} + \vec{M} \right) = 0 \ldots\ldots (2.10) \end{cases}$$

If we define ϕ as a scalar potential, where

$$\overrightarrow{H_d} = -\nabla \phi \ldots\ldots (2.11)$$

We can derive that

$$\nabla^2 \phi = \begin{cases} \nabla \cdot \vec{M}, & within\ a\ magnetic\ element \\ 0, & outside\ the\ magnetic\ element \end{cases} \ldots\ldots (2.12)$$

Thus, the surface of a magnetic element determines the equilibrium dipole field, where the normal component of $\vec{B}$ and the tangential component of $\vec{M}$ must be continuous at the boundary. Mathematically, the scalar potential and the demagnetization field can be expressed as

$$\begin{cases} \phi(r) = \frac{1}{4\pi} \left[- \iiint \frac{\nabla \cdot M(r')}{|r - r'|} dV' + \iint \frac{\hat{\mathrm{n}} \cdot M(r')}{|r - r'|} dS' \right] \ldots\ldots (2.13) \\ H_d(r) = \frac{1}{4\pi} \left[- \iiint \frac{(\mathrm{r} - \mathrm{r}') \nabla \cdot M(r')}{|r - r'|^3} dV' + \iint \frac{(r - r') \hat{\mathrm{n}} \cdot M(r')}{|r - r'|^3} dS' \right] \ldots\ldots (2.14) \end{cases}$$

where n̂ is the surface outward normal vector. According to the equation (2.14), the demagnetization interaction is non-local and is attributed to the whole magnetization vector field. For a magnetic system, the total magnetostatic energy, E_{ms}, is formulated as

$$E_{ms} = -\frac{\mu_0}{2}\iiint \vec{M} \cdot \overrightarrow{H_d} dV \ldots\ldots (2.15)$$

Besides exchange energy, E_{ex}, and magnetostatic energy, E_{ms}, is Zeeman energy, E_{zeeman}, which represents the potential energy of the magnetic element subject to an external field, $\overrightarrow{H_a}$, as

$$E_{zeeman} = -\mu_0 \iiint \vec{M} \cdot \overrightarrow{H_a} dV \ldots\ldots (2.16)$$

Additionally, crystalline structure of the magnetic element would introduce the magnetocrystalline energy, E_{mc}, and it describes the extent to which $\vec{M}$ is aligned with respect to the specific principle axes. If we define w_a as the magnetocrystalline energy per unit volume, we can get

$$E_{mc} = \iiint w_a dV \ldots\ldots (2.17)$$

Thus, the total energy of a magnetic element is expressed as the summation of all different terms, which is

$$E_{total} = \iiint \left[w_e - \frac{\mu_0}{2}\vec{M} \cdot \overrightarrow{H_d} - \overrightarrow{\mu_0 M} \cdot \overrightarrow{H_a} + w_a \right] dV \ldots\ldots (2.18)$$

2.4.2 Micromagnetic equilibrium and LLG equation

For a constant external field and boundary condition, the equilibrium states, either the ground state or metastable states, are given by the minima of the total energy of a magnetic

element, E_{total}, provided that its first-order variation, δE_{total}, equates zero for any small variation of the vector field, $\delta\vec{m}$ [B29]. Solving for the differential equation, combined with initial state and boundary conditions, we can generate the equilibrium magnetization states of the magnetic elements. In practice, however, the analytical solution for a random system is difficult to find. Thus, the solution is usually carried out by numerical simulation with a given maximum number of iterations.

On the other hand, another approach [B30] is proposed based on the Landau-Liftshitz-Gilbert (LLG) equations [B31] in consideration of the intrinsic dynamic process and the quantum mechanics nature of the magnetic element. The principle of LLG equation is to introduce a viscous force $\frac{\alpha}{M_S}\boldsymbol{M}\times\frac{\partial \boldsymbol{M}}{\partial t}$, where α >0, M_S and $\boldsymbol{M}$ represent the damping constant, the saturation magnetization and its direction in a vector form, respectively. If we define H_{eff} as the combination of the external magnetic field, the demagnetizing field and the quantum mechanical effects and γ as the gyromagnetic ratio, we can get the LLG equation as:

$$\frac{\partial \boldsymbol{M}}{\partial t} = -\gamma \boldsymbol{M}\times \boldsymbol{H_{eff}} + \frac{\alpha}{M_S}\boldsymbol{M}\times\frac{\partial \boldsymbol{M}}{\partial t} \quad \ldots\ldots(2.19)$$

In order to put the first derivative to time on the left side, equation (2.19) is re-written as:

$$\frac{\partial \boldsymbol{M}}{\partial t} = -\frac{\gamma}{1+\alpha^2}\boldsymbol{M}\times\boldsymbol{H_{eff}} - \frac{\gamma\alpha}{(1+\alpha^2)M_S}\boldsymbol{M}\times(\boldsymbol{M}\times\boldsymbol{H_{eff}}) \quad \ldots\ldots(2.20)$$

2.4.3 LLG micromagnetic simulator

In this thesis, the micromagnetic simulation was performed to simulate the magnetization states and reversal of elements using a commercially available software, LLG micromagnetic simulator, which was invented by M. R. Scheinfein [B32]. The LLG micromagnetic simulator

solves the LLG equation by relaxation and/or integration, and is capable of characterizing both micromagnetic structure and dynamics in films [B33]. It is a full 3-dimensional simulation tool with integrated graphics that solves the LLG equation.

The simulation involves 5 steps. First, the geometry and material properties of the magnetic element are defined within the user interface. Next, different boundary conditions and initial state are loaded. Then right before calculation, the object is discretized into cells, which represent the minimum units during the whole calculation process. The magnetization $\vec{M}$ is assumed to be uniform within a cell; the cell size should be comparable to the exchange length [B34], so that the magnetization gradient can be safely neglected. Fourth, the calculation is performed to find the minima of the total energy. Last, the final result and relaxation process are viewed and analyzed within the LLG simulator.

Chapter 3[*]

MQCA LOGIC AND DIPOLE INTERACTION

3.1 Dipole interaction within the single domain limit

Dipole interactions within the single domain limit for shape-tuned nanomagnet array was studied in this chapter. We proposed a 45° clocking mechanism, combined with shape-tuned nanomagnet arrays that would intrinsically eliminate clocking misalignments. The clocking mechanism was demonstrated for both *signal propagation* and *logic operation*. Correct output was detected for both configurations. Further, we carried out two digital binary full adder, which provides high stability for MQCA logic and potentially paves way for its application.

As introduced in section 1.5, the concept of Magnetic Quantum-dot Cellular Automata (MQCA) [C1] aims to process information and perform Boolean logic operations via dipole

[*] Publications:

- Misalignment-free signal propagation in nanomagnet arrays and logic gates with 45°-clocking field, Zheng Li, BS Kwon, KM Krishnan, J. Appl. Phys. 115 17E502 (2014)
- Highly stable signal propagation in a consecutively tuned nanomagnet array, Zheng Li, KM Krishnan, J. Appl. Phys. 113 17B901 (2013)
- Misalignment-free logic operation in a 3-input MQCA full adder using 45°clocking mechanism, Zheng Li and KM Krishnan, under preparation

coupling between patterned elements within *the single domain limit*. For lithographically patterned rectangular nano-elements with aspect ratio η >2 in length scale of 100 nm, single domain state was observed for 30 nm-thick permealloy as shown in fig 3.1(a). The uniaxial shape anisotropy defines an easy axis and aligns the magnetization along this axis. Thus the reversal process would start with coherent rotation and can be described by the Stoner-Wohlfarth model [C2]. The corresponding Stoner-Wohlfarth astroid [fig 3.1(b)] [C3] is a curve that represents the angular dependence of the switching field, H_{sw}. Most notably, it predicts that for a uniaxial anisotropic magnetic element within the *single domain limit*, a reduced H_{sw} with minimum angular-sensitivity would be realized if the external field is applied 45° off the hard axis of the magnetic elements.

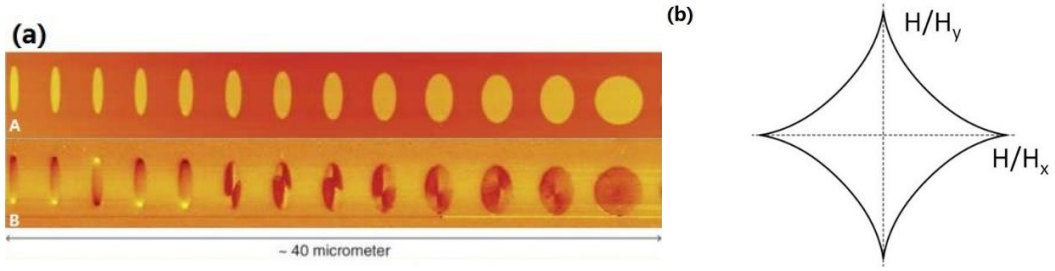

Fig 3.1 (a) (adopted from ref C1) AFM (upper) and corresponding MFM (lower) images for patterned nanoelements with varied aspect ratio. For the MFM image, the bright/dark contrast indicates different magnetic polarities, hence the domain structure. It is clearly demonstrated that the patterning induced shape anisotropy would introduce a uniaxial easy axis for the elements. (b) (adopted from ref C3) Schematic of the Stoner-Wohlfarth astroid, indicating the angular dependence of the switching field.

To test this idea, we carried out micromagnetic simulation for Fe elements [C4][C5] in scale of 100 nm with different aspect ratio η =2, 3, denoted as S_2 and S_3, as shown in fig 3.2(a). Magnetic modelling was carried out using LLG micromagnetic simulation [C6,C7]. To simulate the switching behavior of nano-patterned polycrystalline iron, which is deposited at room

temperature, the following parameters are used: saturation magnetization, M_s =1000 emu/cm^3, exchange constant, A = 2.1 μerg/cm. Magnetocrystalline anisotropy, K_{mc}, is set to be zero, because for the Fe polycrystalline element, the randomly directed grains would give an average of K_{mc} = 0. The 3-D model was meshed into discretized cells in size of 2.5×2.5×20 nm^3 to simulate the nanomagnets in thickness of 20 nm. The areal dimensional size equals the iron exchange coupling length of 2.5 nm [Tab 1.1]. Thus, the magnetization gradient is small enough so that the magnetization, M, can be considered as uniform within each individual cell. On the other hand, only 1 layer along z-axis was assumed as the thickness of each cell was set to be t = 20 nm, because magnetic phenomena, such as magnetic switching, took place mostly in the X-Y direction. This method has been proved practical by experiments.

First, we modeled each elements individually. The angular, θ, dependence of flipping field, H_{fl}, follows the Stoner-Wohlfarth model, i.e., H_{fl} decreases with increasing θ till the field is 45° off the hard axis of the element [fig 3.2(b)]. Next, to study the dipole interactions, we tested bimagnet system where S_2 and S_3 were placed adjacent to each other. Similarly, H_{fl} decreases with increasing θ. However, S_2 flips earlier owing to the dipole interaction where magnetic antiparallel state (AP-state) is energetically more favorable, as shown in fig 3.2(c). In short, an external field applied 45° off the hard axis triggers S_2 flipping with smaller H_{fl}, which is also less θ-sensitive, compared to that applied along the hard axis. Therefore, by applying and removing 45°-clocking field with amplitude between $H_{fl}^{(2)}$ and $H_{fl}^{(3)}$, we could realize AP-state with smaller field amplitude and higher θ tolerance. This AP-state corresponds to signal propagation in a nanomagnet array, while θ tolerance is related to misaligned clocking field.

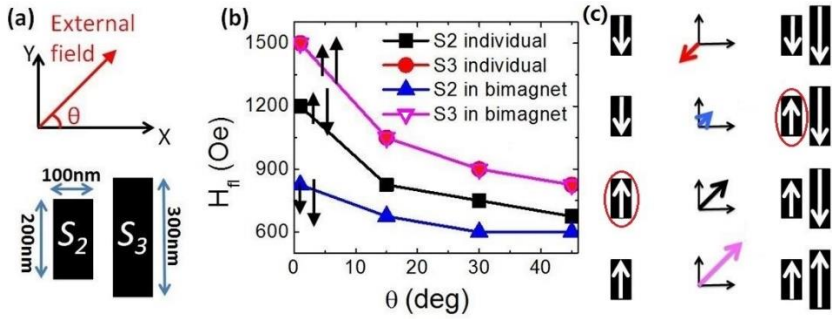

Fig 3.2 (a) Schematic of the nanomagnet structure and the angular-dependent magnetic field. (b) Simulated angular dependence of flipping field H_{fl} for elements S_2 and S_3, both individually and when put together. Curves for S_3 *individual* and S_3 *in bimagnet* overlap because the difference in H_{fl} is much smaller than for the other two curves. (c) Illustration of element flipping for S_2 both individually (left) and when putting together with S_3 (right). It is clear that S_2 would flip earlier in the bimagnet system than individually due to the dipole field, as highlighted by the red circle.

Next, we simulated a nanomagnet array where the shape anisotropy, K_S, was progressively tuned by shortening the long axis. A reversal field with 5°, 42° and 45° offset along the hard axis was applied, respectively. For a given field axis, element S_i would keep flipping and only reach its final state when the reversal field drops to some specific value. Element S_{i-1} with a lower K_S, is expected to flip first, such that it is antiparallel to S_i, and the resulting magnetostatic interaction will then hinder S_i from flipping. Considering only the dipole interaction from adjacent elements S_{i+1} and S_{i-1}, the flipping field of S_i is determined from $H_{fl}^{(i)}+H_{int}^{(i,\,i+1)}-H_{int}^{(i,\,i-1)}=H_{bar}^{(i)}$, where $H_{bar}^{(i)}$ represents the energy barrier for element i between two grounding states [state α in fig 3.3(a)]. After that, there are two possibilities: (a) further increasing negative field would cause S_{i+1} to flip down at $H_{fl}^{(i+1)}$, where $H_{fl}^{(i+1)}$ denotes the flipping field of element $i+1$ when considering the dipole interactions [state β]; or (b) when the clocking field is reversed the AP-state will remain until S_i flips up again at $H_{fl}^{(i^*)}$, as shown in fig 3.3-state γ. If we define $H_{int}^{(i,\,j)}$ as the dipole interaction field exerted on S_i by S_j, we get:

$$\begin{cases} H_{fl}^{(i*)} = H_{int}^{(i,i+1)} - H_{int}^{(i,i-1)} + H_{bar}^{(i)} = H_{fl}^{(i)} + 2\left(H_{int}^{(i,i+1)} - H_{int}^{(i,i-1)}\right) & \dots\dots(3.1) \\ H_{fl}^{(i+1)} = H_{bar}^{(i+1)} - \left(H_{int}^{(i+1,i+2)} - H_{int}^{(i+1,i)}\right) & \dots\dots(3.2) \end{cases}$$

Thus, a reversal clocking field in the range [$-H_{fl}^{(i+1)}$, $H_{fl}^{(i*)}$] will not affect the AP-state between S_i and S_{i+1}; neither of them will flip any more. Furthermore, we could define the stable field window (SFW) as the reversal field with amplitude lower than the minimum of $H_{fl}^{(i*)}$ and $H_{fl}^{(i+1)}$, i.e. a reversal field within SFW of S_i will not affect the AP-state between S_i and S_{i+1}. In general, if the amplitude of the reversal clocking field is reduced progressively passing through the SFW of different elements sequentially, the AP-state will be achieved from high anisotropic elements down to the lower ones. The higher the K_S of an element, the earlier it will become magnetically stable against the clocking field. Thus, the array will realize cascade-like signal propagation, realizing the AP-state one by one.

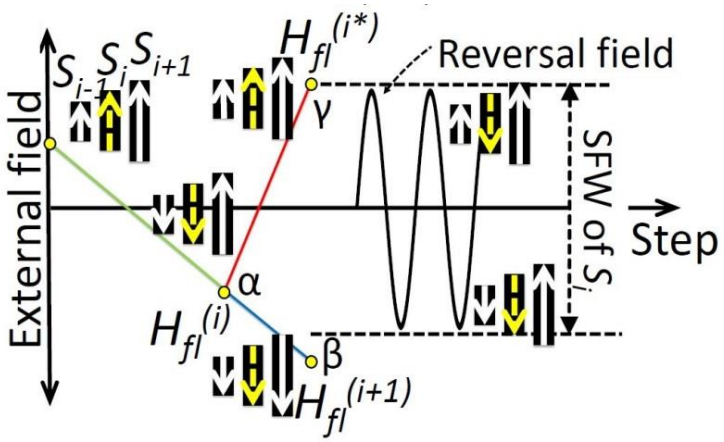

Fig 3.3 The array magnetic state (only three elements are shown here). S_i (highlighted with yellow dotted arrow) and its antiparallel state with S_{i+1} will remain if the reversal field is within its stable field window. The two cases marked on the right side indicate that S_i and S_{i+1} will stay unchanged.

To demonstrate this cascade-like signal propagation, we modeled a chain of five rectangular elements, with the same short axis length (100 nm), and the long axis length varying from 600 nm to 200 nm corresponding to a gradually decreasing K_S. Reversal field, 45° off the

hard axis, was applied with progressively reduced amplitude from 750 Oe down to 600 Oe, as shown in fig 3.4(a). The dotted line represents the field magnitude required when applied at 5° off the hard axis, suggesting that approximately half the field magnitude is required if applied 45° off the hard axis. Figure 3.4(b) shows the magnetic state at different steps, suggesting a cascade-like AP-state evolution from right to left. There are two points worth mentioning here: (a) only if the reversal field drops into the SFW of S_i can it reach the stable final state, i.e. the amplitude of the reversal field should be smaller than the minimum of $H_{fl}^{(i^*)}$ and $H_{fl}^{(i+1)}$; (b) the SFW varies for magnets with different K_S and is largest for S_6 and smallest for S_2. Thus, S_6 would be the first to reach its final state with S_2 being the last one. Additionally, to test the misalignment tolerance, we simulated the field 42° off the hard axis. This 3° variation, corresponding to the typical fabrication misalignment, does not affect correct signal propagation. Thus, the 45°-reversal field achieves both smaller field and higher misalignment tolerance within an array, *i.e.* more reliable signal propagation and lower energy consumption.

To further demonstrate the progressive switching of elements in this novel architecture, we fabricated and tested Fe nanomagnet arrays. Reversed magnetic field 5° off the hard axis as the simulation [fig 3.4(a)] was applied. Figure 3.4(c) shows the scanning electron microscope (SEM) and the MFM image of the Fe nanomagnet array corresponding to steps A-E. It clearly shows the evolution of the magnetic state to the AP-state, suggesting cascade-like signal propagation. In summary, the reversal field was demonstrated to facilitate signal propagation in this shape-tuned nanomagnet array.

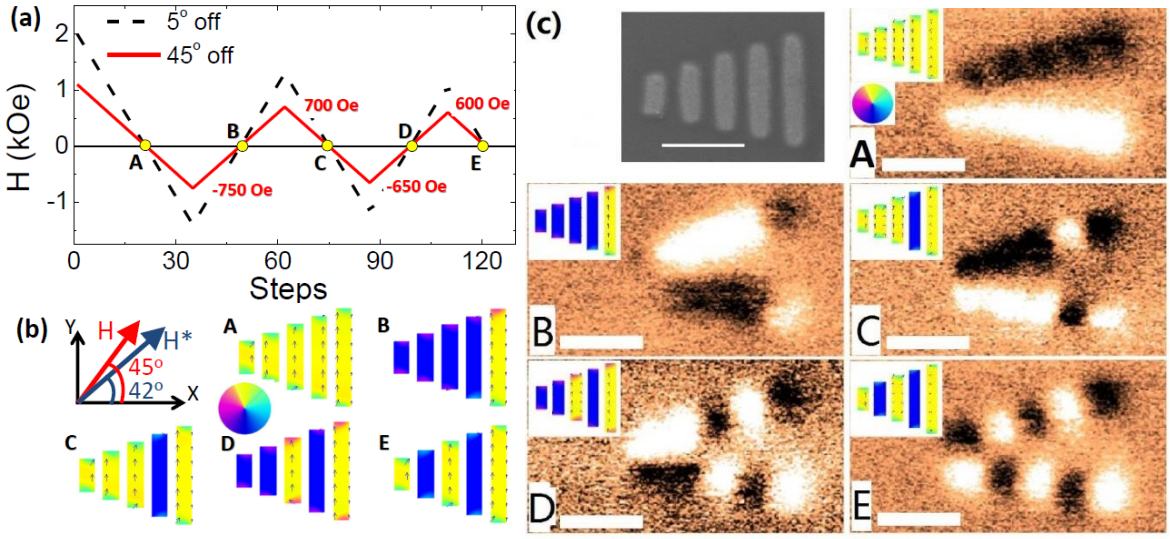

Fig 3.4 (a) The 45° reversal field employed with progressively reduced amplitude. (b) Simulated magnetic states corresponding to different steps in (a). Both 42° and 45° offset with respect to the hard axis was tested. (c) (top-left) SEM image of the patterned array; A-E: Simulated magnetic state (inset) and the corresponding MFM image for different steps in (a). As the amplitude of the field is reduced, each element is aligned antiparallel with its right neighbor, forming a cascade-like switching from right to left. The magnetization direction is indicated by the color wheel or overlaid arrows. The scale bar stands for 500 nm.

3.2 MQCA logic

As discussed in chapter 1, a clocking field is required for MQCA logic, while a fabrication misalignment makes such MQCA logic practically challenging. Based on the discussion above, however, the novel 45° clocking architecture, suggesting a cascade-like signal propagation, would help solve the misalignment problem. In the rest of this chapter, we propose a misalignment-free configuration where the least number of field reversals with reduced amplitude is required for a wide range of θ. A clocking field applied at 45° off the hard axis was designed by micromagnetic simulation and tested with lithographically fabricated elements and arrays. Correct signal propagation can be achieved within an array at both 42° and 45°- off the

hard axis. In other words, clocking field with randomly distributed misalignment less than 3° would not block the correct signal propagation and the field is both more efficient and energy saving. Further, studies of majority gates for the OR logic operations showed correct output of logic function. We further designed and fabricated an all-magnetic full adder based on the 45° field, which paves way for the practical application of MQCA logic.

3.3 Signal propagation in nanomagnet arrays

3.3.1 Experimental details

Experimentally, we used e-beam lithography (EBL) with Polymethyl-methacrylate (PMMA) / LOR 1A (MicroChem Corp., Newton, MA) bilayer resist for pre-patterning. Selective wet-etching of the LOR 1A underlayer by TMAH helped introduce the undercut profile, which facilitates clean lift-off and prevents sidewall deposition, as discussed in chapter 2. A magnetic layer 20 nm-thick Fe, with a 3 nm-thick Au cap, was deposited using ultra-high-vacuum ion beam sputtering system (UHV-IBS) with base pressure better than 5×10^{-8} Torr. The magnetic configuration at remnant state was investigated by scanning electron microscopy (SEM) and magnetic force microscopy (MFM).

3.3.2 Logic propagation with 2 different inputs

The MQCA logic architecture of a nanomagnet array was simulated with a horizontal nanomagnet placed at the long end as the input in order to raise only one ground state, and signal is expected to flow unidirectionally from the higher anisotropic elements to lower ones. Reversed magnetic field 5° off the hard axis [fig 3.4(a)] was applied in this simulation. The first turn of the

reversal field at -1400 Oe set the input element to the left direction, followed by the flipping of S_6, which has the largest aspect ratio of 6:1, to the corresponding state that triggers the signal propagation. After that, the clocking field shows no more influence on S_6 and the input signal from the horizontal element is received. Both structures showed the correct signal output at the short end of the array disregarding the field misalignment, as shown in fig 3.5(a)&(b).

We also modeled the traditional logic without shape-tuning or reversal clocking field. First, array with no tuned shape was tested [fig 3.5(c)]. Signal failed to propagate down to the left under the same reversal clocking field. No cascade-like signal propagation was observed. Actually, it is the shape asymmetry that helps the signal move down in one direction, but not in the reverse, guaranteeing the cascade-like signal propagation. Also, a non-reversed clocking field with 5° misalignment was tested [fig 3.5(d)] and all the nanomagnets flipped up to the misaligned direction. Thus, it is confirmed that a combination of the shape tuning and the reversal clocking field are critical for signal to propagate against misalignment.

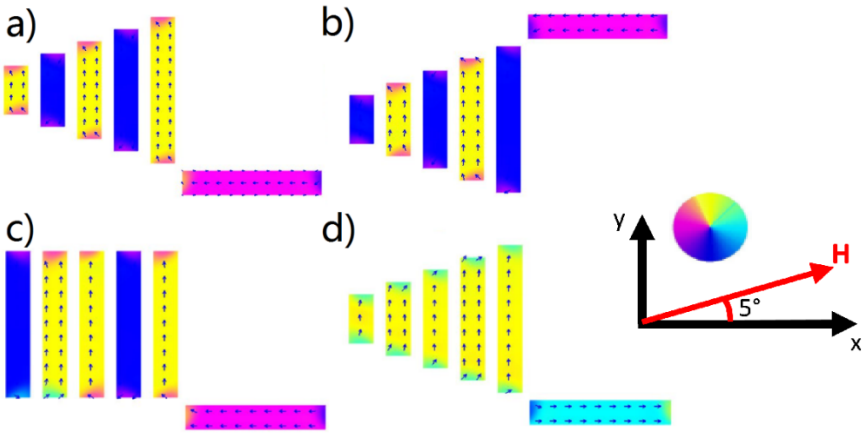

Fig 3.5 (a)&(b) Simulated MQCA logic structures with different input using the reversal clocking field. Both senarior shows correct output according to different inputs, suggesting a misalignment free mechanism. (c)&(d) Control architectures. Signal fails to propagate when there is no shape tuning (c) or no reversals in the clocking fields (d); some elements rested in the grounding states before the signal reached to them.

3.4 Logic operation in majority gates

Next, we studied validity of this 45°-clocking field for logic operations when applied to majority gates. The same reversal clocking mechanism combined with shape-tuned nanomagnets array was employed. By setting one input as 0/1 [or down/up in fig 3.6(a)], the majority gates can execute OR/AND function. For example, if we preset the middle horizontal bar (X) at the upper position [fig 3.6(a)], we could list the 4 possible input combinations for the other two. As a result, the true value chart in fig 3.6(b) indicated OR function.

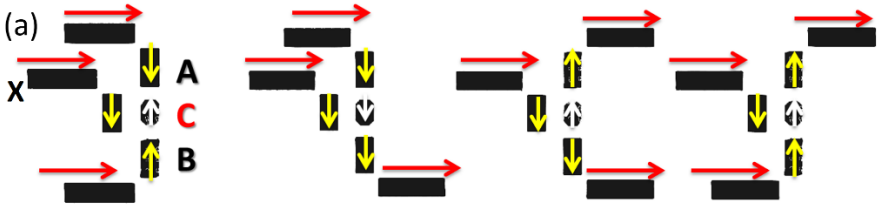

(b)

	Logic 1	Logic 2	Logic 3	Logic 4
Input (A)	0	0	1	1
Input (B)	1	0	0	1
Output(C)	1	0	1	1

Preset
Input
Output

Up: 1
Down: 0

Fig 3.6 (a) 4 possible combinations: (1,1), (0,1), (1,0) and (0,0) for inputs (A)&(B). (b) True value chart indicating output (C) based on the four input combinations. By fixing the element X, we achieve OR function logic with two valid inputs (A)&(B), selected by the horizontal bar at the beginning.

Different from the nanomagnet array, majority gates require coordinated rearrangement of the elements for both signal input and logic operation which would weaken the dipole coupling between elements and requires accurate field tuning down to tens of Oersteds. The reversal field with amplitude decreasing from 700 Oe down to 490 Oe [fig C-7(a)] was used to simulate all four input combinations for the OR gate, with the bit value = 0(1) assigned to magnetization direction down (up) along the easy axis for two vertical inputs (above and below)

and the center output. The final stage is shown in fig C-7(b-e), suggesting correct logic operation under 45° clocking field.

Experimentally, we demonstrated 2 input combinations using EBL and UVH-IBS. The magnetic configuration were observed by magnetic force microscopy (MFM). Fig C-7(f)(j) shows SEM images of two gates fabricated for logic operation test. The MFM images on the right are the magnetic evolution corresponding to stage A-C in fig C-7(a). Even though correct logic operation is achieved by only two reversals, the complete clocking field in fig C-7(a) is required for all four input combinations ensuring that the output element finds its ground state. In summary, the 45°-clocking reversal field was demonstrated to facilitate logic operations for majority gates.

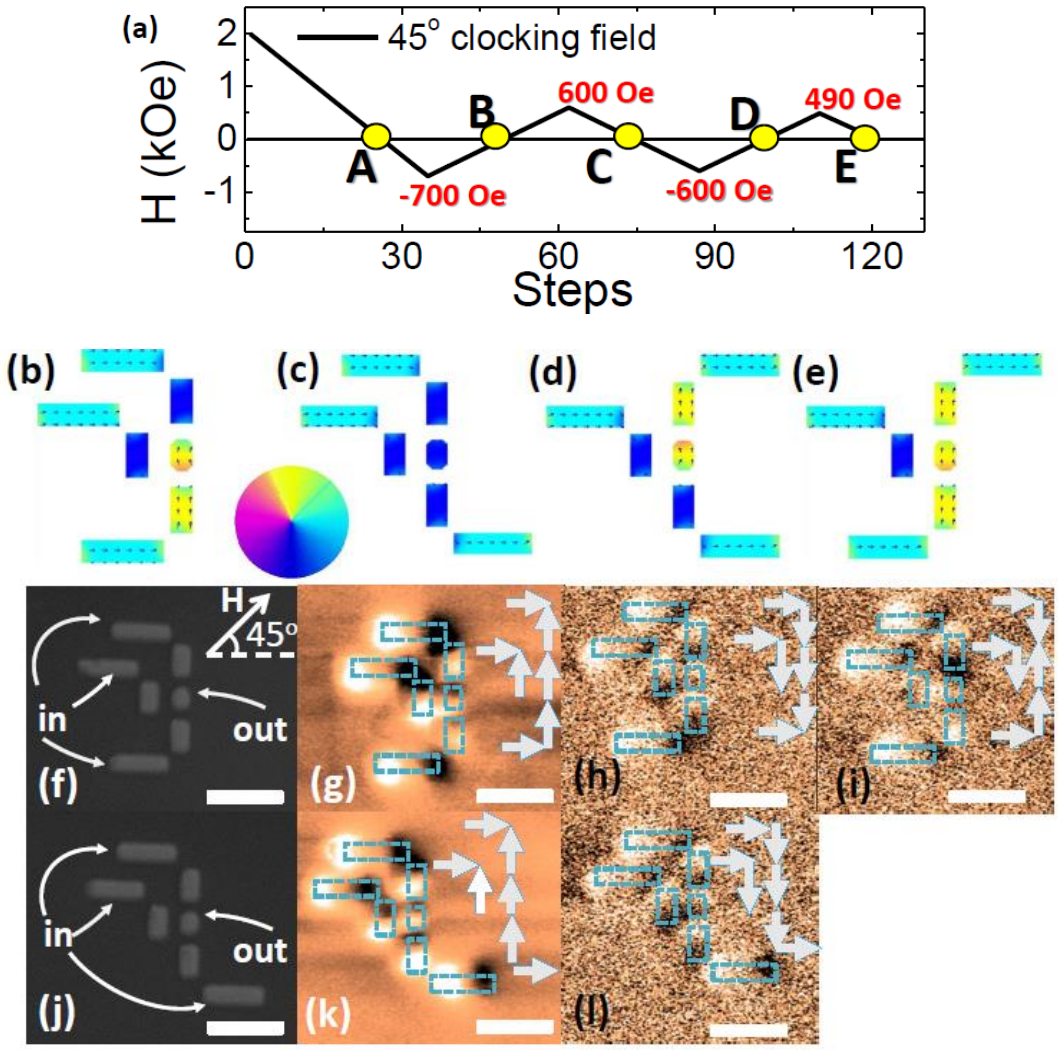

Fig 3.7 (a) The 45° clocking field employed for logic operation. (b)-(e) The simulation results of all four majority gates. (f)&(j) SEM images of lithographically patterned OR gates (only two are demonstrated here), with the magnetic state evolution observed by MFM shown on the right (g)-(i) and (k)-(l), respectively. Again, elements with larger shape anisotropy will stay against the clocking field with reduced amplitude. The magnetic direction is defined as "from white to black" while the arrows serve for visual guidance. The scale bar stands for 500 nm in (f)-(l).

3.5 Full adder and all-magnetic circuit

Further study on MQCA logic requires more complicated functions, such as full adder, for integration with electrical circuit and pipelined logic of data flow [C8]. A binary full

adder works to add up binary numbers and accounts for values carried in/ out [C9]. Although it is straightforward to design such a MQCA full adder based on blocks of *nanomagnet arrays* and *majority gates*, there are few experimental attempts due to the misalignment issue [C9-C11]. For example, error of wrong data-flow directionality occurs under traditional clocking field [C10]. Thus, it is of interest to redesign a full adder that is robust against misalignment in clocking.

We proposed a novel architecture of 3-input full adder based on 45°-clocking field mechanism; the field alters between 0° and 45°-off the x-axis to separate input writing and logic operation. This alternated clocking mechanism facilitates stable logic operations. Moreover, it intrinsically favors unidirectional signal flow and hence requires only 1/3 number of elements compared to a traditional full adder design [C10].

3.5.1 Logic and algorithm

There are two basic architectures in MQCA logic: (a) *nanomagnet array* where the signal propagates, and (b) *majority gate* for logic operation. For a *nanomagnet array*, the dipole field between adjacent elements would facilitate antiferromagnetic (AF) coupling, suggesting an ↑/↓ alternation of magnetization in the chain. Unlike the Coulomb-coupled quantum cellular automata (QCA) [C9] where an inverter is required to reverse the signal, MQCA *nanomagnet array* can achieve the NOT function by simply adding another AF-coupled element into the chain if we define ↑/↓ as 1/0. On the other hand, *majority gates* perform 3-input logic operation; the output is determined by voting among all 3 adjacent elements through the competing dipole field on the center one. Fixing the magnetic state of one input driver as preprogrammable, we could transfer the *majority gates* into a 2-input AND/OR gates. Again, an additional AF-coupled element can bring up logic functions of NAND/NOR. In a word, all five basic binary logic

functions of NOT/AND/OR/NAND/NOR could be realized by the two basic MQCA architectures— *nanomagnet array* and *majority gate*.

Next, a full adder could be realized based purely on these two architectures. A full adder [C9] has three inputs of one-bit number, often written by convention as *A*, *B*, and C_i and two outputs, C_o and *S*. Table 3.1 shows the relation between 3 inputs and 2 outputs.

Table 3.1 True value chart of a 3-input full adder.

Inputs	***A***	0	1	0	1	0	1	0	1
	B	0	0	1	1	0	0	1	1
	$\boldsymbol{C_i}$	0	0	0	0	1	1	1	1
Outputs	$\boldsymbol{C_o}$	0	0	0	1	0	1	1	1
	S	0	1	1	0	1	0	0	1

Conventionally, a full adder is expressed based on 2-input logic functions, which are AND (·) and OR (+). The true value chart (Tab 3.1) can thus be rewritten as

$$\begin{cases} C_o = A \cdot B + B \cdot C_i + A \cdot C_i \ \dots\dots (3.3) \\ S = A \cdot B \cdot C_i + \bar{A} \cdot \bar{B} \cdot C_i + \bar{A} \cdot B \cdot \bar{C_i} + A \cdot \bar{B} \cdot \bar{C_i} \ \dots\dots (3.4) \end{cases}$$

To express this function within 3-input MQCA majority gates [C8], the third input has to be fixed to mimic this 2-input logic, which is inefficient—it requires more gates to express the same function than the conventional 2-input logic gates does. However, a compact algorithm can be achieved if we define the 3-input voting function [C8], which can be expressed as

$$M\ (A, B, C_i) = A \cdot B + B \cdot C_i + A \cdot C_i \ \dots\dots (3.5)$$

On the one hand, the M-function is compatible with the 2-input logic in that the AND/OR function could be achieved by fixing the preprogrammable element, C_i as

$$\begin{cases} A \cdot B = M\ (A, B, 0) \ldots\ldots (3.6) \\ A + B = M\ (A, B, 1) \ldots\ldots (3.7) \end{cases}$$

It is worth mentioning that the NOT function also applies to the new algorithm, where NOT of A is represented by $\bar{A}$. Thus, much higher efficiency can be achieved as we could concisely rewrite the full adder with the M-function as:

$$\begin{cases} C_o = M\ (A, B, C_i) \ldots\ldots (3.8) \\ S = M\left(\overline{M\ (A, B, C_i)}, M\ (A, B, \overline{C_i}), C\right) \ldots\ldots (3.9) \end{cases}$$

Such an architecture [C8] intrinsically require only three 3-input majority gates; it requires fewer gates to achieve the full adder logic function.

3.5.2 Angular sensitivity of switching field

As will be discussed below, our full-adder design requires switching of the clocking field between two axis with 45° difference to each other, thus it is of interest to study the angular sensitivity of nano-elements to switching field. We first simulated the magnetic reversal of a single element in size of 100×300×20 nm^3, predefined with a uniaxial shape anisotropy because of a aspect ratio of 1:3. Predicted by the Stoner-Wohlfarth model, the switching field, H_{sw}, would be minimized when the field is applied 45° off the hard axis. Correspondingly, the angular sensitivity of H_{sw}, $dH_{sw}/d\theta$, should equals zero. To test this idea, we carried out the angular (θ) dependence of the θ-sensitivity of H_{sw}, $dH_{sw}/d\theta$, from 1° to 45° off the hard axis with an angular step of 3° and magnetic field step of 1 Oe. The $dH_{sw}/d\theta$ would represent the misalignment tolerance—that a lower $dH_{sw}/d\theta$ indicates more stable magnetic switching against field misalignment, hence is practically more favorable. As shown in fig 3.8, the misalignment sensitivity, $dH_{sw}/d\theta$, reduces from 176 Oe/° to 0.2 Oe/° when the field direction changes from 1°

to 45° off the hard axis, suggesting a totally different switching behavior when the clocking field alters between 0° and 45° along the hard axis. This makes possible the separation between *input writing* and *logic operation*, as will be discussed below.

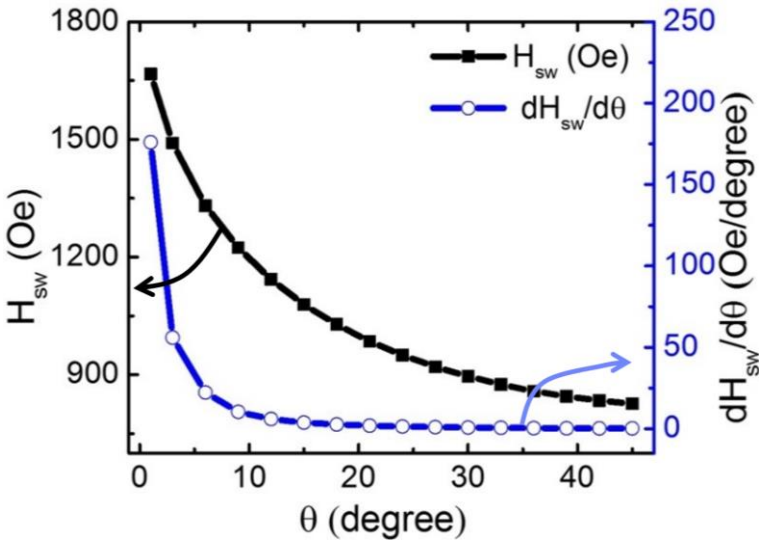

Fig 3.8 Misalignment sensitivity of the switching field, $dH_{sw}/d\theta$, for an element with aspect ratio of 1:3.

3.5.3 Layout design of full adder

Based on the M-function, (Eq. 3.5), using 3-input majority gates, we demonstrated the architecture design of a full adder using only three majority gates, as shown in fig 3.9(a). Next, the schematic design of the full adder is realized relying on the 45° clocking mechanism [fig 3.9(b)]. The clocking field is switched between 0° and 45° off the x-axis in order to alternate between *input writing* and *logic operation*. The full adder is composed of (1) writing part of input drivers (ABC_i) with hard axis aligned 45° against x-axis, and (2) operation part of three 3-input majority gates with output elements of (C_oS). First, for the *input writing* part, different drivers (ABC_i) were programed independently. Their aspect ratio and correspondingly the shape anisotropy are different, ensuring them to be switched selectively by tuning the field amplitude;

higher aspect ratio yields higher writing field. Then for *logic operation*, the field was turned to 45°-off the x-axis, in order to maximize the misalignment tolerance for majority gates, ensuring a unidirectional signal propagation to the output elements of C_o and S.

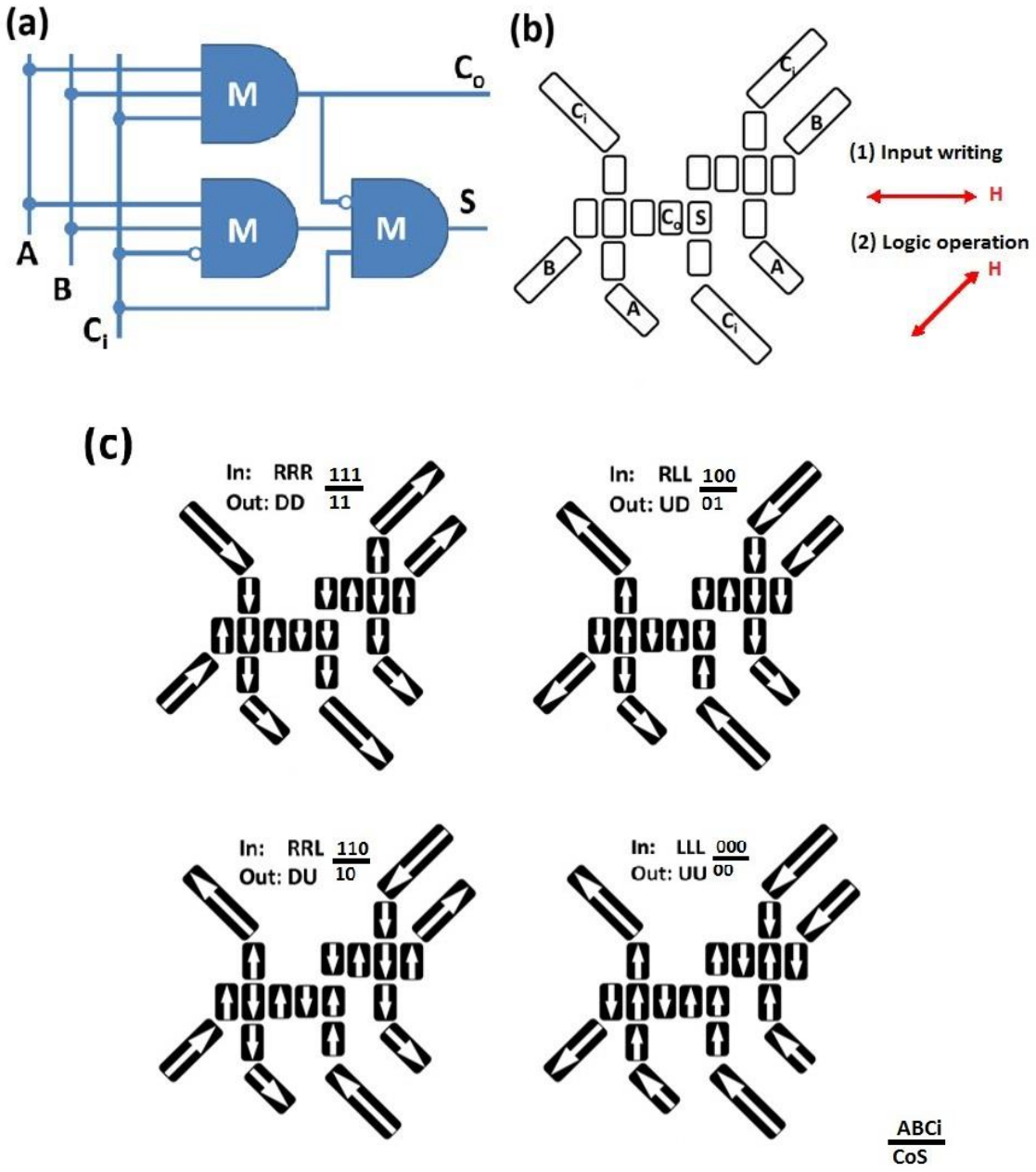

Fig 3.9 (a) Architecture design of a full adder based on three 3-input majority gates; (b) schematic design of the full adder relying on 45° clocking mechanism; (c) demonstrations of the correct output (with ↓:1 and ↑:0) based on the input (with ↘, ↗:1 and ↖, ↙:0).

We use four different inputs combination (ABC_i) as demonstration in fig 3.9(c). In the upper-left scenario, for example, all input elements are aligned to the right direction (either upper-right or lower-right), thus we have (ABC_i) equals (111). Correspondingly, we have both output elements (C_oS) pointing down as (11). In the upper-right scenario, only the input driver *A* is pointing rightward, while both *B* and C_i are pointing either upper-left or lower-left, indicating an input combination of (100). As a result, the output turns out to be (01)—both elements pointing downward. Similar to that, inputs of (011) and (000) leads to outputs of (10) and (00), respectively. In a word, the input drivers are defined by the clocking field and recorded by their final magnetic direction— that right (either upper-right or lower-right) indicates 1, and left (either upper-left or lower-left) indicates 0, and output is recorded as 1 when the magnetic moment is pointing downward for both C_o and *S* in fig 3.9(c).

To test this configuration, we modeled a full adder with input (111). Instead of presetting the input drives (ABC_i) along the positive x-axis (either ↘ or ↗ magnetic direction), for the *input writing* we redirected the field along the negative y-axis (either ↙ or ↘ magnetic direction) in order to optimize the system thermal efficiency. On the one hand, the identical output would be the expected (11). On the other hand, this *input writing* redirection is advantageous in spreading out the heat dissipation generated by the clocking current. In other words, in this specific scenario, it reduces the overall duty cycle for the x-axis field generated by the y-axis copper lead [C12]. As a matter of fact, continuous signal processing usually gives pulse currents in ~GHz frequency and ~10^6 A/cm^2 current density [C13] in the copper leads. Such a redirection will reduce the use and hence the heat dissipation on the heavily used y-axis copper lead by using the x-axis copper lead instead.

Figure 3.10(a) shows the magnetic field applied to the unit. At the beginning, a field of -1000 Oe along the y-axis was applied to preset the input drivers. Next for the operation, reversal fields with amplitudes of 620 Oe and 502 Oe were applied 45° off the x-axis. At each field cycle only elements with lower shape anisotropy can flip until they reached the right position after which they will freeze at lowering clocking field. Inset of fig 3.10(a) shows the simulated magnetic configuration after each clocking cycle. Stage 3 (S3), corresponding to the final stage when the clocking field was removed, demonstrates correct output. To further test the effect of a misaligned clocking field, an angular variation of ±1.5° was carried out and led to the same output, suggesting a robust design with high misalignment tolerance.

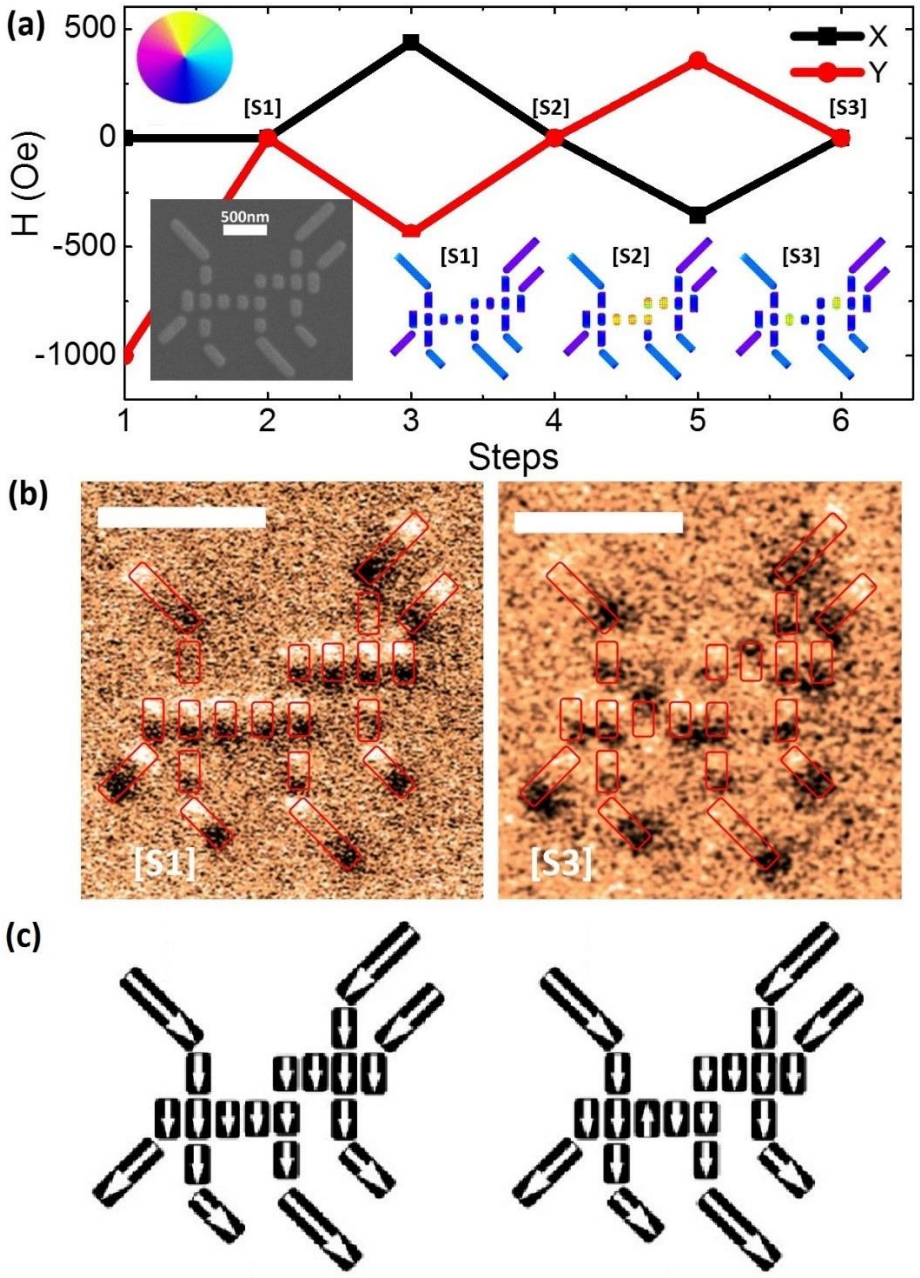

Fig 3.10 (a) Reversal field used in the simulation for the full adder operation and (inset) corresponding magnetization states and color wheel representing the magnetization direction. (b) MFM images of the stage 1 [S1] and stage 3 [S3] for a 20 nm-thick Fe sample fabricated by electron-beam lithography, with the scale bar representing 1 μm; (Inset of (a)) SEM image of the lithographically fabricated sample. (c) Demonstrations of the correct output according to (b).

Next, we fabricated Fe nanomagnet arrays. The SEM image of the full adder is shown in the inset of fig 3.10(a). A continuous magnetostatic reversal field, the same as in simulation [fig 3.10(a)] was applied. The magnetic state after (1) *input writing* and (2) *logic operation* were carried out, as for S1 and S3, respectively [fig 3.10(b)]. Magnetic state of elements was observed by the white/black contract in the MFM image. Assuming the magnetization direction pointing from white to black, we observed the correct output of (11) resulted from input of (111), as shown in fig 3.10(c). In summary, the 45° clocking mechanism was demonstrated to facilitate a robust full adder.

In summary, practical application of MQCA logic requires a robust clocking mechanism with low error rate. Our full adder design with 45° clocking field enables unidirectional signal flow and correct output. It is also advantageous in lowering heat dissipation and higher integration density. Thus, this misalignment-free full adder using 45° clocking mechanism paves way for the application of MQCA.

3.6 Discussion

Finally, we would like to discuss the feasibility of this 45°-clocking field. The key advantage of this configuration over the traditional clocking field is the misalignment-free mechanism. It was estimated [C14] that the misalignment angle θ should satisfy $tan\theta<(H_{align}^{easy}/H_{align}^{hard})<<1$ for traditional clocking fields that is applied along the hard axis, where H_{align}^{easy} and H_{align}^{hard} represents the fields required to magnetize the element along the easy and hard axis, respectively. The requirement for the highly accurate directionality is practically challenging. The 45°-clocking field solves this problem intrinsically by applying the

field along the angular-insensitive direction of 45° with respect to the hard axis. Furthermore, the reduced field amplitude is more efficient and energy saving.

Next, for proper functioning of majority gates, accurate field tuning down to tens of Oersteds is required. This is because the dipole coupling is weakened when the elements are not aligned parallel, affecting the corresponding energy ground state. This is a general problem for most MQCA architecture other than the nanomagnet arrays. However, it is feasible since the magnitude of the current generating the clocking field can be controlled with a much better accuracy. To generate a magnetic field ~5×10^3 Oe along the top surface of the copper wires, a current density ~10^6 A/cm^2 is required [C15]. Considering a normal current generator [C16] with capacity of a pulse current of 50 A and step of 0.2 A, this field could be achieved since the accuracy is better than 400 A/cm^2, or 2 Oe. Thus, our design is practically applicable.

One of the drawbacks of this configuration is that it requires N-times field reversal for signal to propagate down an array with N-elements. However, N can be minimized by breaking a long chain of magnetic elements down to several short ones. Correspondingly, the short chains only communicate at the connecting part, where a local clocking field is applied individually to only one element. Additionally, since the signal propagates unidirectionally from higher anisotropic element to lower ones, signal refreshment from lower to higher ones is required and can be achieved using similar mechanism, that a local field is applied individually to the output element alone [C14]. Demanding more elaborate fabrication, this local clocking field may only be used for chain breaking down and signal refreshment. As reported [C13], the switching occurs below 1 ns, suggesting GHz clocking frequency. Thus the influence of this local clocking on the circuit speed will be very limited.

Next, to implement the proposed architecture into a full circuit, a local clocking field is required, which is normally generated by copper wires embedded underneath. The wire current should be perpendicular to the 45° clocking field and confined within a local area (~1.5um×1.5um). This copper wire can be realized through the standard fabrication process [C17]. A thicker wire with high aspect-ratio sidewalls, combined with high-permeability claddings (such as supermalloy) [C18], would help retain the reluctance and reduce the power consumption as well.

The mechanism we proposed requires smaller clocking field, about 50 % in amplitude, to reverse the nanomagnets. In practice, it indicates a reduction of current density [C12] of the order of ~10^6 A/cm^2 that would help further optimize the heat dissipation and extend the device lifetime.

Further, our design requires much fewer elements, a factor of 3 less than the conventional one [C10], indicating higher integration density and less fabrication processes. Most importantly, the 45° clocking mechanism guarantees unidirectional signal flow, preventing any faulty signal introduced by either data back-flow or noise.

The integration of MQCA logic with current Complementary Metal-Oxide Semiconductor (CMOS) technology requires a robust reading/writing system, which has been designed based on MTJ [C18] and spin-transfer torque [C19], where the magnetic state of individual element is electrically measured [C20]. On the other hand, employment of spin Hall Effect has been reported to deliver a spin torque required for clocking [C21]. For example, the magnetization of CoFeB elements has been reported to align to their NULL state by a current through the underlying Ta wire [C22]. The current required is much smaller than that from a copper wire. All

these mechanisms, if pursued seriously, would make it possible to integrate the MQCA device into the CMOS circuits.

Chapter 4[*]

MAGNETIC RECORDING AND EXCHANGE INTERACTION

4.1 Exchange interaction in PMA system

The magnetic reversal in perpendicular magnetic anisotropy (PMA) system relies strongly on the areal size. For a continuous film, the reversal starts with nucleation of a small reversed volume followed by rapid domain wall propagation, where the angular dependence of switching field H_{sw} typically shows a $1/cos\theta$ relation [D1][D2]. For a patterned dot array, however, the magnetic reversal would be totally different, where the domain wall motion is hampered and the dots are isolated from each other. The difference would be the most for dots within *the single domain limit*, where domain wall is eliminated in the equilibrium state because it is energetically unfavorable [D3]. Thus, the angular dependence of H_{sw} of patterned samples may show a Stoner-Wohlfarth behavior with a minimum at 45^o to normal, as discussed previously in chapter 3.

[*] Publications:

- Large-area patterning of sub-100 nm L10 FePt dots array, Zheng Li, Wei Zhang and KM Krishnan, AIP Advances 5 087165 (2015)
- Effect of Pt addition on perpendicular anisotropy of L10 FePd thin films, Zheng Li, Wei Zhang, Alexandru Stancu, Mark Bowden, S. Manandhar, V. Shutthanandan, KM Krishnan, under preparation

Further, nanofabrication and related processing make the size-dependent reversal process even complicated; the switching field, as well as its distribution that describes the H_{sw} uniformity over all elements, might change dramatically in patterned dot array [D4], as shown in fig 4.1. For example, ion-bombardment results in edge defects and damage during patterning, and such defects could pin the domain walls from moving [D5][D6]. Also, the magnetic switching is influenced by the material intrinsic properties, such as the anisotropy and saturation magnetization, as well as their spatial variation in continuous films [D4]. This influence is often buried by the domain wall propagation in thin film samples due to the strong exchange coupling and thus remains elusive. However, these intrinsic property could be probed in patterned dots samples where the domain wall propagation is suppressed [D7]. In short, it is of scientific interest to study the magnetic reversal behavior of patterned dots arrays for a perpendicular magnetic anisotropy (PMA) system, where the domain wall motion is hampered.

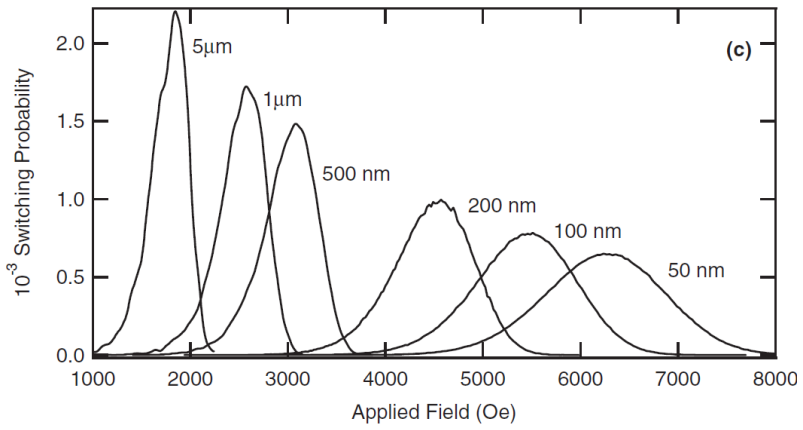

Fig 4.1 (Adopted from ref D4) Summary of the simulated switching probability as a function of the size of the dots within the array. The spacing between dots was kept large enough so that dipole interaction between adjacent dots could be neglected for all arrays. The curve shows a broader distribution over the applied field for dots that are in smaller diameter.

4.2 PMA recording and $L1_0$ system

From an industrial perspective, the concept of utilizing PMA materials for super-high density magnetic recording has drawn people's attention for decades [D8-D10]. Among all the PMA material candidates for the recording media, $L1_0$ ordered epitaxial thin films (such as FePt and FePd), with the c-axis being the easy axis of magnetization, have generated most interest [D11-D13]. Figure 4.2(b) shows the atomic structures of $L1_0$ FePt, where Pt and Fe atoms form a superlattice by alternating the atomic layers in the [001] direction. As a comparison, the phase that lost this superlattice periodicity is called A1 structure [fig 4.2(a)].

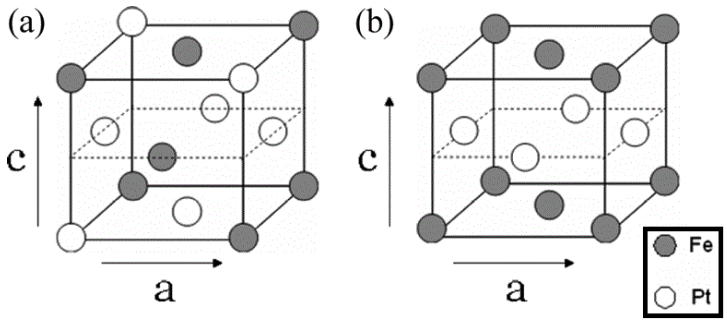

Fig 4.2 Two crystal structures of FePt. (a) A1 structure (face centered cubic, *fcc*) where a = c; Fe and Pt atoms are randomly distributed. (b) $L1_0$ structure (face centered tetragonal, *fct*) where a $\neq$ c.

Among all $L1_0$ structured thin films, the $L1_0$ $Fe_{50}Pt_{50}$ (K_{mc} = 6.6×10^7 ergs/cc [D14]) has drawn the most attention because it requires moderate fabrication temperature (<500°C) and provides robust performance for PMA system, as will be discussed later in this chapter. Besides FePt, other candidates are also desired for the exploration of different PMA system for potential applications, such as exchange coupled composite (ECC) [D15], as previous discussed in *chapter 1.6*. Thus, we also carried out studies of the FePd system in this thesis, which has drawn little attention so far. With Palladium (Pd) in the same column but with a lower atomic number than

Platinum (Pt), FePd has the same $L1_0$ ordering. However, Pd has one less electron shell than Pt [D16], and hence a smaller atomic size that makes A1-$L1_0$ phase transformation more difficult for FePd than for FePt. Thus, it is difficult to fabricate high quality $L1_0$ FePd thin films. To address this issue and enhance magnetic performance, we introduced ~5% Pt addition for ternary effect, as will be discussed in section 4.3.

The discussion in the rest of this chapter is in three parts. First, we show that the $L1_0$ FePd thin film with Pt addition is a good candidate for high performance PMA system. Next, $L1_0$ $Fe_{50}Pt_{50}$ thin films are used to study the effect of patterning within the *single domain limit* on the magnetic reversal of PMA thin films. Then, large-area patterning of sub-100 nm epitaxial $L1_0$ FePt dots array via nanoimprint lithography, as well as FePt/Co exchange coupled heterostructure, are carried out to investigate their suitability for the application of bit-patterned media (BPM) recording.

4.3 $L1_0$ FePd thin film with Pt addition

4.3.1 Ternary effect in $L1_0$ epitaxy system

Earlier works [D17-D18] have examined the influence of certain additive elements on the properties of $L1_0$ FePt thin films. For example, Cu, Ni and Cr are totally soluble in FePt and have been reported to significantly improve the $L1_0$ order, forming ternary alloys [D18-D20]. On the other hand, although $L1_0$ FePd has magnetic properties similar to $L1_0$ FePt, there are only few studies of $L1_0$ FePd thin film system and even fewer of $L1_0$ FePdX ternary systems [D21-D23]. In this chapter, we show the study of FePd binary system with Pt additions (~5%), which demonstrates an enhancement in $L1_0$ ordering. A soft magnetic phase is observed and its

variation after annealing at 350°C for 1h is examined using both major/minor loops and first order reversal curve (FORC) diagrams [D24, D25].

4.3.2 $L1_0$ FePdPt thin film

FePd films were prepared using an HV ion beam sputtering system [D26,D27]. Pt additions were selectively doped by attaching an elemental chip onto the surface of the $Fe_{50}Pd_{50}$ (at. %) target. 10 nm FePdPt film was deposited on MgO (001) substrates at 480°C with a base pressure below $5x10^{-8}$ Torr. The samples were cooled down to room temperature, then capped with 3 nm-thick Ag in the vacuum chamber. The ternary composition of the deposited film was determined to be $Fe_{45.4}Pd_{50.1}Pt_{4.5}$ (at. %) by energy dispersive x-ray spectroscopy (EDS). The as-grown sample was cut into two pieces, subject to different annealing processes and labeled as S_{asgrn} (no annealing) and S_{ann} (annealed at 350°C for 60 min in vacuum better than 5×10^{-8} Torr). Both Rutherford backscattering spectroscopy (RBS) and X-ray photoelectron spectroscopy (XPS) analysis of the sample was performed to verify if the Ag capping layer has diffused in the annealed sample. A binary FePd reference sample without Pt addition (S_{ref}) was also deposited.

Figure 4.3(a) shows the XRD θ-2θ patterns. For both samples, clear (001), which is only allowed in the ordered $L1_0$ phase, and (002) peaks of FePdPt were observed, as well as MgO (002) and Ag (002) peaks. Texture of FePdPt (001) is further evidenced by the full width at half maximum (FWHM) of the rocking curve of S_{asgrn} [fig 4.3(b)] of about 2°. The in-plane Φ-scan of S_{asgrn} [fig 4.3(c)] confirmed the epitaxial relationship of MgO (001) [100]||FePdPt (001)[100]. The unit cell of S_{asgrn} was determined to be tetragonal with lattice parameters $a = b$ =3.86 Å, c = 3.69 Å and c/a = 0.956, determined from the (002) and (202) Bragg peaks. This decreased axial ratio (c/a) compared to the bulk $Fe_{50}Pd_{50}$ (a=b=3.85 Å, c=3.72 Å, c/a=0.966) [D28] is likely due to

the strain induced by the 8.5% mismatch between MgO/ FePd lattice [D29] and may be partially released in the annealed sample S_{ann}.

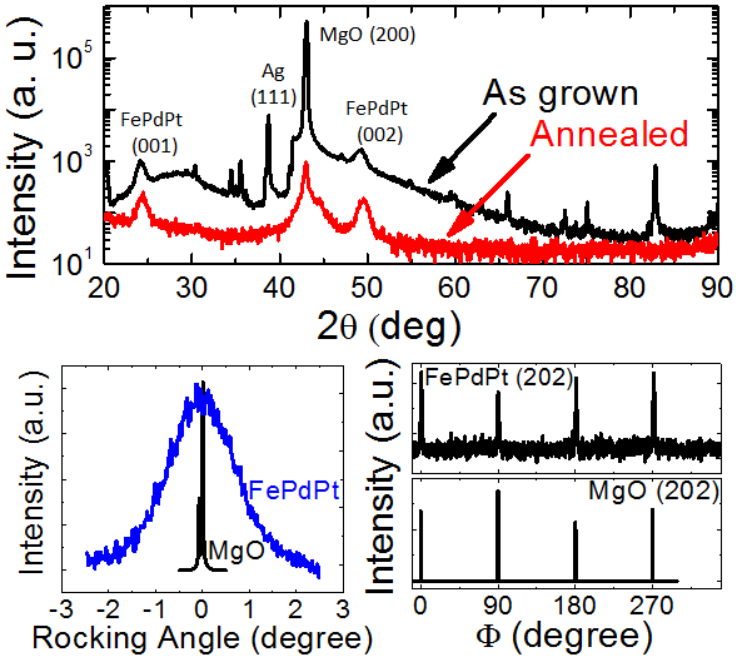

Fig 4.3 XRD measurements, (a) θ-2θ scan of sample as-grown S_{asgrn} and annealed S_{ann}. Clear FePdPt (001) and (002) peaks confirm the $L1_0$ chemical ordering. (b) Rocking curve suggesting a good texture, and (c) Φ-scan of S_{agrn}, indicating good epitaxy of FePdPt (001).

After annealing, θ-2θ peaks related to the capping [Ag (111), (220) and (222)] disappeared, leaving only the FePdPt film texture along (002). However, both RBS and XPS data for S_{asgrn} and S_{ann}, as shown in Appendix-3 [D30], indicates that Ag only redistributed on the top layer. Thus the Ag atoms remain as the top layer, albeit redistributed in an amorphous fashion, and have no influence on the chemical ordering of FePd layer after annealing. The peak intensity ratio (I_{001}/I_{002}) in the θ-2θ scan is a good indicator for FePdPt $L1_0$ chemical ordering because the (001) peak is forbidden unless there is $L1_0$ ordering. An increased (I_{001}/I_{002}) is observed for S_{ann} from 0.60 to 1.29 after annealing. On the other hand, this dramatic increase was not observed in

the FePd binary control sample, where (I_{001}/I_{002}) only changed from 0.53 to 0.71. In short, our results show that Pt addition could facilitate FePd $L1_0$ ordering at a temperature as low as 480°C , which could possibly be related to the formation of the FePdPt ternary phase.

4.3.3 Annealing effect on $L1_0$ FePdPt system

Figure 4.4(a) and (b) show the hysteresis loops for S_{asgrn} and S_{ann} with external field applied normal to the film plane. Coercivity, H_C= 9.10 kOe for S_{asgrn} was observed, which is higher than the previously reported value of 1.2 kOe [D22] for FePd thin films. The anisotropy field, H_A=19.8 kOe, defined as the saturation field along the hard axis (in-plane here). It suggests an easy axis out of plane, and thus clearly shows perpendicular magnetic anisotropy (PMA). A kink-shaped loop was observed for both S_{asgrn} and S_{ann} around zero-field, indicating that a soft magnetic phase reversed at lower field. This soft phase could be further illustrated by the sharp peak in the first derivative, *dM/dH,* curve [inset of fig 4.4(c)&(d)]. A sharply increased zero-field peak is observed for S_{ann} compared to S_{asgrn}, indicating a soft phase expansion, perhaps because of volume increase, after annealing (S_{ann}). This soft phase expansion would possibly facilitate the lateral magnetic domain wall propagation and is discussed below.

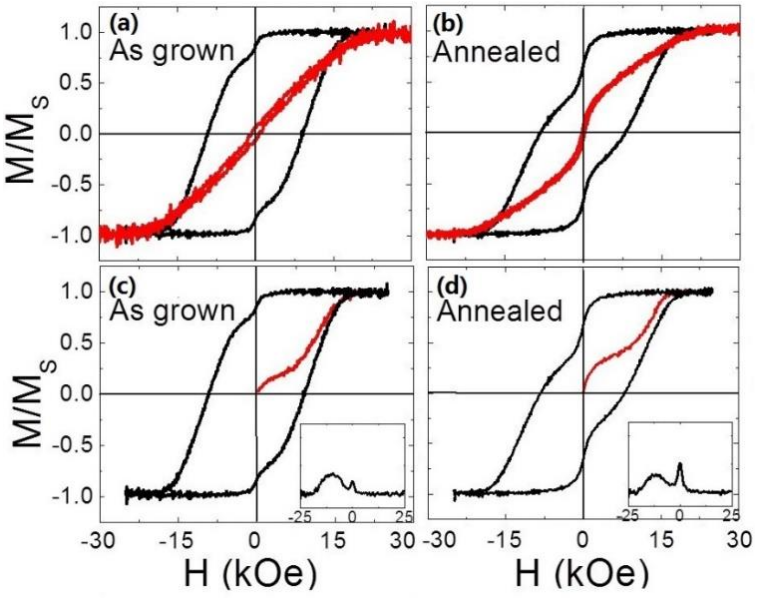

Fig 4.4 (a)& (b) Hysteresis loops of S_{asgrn} and S_{ann} along both easy axis (out-of-plane, black) and hard axis (in-plane, red). (c)&(d) Corresponding initial curves (red). Inset of (c)&(d) is the first derivative, d*M*/d*H*, of the descending branch.

Further, we measured the initial/virgin curve after AC demagnetization, as shown in fig 4.4(c)&(d). AC demagnetization is a process that the field is keeping reversed with field amplitude decrease gradually, after which the sample is expected to reach a state with zero remnant magnetization. The initial curve is measured right after that by increasing the field from zero to saturation in one direction. For S_{asgrn}, the magnetization increased slowly at the beginning up to a certain point, followed by a rapid saturation. This turning point could be related to the pinning sites such as grain boundaries or defects, hindering domain wall (DW) propagation [D31]. On the other hand, initial curve of S_{ann} indicates an easy magnetization process, typically coming from DW nucleation and propagation [D31]. Considering the reason for this annealing facilitated DW propagation, it could be possibly related to the soft phase expansion discussed above. The magnetic soft phase may switch at small field and with DW entering the hard phase it helps

reverse the hard phase at lower field. Thus, DW propagation into the hard phase is easier with an expanded soft phase.

4.3.4 FORC diagram analysis

To confirm this hypothesis, we carried out first order reversal curve (FORC) measurements for both S_{asgrn} and S_{ann}. FORC diagram eliminates the purely reversible contributions in the magnetic switching process, which would reverse back to its initial state when the external field is removed. FORC diagram has been widely used as a visual 'fingerprint' to study the magnetic reversal mechanism [D24,D25]. Details of FORC as a method to characterize magnetic materials are discussed in Appendix-1. Figure 4.5(a) indicates fully decoupled soft/hard phases in S_{asgrn}. Regarding the origin of the soft phase, it is possibly comes from the large surface energy difference between MgO and FePd, leading to in-plane growth of *c*-axis at the interface and a corresponding in-plane soft phase [D31], which would correspond to a granular film morphology; further experimental investigation, such as cross-sectional TEM, may be required to confirm this. Moreover, a connection between soft/hard phase reversal-center was observed after annealing [fig 4.5(b)], indicating a sustained irreversible switching. This continuous switching is partially attributed to an increased soft/hard phases exchange coupling. To further explain the FORC diagram, we employed the Preisach model [D32], where the moving constant, α, describing the mean field interactions, was measured. As marked by lines labelled "1" and "2" in fig 4.5(a)&(b), α represents the rotation of the irreversible switching due to magnetic interactions. A reduction of α was observed after annealing from 13.3° (α_1) to 12.9° (α_2), suggesting a positive mean field. It is consistent with previous conclusion that interphase

exchange coupling would introduce a coherent rotation within magnetic element and suggest a positive mean field.

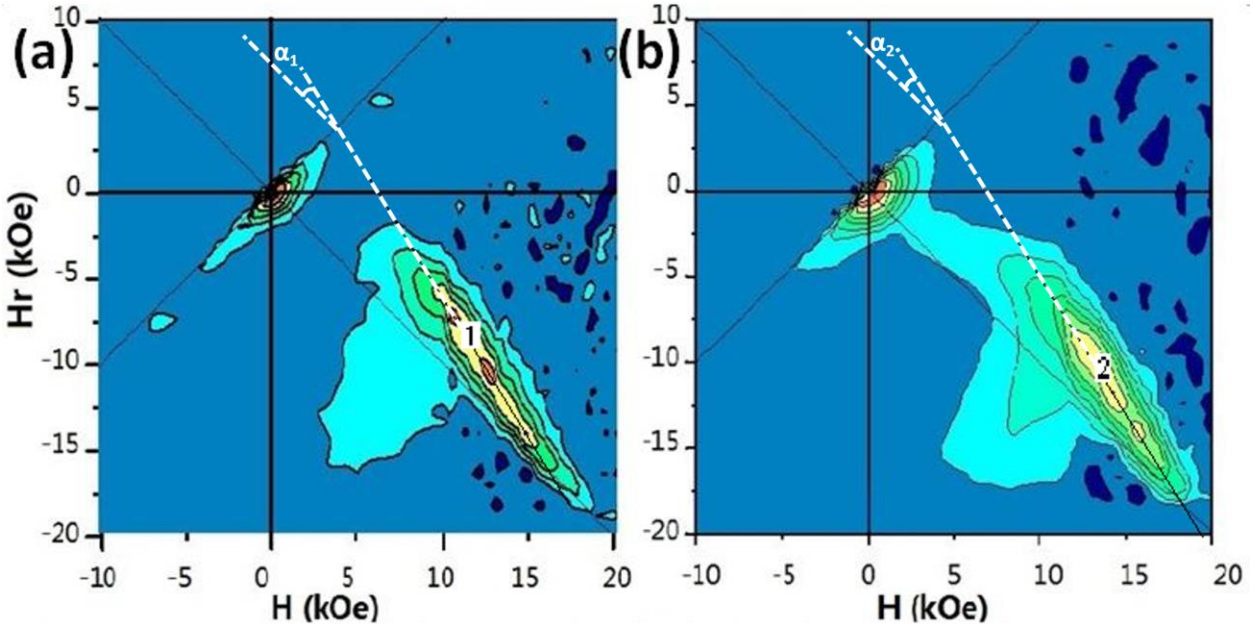

Fig 4.5 (a)&(b) Room temperature FORC diagram of S_{asgrn} and S_{ann}. The distinct separation between islands, representing the irreversible switching, is weakened after annealing, suggesting a sustained irreversible switching. In both diagrams, H_r represents the turning point that the minor loop $M(H)$ started. More details about the FORC diagram basics can be found in Appendix-1.

In conclusion, we fabricated high quality epitaxial $L1_0$ FePdPt films on MgO (001) substrate at 480 °C. We observed that Pt addition facilitates $L1_0$ chemical ordering. Sample post-annealed at 350 °C for 1h shows increased $L1_0$ ordering with no Ag diffusion observed from the capping layer. A weak coupling between soft/ hard phases is observed for the as-grown sample and it increases after annealing, as demonstrated by FORC diagrams. With perpendicular coercivity of 9.1 kOe, the $L1_0$ FePdPt system serves as a good candidate for magnetic recording media.

4.4 $L1_0$ FePt thin film

4.4.1 FePt film varying thickness

FePt thin film samples were prepared by ultra-high-vacuum ion beam sputtering (UHV-IBS) [D28] using a $Fe_{50}Pt_{50}$ (at.%) alloy target with a base pressure lower than 5×10^{-8} torr. Epitaxial $L1_0$ FePt films were deposited at a rate of 1.5 Å/sec onto MgO (001) single crystal substrate at 450 °C. *In situ* annealing (1h) at the growth temperature was performed right after the deposition. The combination of both the low deposition rate and *in situ* annealing ensures the crystalline quality and chemical ordering of the $L1_0$ FePt samples. The samples were then cooled down to room temperature and capped with a 3 nm-thick Au layer in the vacuum chamber to prevent any surface oxidation. Two samples in different thickness, 9 nm(S_1) and 15 nm(S_2) were fabricated.

Figure 4.6 shows the XRD θ-2θ scans for both samples. Both FePt (001) and (002) peaks were observed, indicating a good $L1_0$ ordering. Further, FePt (110) peak was found only in S_1, possibly due to the in-plane growth of *c*-axis at the MgO/ FePt interface during initial grain growth, where there is an 8.6% lattice mismatch between MgO and FePt [D33]. Moreover, the peak intensity ratio (I_{001}/I_{002}), a good indicator for $L1_0$ chemical ordering, saw an increase from S_1 to S_2, suggesting a better $L1_0$ ordering for thicker samples.

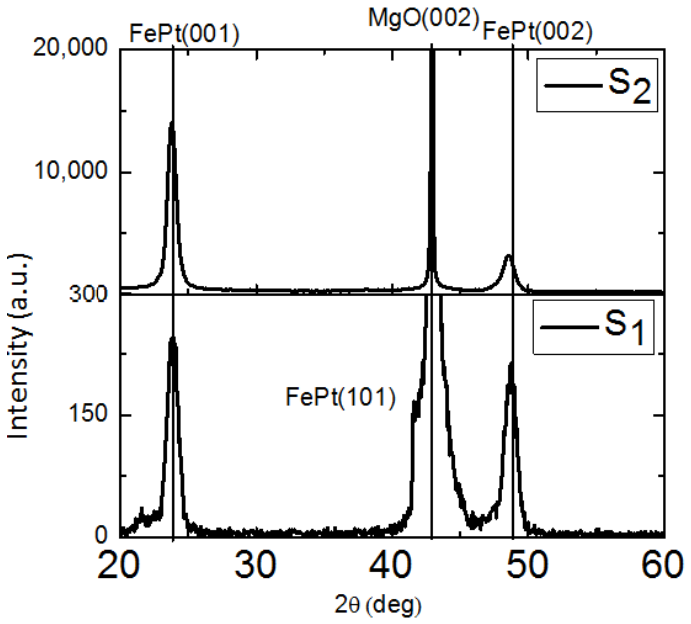

Fig 4.6 XRD θ-2θ scans of 2 samples varying thickness: 9 nm(S_1) and 15 nm(S_2).

Next, the thin film morphology and magnetic domain configuration were investigated, as shown in fig 4.7. We carried out MFM images for both S_1 and S_2 after a.c. demagnetization. First, maze-like pattern of magnetic domain was observed for S_2 [fig 4.7(b)] which is typical for PMA continuous film with strong exchange interaction facilitating domain wall motion [D34]. Magnetic domains broke into island-like pattern for thinner film (S_1), which is likely related to the pinning effect from grain boundaries or defects [D31]. The topological effects [D34] were also demonstrated by the AFM image [inset of fig 4.7(a)&(b)]; sample S_1 shows a granular topology while S_2 is a continuous film with smoother surface, with surface roughness of 0.21 nm. Thus, it is concluded that for thick FePt sample (S_2), the reversal process is facilitated by DW motion resulting in a dramatic reduction of coercivity; while topological pinning possibly takes place for the thinner sample.

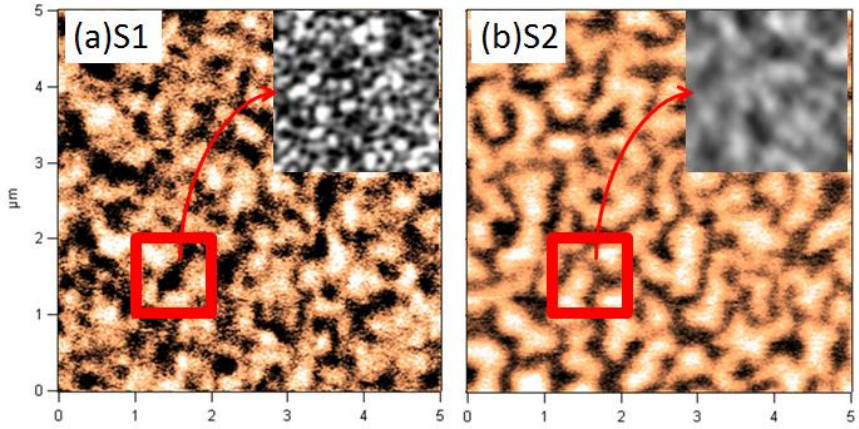

Fig 4.7 (a)&(b) MFM image of S_1 and S_2 after a.c. demagnetization. The black/white contrast suggests different phase in the MFM scan and hence the opposite polarity of the magnetic domains in the thin films. Insets of both images stand for AFM imaging probing the surface morphology with the surface roughness of 1.01 nm(S_1) and 0.21 nm(S_2), respectively. Scale is 5 μm for both figures and 1 μm for both insets.

4.4.2 FePt film varying lateral size

To examine the scaling behavior of the PMA system, especially when approaching *the single domain limit*, we fabricated nanodots arrays of epitaxial $L1_0$ FePt, fixing the thickness at 9 nm, with a series of lateral sizes to observe the transition from multi-domains to single domains.

First, nanodots arrays with diameter of 380 nm were fabricated using nanoimprint lithography (NIL) and post-patterned by ion milling from a 9 nm-thick epitaxial $L1_0$ FePt thin film (S_1). Figure 4.8(a) shows the SEM image of polymer resist pillars on top of FePt film before ion milling. The topology of FePt nanodots was studied by AFM, as shown in fig 4.8(c)&(d).

The large patterned area (0.5 cm×0.5 cm) allows detection of collective signal by VSM, as shown in fig 4.8(b). The coercivity, H_c, increases from 19 kOe to 27.8 kOe after patterning

and is attributed to the hampered domain wall motion. Further, we studied the magnetic configuration of the patterned dots, as will be shown in the next section.

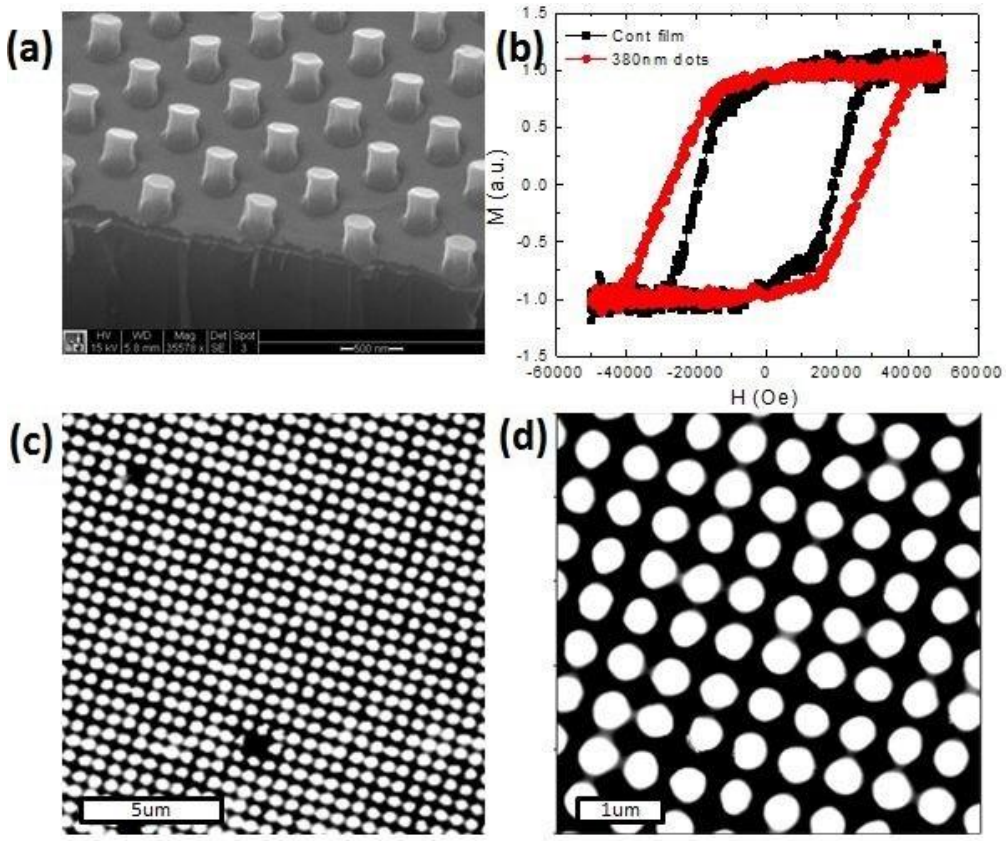

Fig 4.8 (a) SEM image of polymer resister pillars after nanoimprint. (b) Hysteresis loops of continuous film and 380 nm nanodots. (c)&(d) AFM images of patterned nanodots under different scale.

4.4.3 Multi-single domain transition

Next, we fabricated nanodots arrays with different sizes (440 nm, 260 nm and 150 nm) using focused ion beam (FIB). For each size, an area of 25 μm×25 μm was patterned. The design and the corresponding SEM image of the nanodots are shown in fig 4.9. Combined with the above NIL- patterned 380 nm dots array, they enable us to observe the multi-single domain transition for $L1_0$ FePt— that the magnetic domain configuration at remnant state within a

patterned dot would change from multiple domains to single domain, providing that its lateral size is smaller than the *single domain limit*. This transition was observed by magnetic force microscopy (MFM) and summarized in fig 4.10. For our 9 nm-thick $L1_0$ FePt films, this transition occurs for nanodots in size between 260 nm(d) and 150 nm(e), indicating *a single domain limit* around 200 nm. It is worth mentioning that this *single domain limit* of 200 nm is smaller than the theoretical prediction of 340 nm for bulk $L1_0$ FePt [Tab A1, section 1.2]. The defects (film deposition), shape effect (patterning) and edge damage (ion milling) coming from nanofabrication would lead to DW pinning, hampering the single domain formation. Moreover, decreased perpendicular anisotropy during thin film sample preparation would also possibly lead to a reduced *single domain limit*.

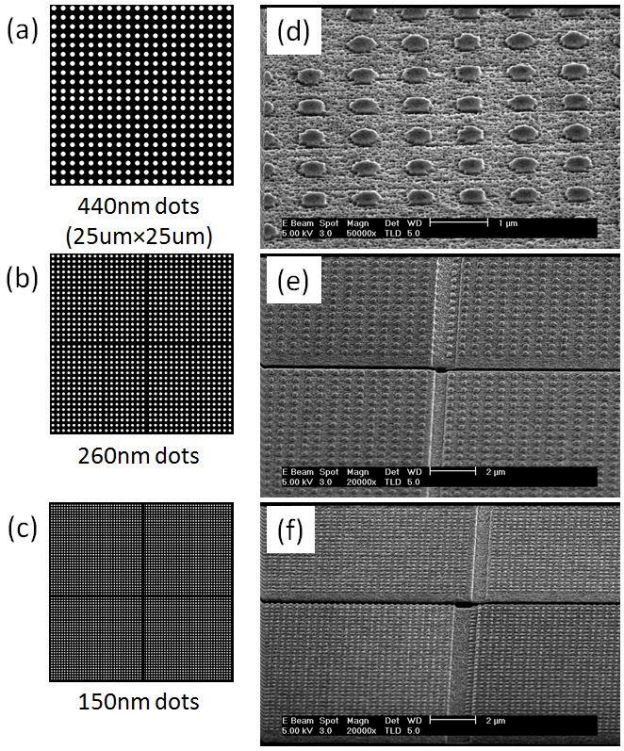

Fig 4.9 (a-c) Schematic and (d-f) SEM images of FIB-fabricated nanodots in size of 440 nm(d), 260 nm(e) and 150 nm(f), respectively. The patterned area is 25 μm×25 μm for all three samples.

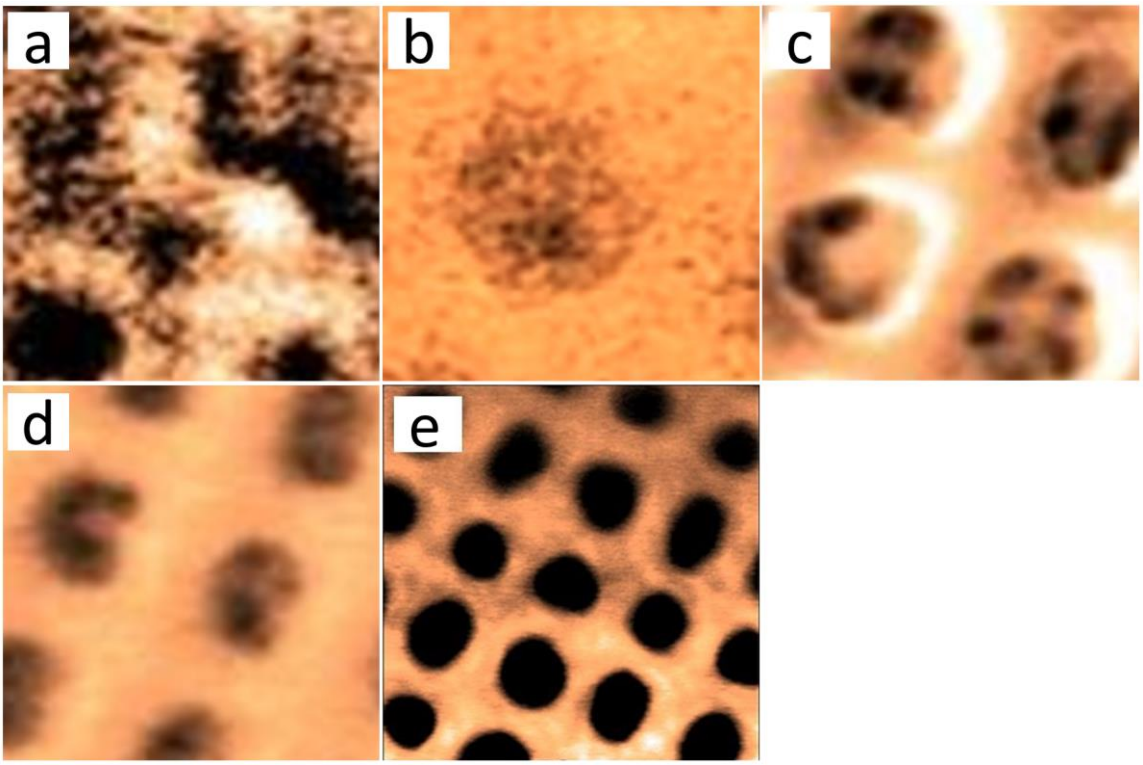

Fig 4.10 MFM images at remnant states showing the multi domain to single domain transition for our 9 nm-thick $L1_0$ FePt sample: (a) continuous film, (b-e) patterned nanodots in size of 440 nm, 380 nm, 260 nm and 150 nm, respectively. The scale of (a)-(e) is 1μm. Images (b)-(d) shows multiple magnetic domains within each dot, while image (e) shows single magnetic domain.

4.5 Sub-100 nm dots array & BPM recording

Based on the above discussion, it is of interest to assess the potential magnetic recording application of bit-patterned media (BPM). BPM requires lateral size of patterned dots to be within *the single domain limit*, so that the magnetization state of each dot can represent a bit information unambiguously. Here, we describe the fabrication of large-area (0.75 cm×0.75 cm) dots array using NIL combined with Molybdenum mask-transfer and ion milling. The sub-100 nm dots array shows high coercivity and is characterized by magnetic force microscopy (MFM)

and vibrating sample magnetometer (VSM). The magnetization reversal mechanism is studied by d.c. demagnetizing curves.

4.5.1 Nanofabrication of sub-100 nm dots array

Subsequent to the thin film deposition of 15 nm-thick $L1_0$ FePt thin film, as described above in section 4.4, large area patterning was carried out by nanoimprint lithography (NIL) using a Molybdenum mask-transfer lithography process. The transparent quartz master mold for NIL was bought from NTT-AT [D35]. It has nanodots array, with elements 100 nm in diameter, and a periodicity of 200 nm, on a total scale of 0.75 cm×0.75 cm. To extend the life of the master mold, daughter molds for subsequent NIL use were fabricated through duplication from the master mold using Ormostamp (Microresist Tech., GmBH)— a standard procedure developed by our group, which is discussed in detail elsewhere [D36]. The schematic of the NIL process is shown in fig 4.11(a)-(g) [D37-D39]. First, the desired heterostructures were deposited by UHV-IBS. Then, polymeric resist LOR1A (MicroChem Corp., Newton, MA) was spin-coated onto the sample surface for building the undercut profile, followed by thermal imprint resist 7010R (Microresist Tech., GmBH) coating. The thickness of the bilayer resist, *i.e.* LOR1A (90 nm) / 7010R (120 nm) [D40], was optimized for our feature size of sub-100 nm dots array. Next, the coated wafer was thermally imprinted in a Nanonex NX-B100 compact thermal imprinter at 200 psi / 120 °C for a duration of 60 s. Then, RIE dry etching was performed for 25 s followed by wet development (10 s) using TMAH for selectively etching the LOR1A and achieving the undercut, as shown in fig 4.11(h). Then, 20 nm-thick Molybdenum was deposited at room temperature for mask transfer before lift-off using Remover-PG [fig 4.11(i)]. Then, the sample was ion-milled in Ar plasma for 25 s to achieve isolated FePt dots. Finally, all Mo-residue on top

of the dots was removed by 30% H_2O_2. Figure 4.11(j) shows the morphology of the FePt dots array.

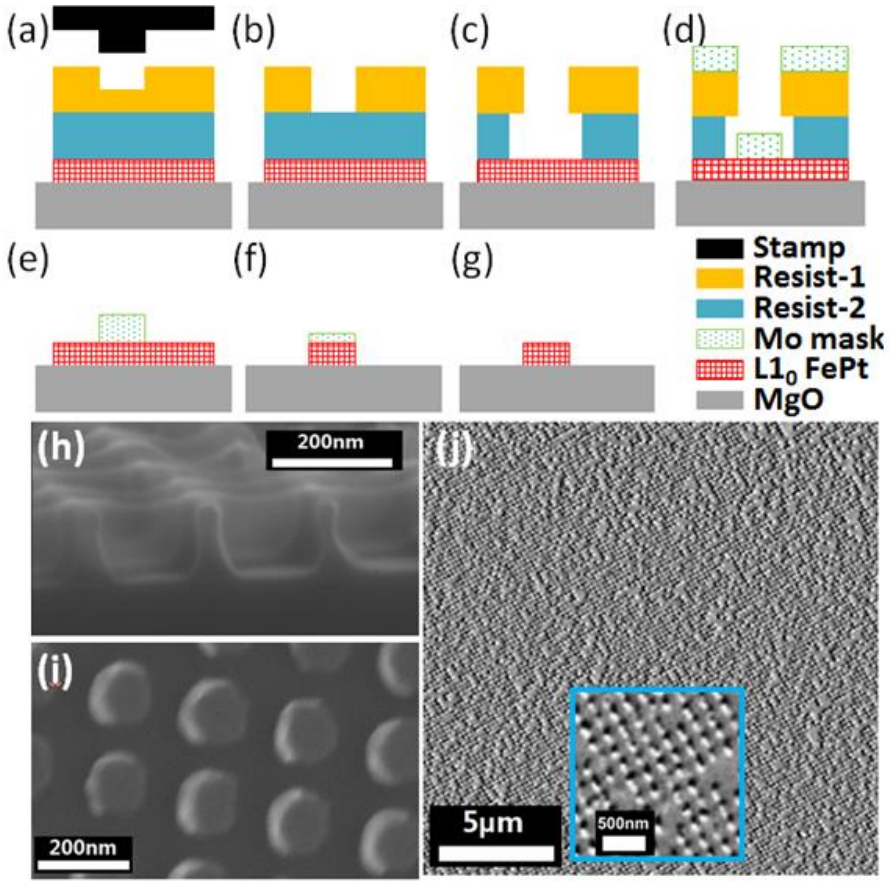

Figure 4.11 (a)-(g) Schematic of the nanofabrication process using nanoimprint lithography: (a) thermal imprinting, (b) RIE dry etching, (c) TMAH wet etching, (d) Mo deposition, (e) lift-off, (f) ion milling, and (g) Mo-residual removal by H_2O_2. (h) Cross-sectional SEM image of the bilayer resist undercut profile. (i) Top-down SEM of the Mo dots after resist lift-off. (j) AFM image of FePt dots array morphology.

The crystallographic structures of both film and dot samples were investigated by X-ray diffraction (XRD) θ-2θ scan using Cu K_α radiation. Magnetic measurements were performed on a Quantum Design® physical property measurement system (PPMS) using the VSM mode. The morphology of the samples was studied using scanning electron microscopy (SEM) and atomic

force microscopy (AFM). The magnetic microstructure was investigated by MFM using 100 nm CoCr coated high moment probes with a lift height of 40 nm.

4.5.2 Magnetic performance of sub-100 nm dots array

A large patterned area, > 0.75 cm×0.75 cm (same dimensions as the stamp), was achieved. The microscope image [inset in fig 4.12(a)] demonstrates the large area patterning. Next, we measured the dot-size distribution using a randomly-picked area of 10 μm ×10 μm, consisting of ~2500 dots, as shown in fig 4.12(a). The mean size of the dot diameter was analyzed to be 97.7 nm with a standard deviation, $\sigma = 8.3\%$, that is below the 10% threshold required for high density recording application [D41] [fig 4.12(b)]. The same analysis was also performed in another randomly-picked area, with similar results suggesting a consistency in the dot-size distribution. Additionally, it is worth mentioning that the dot size variation is largely attributed to Mo-deposition and lift-off [Fig 4.11(d)-(e)]. On the one hand, the sub-100 nm features are more sensitive to the sputtering process, which may introduce side-wall deposition resulting in defects during lift-off. The SEM image of a sample before Mo-deposition, as would be shown in fig 4.16(a), indicates a narrow dot size distribution, $\sigma = 1.13\%$, and suggests a good performance before Mo deposition. On the other hand, ion milling [fig 4.11(f)] does not change the dot size or shape except for the edge, which would not contribute much, considering the low height/diameter ratio of the nanodots in our samples. In conclusion, our NIL fabrication process of sub-100 nm dots array is suitable for high-density BPM owing to both large patterning area and good dot-size distribution.

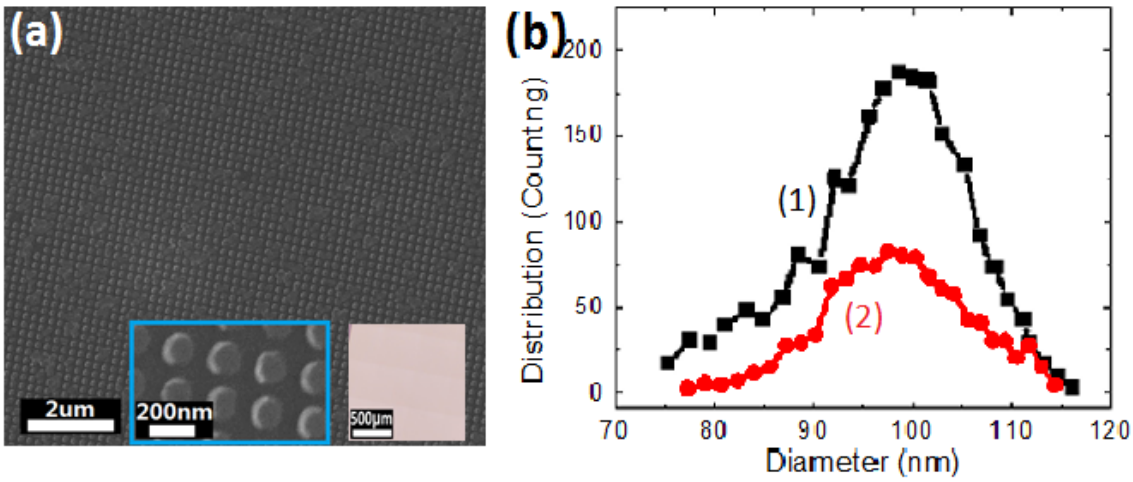

Fig 4.12 (a) SEM image of dots array before ion milling. (b) Dot size distribution (1) with average diameter of 97.7 nm. Inset of (a) shows both outline of the sub-100 nm dots and microscope image of the large area patterning. Curve-2 in (b) represents another randomly picked area showing the same result.

Figure 4.13 (a)&(b) shows the XRD θ-2θ scans for both film and dot samples. Clear FePt $L1_0$ (001) and (002) peaks were observed, in addition to the MgO (002) peak, indicating good chemical ordering. The peak intensity ratio (I_{001}/I_{002}), widely used as an indicator for the degree of $L1_0$ chemical ordering [D19], decreased after patterning (from 4.74 in thin film to 1.03 in nanodots), which is attributed to the processing in the nanofabrication and will be discussed later.

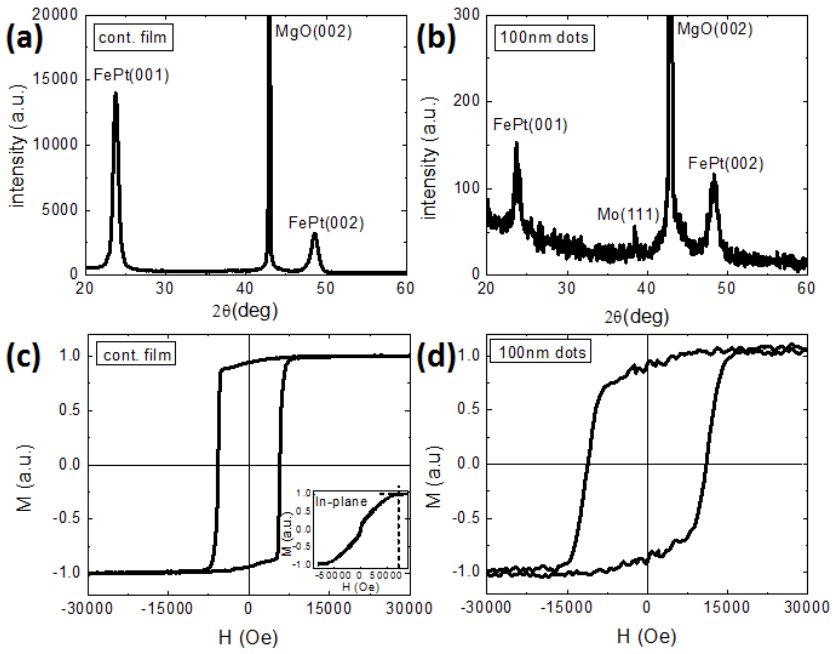

Fig 4.13 (a)&(b) XRD θ-2θ scan for both film/dots samples, showing clear $L1_0$ (001) and (002) peaks. Mo (111) peak was observed only in the dot sample (b), suggesting small amount of residual Mo after removal. (c)&(d) Hysteresis loops for both samples. An increased coercivity was observed for patterned dots array sample.

Next, hysteresis loop measurements were carried out, as shown in fig 4.13(c)&(d). For the film sample, a highly square loop is observed giving a coercivity value of H_c^{film} = 5.8 kOe. The sharp reversal process indicates a collective switching triggered by domain wall (DW) nucleation and propagation. To further confirm this argument, we studied the magnetic domain configuration at remnant states where the external field was applied and then removed before the characterization. After a.c. demagnetization, a maze-like domain pattern was observed using MFM [fig 4.14(a)], with balanced positive and negative magnetizations, which is typical for perpendicular magnetic anisotropy (PMA) system with strong in-plane exchange coupling [D42]. However, when an external field of 6 kOe was applied and then removed after saturation in the opposite direction, a significant expansion of the domains in the applied field direction was

observed [figure 4.14(b)]. Moreover, a close loop was observed with a saturation field of $H_{sat.inpl.}$ = 75 kOe when the field was applied parallel to the sample surface [inset of fig 4.14(c)]. This field, along the hard axis, is often referred to as anisotropy field [D43], H_a, and can be used to calculate the magnetic anisotropy constant, K_1. Based on H_a = 75 kOe and M_s =1140 emu/cc, we get $K_1 = 4.3 \times 10^7 \ {}^{erg}/_{cc}$ and $D_{sd} = 1.4\frac{4\sqrt{AK_1}}{{M_s}^2} = 275\ nm$ for our thin film sample, where D_{sd} is the single domain limit and A=10^{-6} erg/cm is the exchange stiffness. These results are in good agreement with the theoretical value of $K_1^{the.}$= 6.6×10^7 erg/cc and $D_{sd}^{the.}$= 340 nm for bulk $L1_0$ FePt [D14]; thus, our film sample showing high crystalline quality in thin film form is a good candidate for perpendicular magnetic recording (PMR). In short, we fabricated a high anisotropy $L1_0$ FePt film where the magnetic reversal is predominantly by domain wall motion, and indicates a strong in-plane exchange coupling.

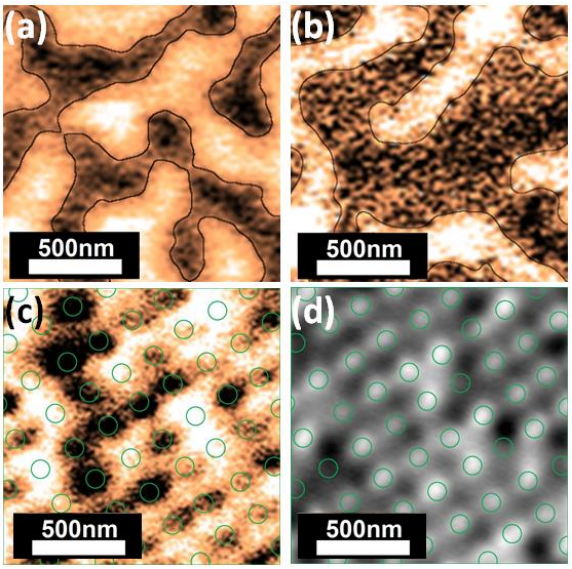

Fig 4.14 MFM image of the film sample at remnant states: (a) after a.c. demagnetization, and (b) when an external field out-of-plane in amplitude of 6 kOe was applied after saturation from the opposite direction. A clear domain wall expansion along the field direction is observed. For the dots array sample: (c) MFM image of dots array after a.c. demagnetization and (d) the corresponding AFM image showing the morphology of the patterned dots.

After NIL patterning, the sub-100 nm dots array showed almost double the coercivity, *i.e.* H_c^{dots} =11.1 kOe in the out-of-plane direction. This increased coercivity is attributed to patterning effect where the dots are within the single domain limit and therefore DW propagation, being energetically unfavorable, would be prohibited [D4]. This argument was confirmed by the MFM imaging. Figure 4.14(c)&(d) show the MFM image after a.c. demagnetization and corresponding AFM image of the dots array. The separate white/black regions indicate up/down magnetic domains, suggesting isolated nanodots after ion-milling. We surmise that this isolation breaks down the exchange coupling between dots and increases the coercivity. Next, it is worth discussing the potential integration of this sub-100 nm dots array into current recording mechanism. The head writing field has a theoretical upper limit of 24 kOe due to the intrinsic nature of pole material [D44]. In practice, owing to the head design and leakage of magnetic flux, this field could be even smaller [D45], and it is reasonable to assume the short-time head field to be 14 kOe [D46]. Nevertheless, the sub-100 nm dots array demonstrated here could fit well into the current writing capability in magnetic recording.

Ion milling has been reported to damage the crystalline structure at the dot surface due to Ar^+ ion bombardment [D5,D6], and cause a soft magnetic rim. This edge damage is expected in our dot sample, as suggested by the decreased peak intensity ratio (I_{001}/I_{002}) in the XRD data [fig 4.13(a)&(b)]. However, this damage will only contribute a very limited fraction of the soft phase to the high anisotropic volume and won't affect its performance [D10], given that the anisotropy field for the dot sample was measured to be as high as $H_a = H_{sat.inpl.}$ = 65 kOe, indicating $K_u = 3.7 \times 10^7 \, {}^{erg}/_{cc}$. In short, without sacrificing much of the magnetic stability by the edge damage introduced by ion milling, the high energy barrier for magnetic reversal is retained.

Additionally, it is of interest to discuss the film thickness and its influence on the magnetic properties. First, demagnetizing energy favors thicker sample with perpendicular anisotropy since magnetic "poles" on the top and bottom surface are further apart from each other. However, it cannot be too thick either. In addition to the cost considerations, a too-thick magnetic media would trigger incoherent reversal by thermally injecting a perpendicular DW into the column. Richter argued [D44] that the critical thickness, L_T, is determined by

$$E_{dw}=E_{coh} \quad \ldots\ldots(4.1)$$

where domain wall energy

$$E_{dw} = \pi D^2\sqrt{AK_u} \quad \ldots\ldots(4.2)$$

is comparable to the energy barrier for coherent rotation

$$E_{coh} = K_u(\frac{\pi}{4}D^2)L_T \quad \ldots\ldots(4.3)$$

where D is the dot diameter. However, besides the domain wall energy, the incoherent rotation would also generate another pair of magnetic poles and correspondingly increase the magnetostatic energy, E_{ms}. For our patterned dots with very low aspect ratio (L_T/D =15%), it is safe to assume that the out-of-plane demagnetizing factor $N_Z = 4\pi$ as the same to a thin film sample. Thus, we can rewrite the Eq 4.1 as

$$E_{dw} + \Delta E_{ms} = E_{coh} \ldots\ldots(4.4)$$

where

$$\Delta E_{ms} = 2\pi M_s^2 \left(\frac{\pi}{4}D^2\right) L_T \quad \ldots\ldots(4.5)$$

and calculate the critical thickness to be L_T=8.5 nm, which means a domain wall can be thermally injected when the patterned dots are thicker than 8.5 nm. It corresponds to an energy barrier required for a domain wall into a cylindrical grain

$$E_{barrier} = (E_{dw} + \Delta E_{ms})|_{L_T=8.5\,nm} = E_{coh}|_{L_T=8.5\,nm} = 2.47 \times 10^{-9} erg \quad \ldots\ldots(4.6)$$

To trigger the incoherent rotation from a thermal activation, an energy of $2.47 \times 10^{-9} erg$ that equals $6 \times 10^{4}(k_B T_0)$ is required, where k_B is the Boltzmann constant and T_0 is room temperature; this is unlikely to happen. Thus, the domain wall injection is not likely to take place for our 15 nm-thick dots array.

To further reveal the influence of patterning on the reversal process of film samples, we measured d.c. demag curves which, by measuring the remanence states, illustrates the direct-field demagnetization after saturation in a direction opposite to the applied field [D47]. As a result, the departure of the d.c. demag curve from the descending branch of the major hysteresis loop gives the reversible part of magnetic switching. As shown in fig 4.15(a)&(c), both thin film and NIL patterned samples show almost overlapping d.c. demag curves/major loops, indicating that irreversible switching dominates.

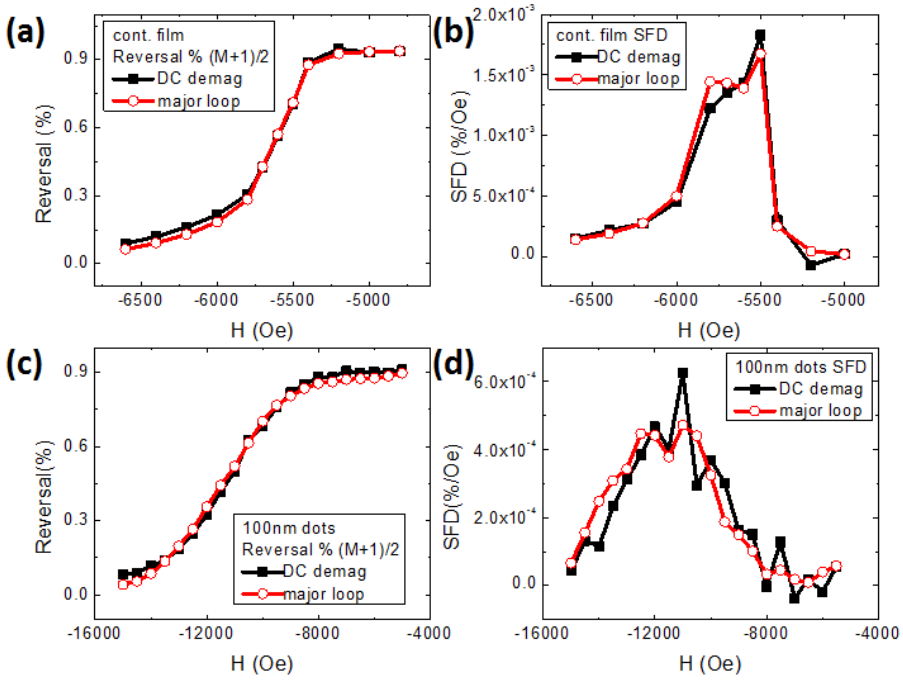

Fig 4.15 (a) Comparison of the descending branch of the major loop and the d.c. demag curve of the film sample and (b) first derivative, *dM/dH* of the both the d.c. demag curves and the descending branch of the hysteresis loops , to illustrate the switching field distribution. (c)&(d) the same set of measurements for the dots array sample.

Next, we carried out the first derivative, *dM/dH*, of both the d.c. demag curves and the descending branch of major loops. The difference is that M is measured at remnant state when the field is removed; while descending branch is measured continuously when the field is applied. More details can be found in Appendix-2. The *dM/dH* curves, usually employed to represent the switching field distribution (SFD), reveal the uniformity of magnetic switching within a system. As shown in fig 4.15(b)&(d), a slight difference in SFD was observed between the major curve and the d.c. demag curve in the case of both film and dot samples: the full-width-half-maximum (FWHM) drops from 460 Oe to 415 Oe for the film sample (9.8%) and from 4210 Oe to 3956 Oe for dot sample (6.0%). The less than 10% differences suggest that irreversible switching shows more collective behavior than the overall switching does, provided

that its complementary part, the reversible switching, was eliminated. Further, the small fraction of reversible switching can be attributed to the magnetostatic interactions between dots which causes a shallower loop with broadened SFD [D44] and can be partially released with the assistance of a soft under layer (SUL) [D10]. Second, compared to the thin film [fig 4.15(b)], the dots array [fig 4.15(d)] exhibits a very large increase in SFD; almost ten-time larger FWHM was observed in the patterned dots. This increase in SFD is a result of individual switching mechanism of the decoupled dots and processing-related defects, such as dots alignment issue from patterning and edge damage from ion milling [D5,D6]. Additionally, the expanded SFD could also possibly arise from the variation of K_1 in the film [D4], which could be extrinsically expressed if there is only one possible nucleation center per patterned dot [D7]. Thus, even though these results above are promising for BPM, a better uniformity in magnetic switching among isolated dots is highly desired, and the SFD for the patterned dots array should be further narrowed down to optimize the performance of the recording media.

One possible solution comes to the exchange coupled composite (ECC). As discussed in *chapter 1.6*, ECC media would reduce the overall switching field by introducing a soft magnetic layer, which switches first under a small external field and exerts a torque on the hard magnetic layer. Further, the soft layer usually shares the similar reversal field, and hence suggests a better uniformity in magnetic switching within the recording media. In the section below, we discuss the ECC patterning structure of FePt/Co bilayer system.

4.5.3 ECC patterning structure of FePt/Co bilayer system

To employ the exchange coupled composite (ECC) for the BPM application, we carried out exchange coupled hard/soft bilayer system of FePt/Co. For the bilayer system, a 13 nm-thick

$L1_0$ FePt serves as the hard layer, while the soft layer Co comes with varying thickness from 0 nm, 2 nm to 4 nm. The bilayer structure is demonstrated to reduce the switching field, H_{sw}, and its distribution (SFD) significantly by the introduction of soft magnetic material, Cobalt. Further, continuous films of the bilayer ECC structure were patterned down to sub-100 nm dots arrays by the nanofabrication process discussed above. Reduced coercivity and narrowing switching field distribution suggests a better control of discrete bits for the BPM recording device in real application.

ECC was originally inspired by the exchange spring phenomenon [D15], which states that when there are two phases within a magnetic element, a hard phase with high coercivity, H_c, and a soft phase with high saturation magnetization, M_s, they would interact with each other through interfacial exchange coupling; their different but coupled response to an external field would lead to magnetic moment rotation acting as a spring. From a magnetic recording point of view [D46], a bilayer ECC media would significantly reduce the required writing field, H_{wr}, without sacrificing much of the thermal energy barrier, ΔE, for the magnetic reversal. As a result, during the switching process, this property within the bilayer system would allow control of both thermal stability and writing field independently, resulting in a further reduction of the grain size in the granular-film recording media and enhancement of the perpendicular magnetic recording (PMR) density [D53].

The ECC structure is also attractive for BPM recording, for mainly two reasons. First, an ECC-BPM recording system would ensure writability for high areal density. As for BPM recording, the minimum writing field, H_{wr}, is determined by the energy barrier, ΔE, which is dependent on the geometrical size of the patterned element [D48]. Consequently, the physical areal density is limited by the writing capacity of the writing head. As discussed above, this issue

could be addressed by the ECC-BPM system [D49], where H_{wr} and ΔE are decoupled, ensuring higher areal density for the recording device. Second, from the application perspective, a narrow switching field distribution (SFD) of the BPM is critical to guarantee a precise and robust writing process for discrete bits [D50,D51]. The introduction of a soft magnetic material, Cobalt as in this thesis, would ensure it owing to its narrow intrinsic distribution of magnetic anisotropy [D4].

We have deposited thin film samples with a fixed 13 nm-thick $L1_0$ FePt serving as the hard layer, capped with a soft magnetic layer of Co, deposited at room temperature in order to prohibit diffusion, in different thickness (0, 2, and 4 nm). Corresponding to *section 4.5.2*, sub-100 nm dots array samples were fabricated to simulate the ECC-BPM system. Using a randomly picked up area of 13 µm× 10 µm, consisting of ~3200 dots, we measure the dot size distribution. The dots have an average diameter of 98.5 nm and standard deviation, σ = 8.48%, which is acceptable for BPM application, provided that the theoretical threshold of σ equals 10% [D41].

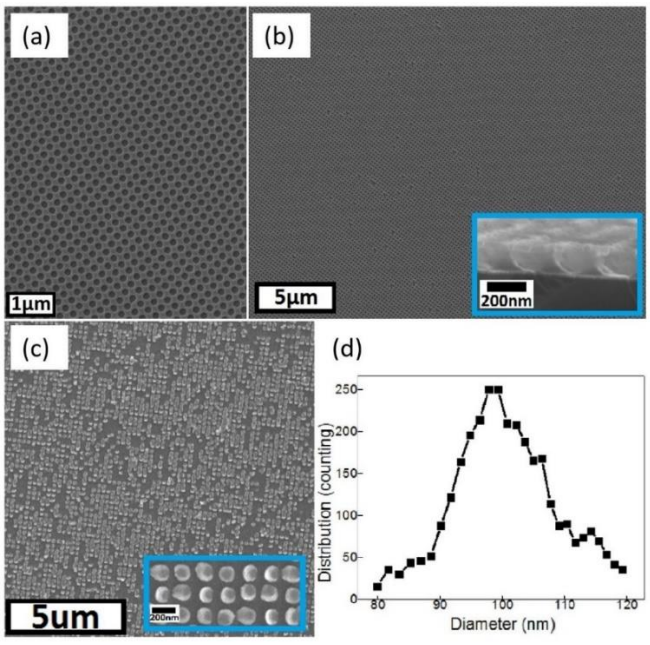

Fig 4.16 SEM image of the patterned dots array, (a)&(b) after imprint, [inset of(b)] after develop, and (c) before ion milling. (d) Dot size distribution with average diameter of 98.5 nm.

Hysteresis loop measurements were carried out for the samples. As shown in fig 4.17(a), top soft layer of Cobalt would help reduce the coercivity in the thin film samples; H_c drops dramatically from 18.1 kOe, 11.9 kOe to 2.8 kOe when Co thickness was varied from 0 nm, 2 nm to 4 nm, respectively. Additionally, it is worth mentioning that the coercivity of 18.1 kOe for the 13 nm-thick FePt monolayer dots array is largely different from that for the 15 nm-thick FePt dots array, 11.1 kOe, as previously discussed in *section 4.5.2*. This difference is attributed to the variation in both the overall magnetocrystalline quality and perpendicular anisotropy for $L1_0$ FePt with different thickness. Further, external factors related to the chamber condition during deposition, such as contamination, residual pressure and temperature stability, would all possibly contribute to a batch-to-batch difference in sample's quality and coercivity.

Besides, a narrowed switching field distribution (SFD) was achieved by the introduction of the top Co layer, as demonstrated by the first derivative of the descending branch of the hysteresis loop, *dM/dH* curve [fig 4.17(c)]. Both the reduced coercivity and the narrowed SFD are attributed to the interfacial exchange coupling between the $L1_0$ FePt layer and the top Co layer. As discussed in *chapter 1*, the external magnetic field first reverses the Co layer, which would exert a torque on the $L1_0$ FePt layer through exchanging coupling and hence facilitate the overall reversal. Thus, the coercivity drops correspondingly. Since the Co layer has a more uniform H_c distribution, a narrowed SFD is expected as well.

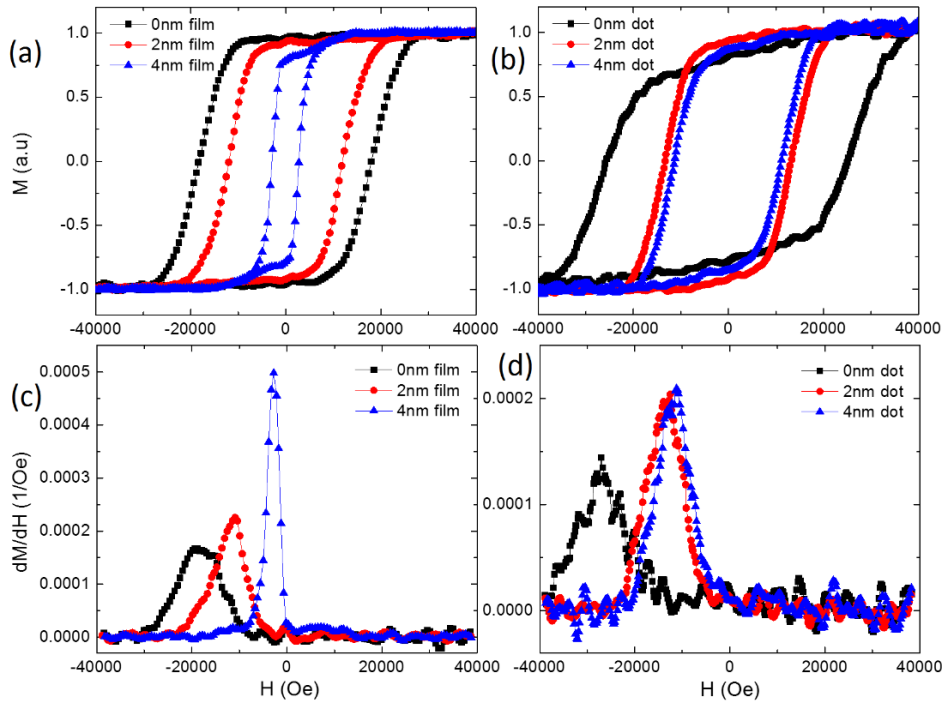

Fig 4.17 (a) Hysteresis loops for the thin film samples: FePt (13 nm)/Co (x nm), where x=0, 2, and 4. (c) First derivative *dM/dH* curves of the descending branch for each loop, representing the switching field distribution. (b)&(d) The corresponding loops and *dM/dH* curves for the sub-100 nm patterned-dots arrays.

For the sub-100 nm dots arrays, on the other hand, similar trends of both decreasing H_c and narrowing SFD were demonstrated with thicker Co in the bilayer structure as well. First, 2 nm-thick Cobalt on top of the $L1_0$ FePt layer would lead to a 48% H_c reduction from 25.4 kOe to 13.2 kOe. A further 2 kOe decrease was observed when the Co thickness was doubled to 4 nm, as shown in fig 4.18(b). Next, a narrow switching field distribution (SFD) of the patterned dots arrays was also observed; the full-width-at-half-maximum (FWHM) of the *dM/dH* curve drops 35% for the bilayer patterned dots array with 4 nm-thick Co layer. On the other hand, it is worth mentioning that both the drop in H_c and decrease in FWHM of the *dM/dH* curve are less when

we increased the Co layer thickness from 2 nm to 4 nm. This is possibly resulted from the patterning effect, where the domain wall motion within the soft phase is also hampered.

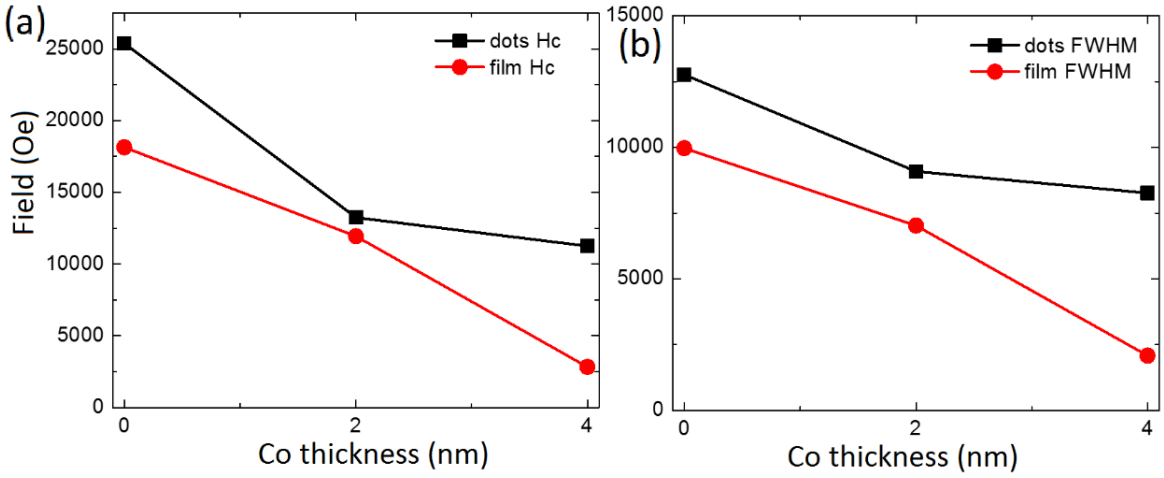

Fig 4.18 (a) Coercivity, H_c, dependence on the Co layer thickness for both thin film &patterned dot samples. (b) Corresponding switching field distribution (SFD) represented by the full-width-at-half-maximum (FWHM) of the *dM/dH* curves [corresponding to fig 4.17(c)&(d)]

In conclusion, we have fabricated sub-100 nm FePt dots array over a large patterning area. The thin film samples showed good $L1_0$ chemical ordering, and the reversal process was dominated by domain wall expansion. Sub-100 nm dots array from the $L1_0$ FePt film with good size uniformity was fabricated using nanoimprint lithography. A higher coercivity with a broadened switching field distribution (SFD) was observed in dots array samples. Further, the exchange coupled composite (ECC) structure of FePt/Co bilayer was demonstrated to both reduce the H_c and narrow down SFD significantly, facilitating a better control of discrete bits for the BPM recording device.

Chapter 5

CONCLUSIONS AND FUTURE WORK

In this thesis we have:

1) studied the angular dependence of switching field for magnetic elements within *the single domain limit*, and demonstrated control of the switching via dipole interaction;

2) established a 45° reversal clocking field mechanism for the MQCA logic, combined with shape-tuned elements array, to solve the misalignment issue;

3) demonstrated misalignment-free signal propagation in nanomagnet arrays and logic operation in majority gates based on this 45° mechanism;

4) developed a 3-input full adder based on 45°-clocking mechanism with the field altering between 0° and 45° off the x-axis to separate input writing and logic operation;

5) carried out thin film system of $L1_0$ FePd and FePt with high perpendicular magnetic anisotropy and coercivity;

6) studied the Pt ternary effect and the annealing effect on the chemical ordering and magnetic property of $L1_0$ FePd thin films;

7) investigated the multi-single domain transition of $L1_0$ FePt thin film using different types of patterning methods;

8) carried out sub-100 nm dots array of $L1_0$ FePt on a large area for the application of EEC-BPM recording.

This thesis provides a systematic study of the magnetism and interactions within *the single domain limit*, and discusses two examples of its most significant applications: MQCA logic and BPM recording. However, both of them requires further investigation before the idea becomes practically applicable.

To fulfill the ultimate goal of application of the MQCA logic, a good compatibility with the current CMOS technology is required, which may involve different integration mechanism. A robust reading/writing system, where the magnetic state of individual element can be electrically measured and altered independently, is strongly desired.

On the other hand, the application of bit-patterned media (BPM) requires more robust performance of the NIL patterned dots array with narrower dot size distribution and better magnetic property uniformity. Spin stand test using standard industrial reading/writing head would be desired.

Appendix-1

Advanced hysteresis loop measurements

1. FORC measurement

In this thesis, we employed first order reversal curve (FORC) measurements. By using a collection of minor loops, FORC diagram [E1] eliminates the reversible component in the magnetic switching process, and thus measures only the irreversible switching contribution. FORC diagram has been widely used as a visual 'fingerprint' to study the magnetic switching mechanism in different magnetic systems [E2][E3].

The first order reversal curve starts from the descending branch of the major loop for a magnetic system at a reversal field point, H_r, as shown in fig A1.1(a). Then, it departs from the major loop and measure the *M(H)* curve, where *M* and *H* are the magnetization and applied field, respectively. Since the curve is dependent on the turning point, H_r, it can be rewritten as $M(H, H_r)$. The data consists of a set of minor loops with different H_r [fig A1.1(b)&(c)].

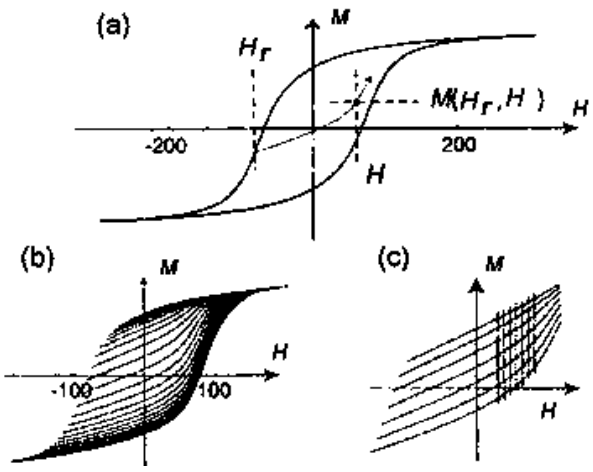

Fig A1.1 Schematic of the FORC diagram (adopted from ref E1). (a) After saturation in one direction, the FORC diagram starts from the turning point, H_r, and measures the minor loop. (b) A set of minor loops with different H_r, and forms (c) a 2-dimentional diagram for further analysis.

Next, the set of minor loops is assessed by some mathematical transformation. The FORC diagram is defined as the negative of the second derivative of M with respect to H_r and H; the 2-dimentional $M(H, H_r)$ diagram is interpreted as:

$$\rho(H_r, H) = -\frac{1}{2}\frac{\partial^2 M(H_r,H)}{\partial H_r \partial H} \quad \text{.....(A1.1)}$$

Then, $\rho(H_r, H)$ is plotted as a contour plot. Sometimes, it is convenient to rotate the coordinates by changing it from (H_r, H) to ($H_c = (H-H_r)/2$, $H_b = (H+H_r)/2$), where H_c and H_b represent coercivity and bias from magnetic interaction, respectively [E4]. When calculating the FORC distribution, a certain amount of numerical smoothing is inevitable. Further details on the measurement of a FORC diagram have been described elsewhere [E5-E6].

The interpretation of FORC diagram requires extensive knowledge on both the magnetic system and the nature of FORC diagram itself. In general, the magnetic response of a material

includes reversible and irreversible magnetizations; the FORC diagram does not capture the contribution of the reversible part, and hence enables us to purely study the irreversible switching process, as shown in *chapter 4.3.4*. Moreover, FORC is also used to establish the switching field distribution curve, which has the form of

$$\int(\partial^2 M(H_r, H)/\partial H_r \partial H)dH = dM(H_r)/dH_r \ldots\ldots \text{(A1.2)}$$

Even more sophisticated interpretation involves the Preisach model [E7], where the mean field interaction between grains within a system can be accurately determined.

2. D.C. demag curves

We also carried out *d.c. demag curves* in this thesis, which, by measuring the remnant state, illustrates the direct-field demagnetization after saturation opposite to the direction of the applied field [E8]. The departure of *d.c. demag curve* from the descending branch of the major loop gives the reversible part of magnetic switching. An overlapped *d.c. demag curve* and major loop indicate that irreversible magnetic switching dominates the reversal process. Fig A1.2 shows the schematic for the *d.c. demag curve*.

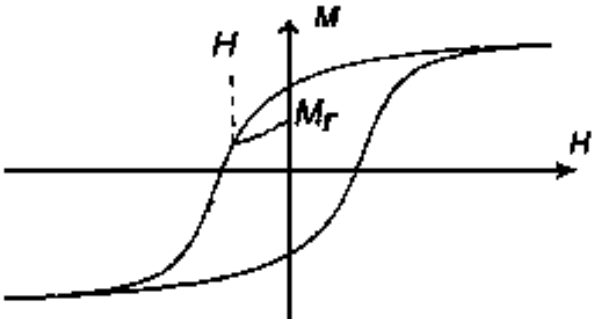

Fig A1.2 Schematic of the d.c. demag curve, $M_r(H)$, where H and Mr stands for the turning point of the minor loop and the remnant magnetization when the external field is removed.

Appendix-2

Standard operation procedure (SOP) for electron-beam lithography (EBL) of nanomagnet arrays

1. Sample preparation

1.1 Cut/clean wafer

1) Cut a piece of clean wafer in size of 1”×1”

2) Prebake the wafer under 180 ℃ for 2 min

3) Blow off the particles attached to the surface using Nitrogen, otherwise, there will be defects after spin coating

1.2 Spin coating

1) Spin coat the underlayer resist of LOR 1A using the recipe of [1500 ramp/4500 rpm/45 sec], which will give a uniform resist layer in thickness <100 nm

2) Bake the coated wafer under 180 ^{o}C for 10 min

3) Spin coat the EBL-resist of PMMA 3% using the recipe of [1500 ramp/4500 rpm/45 sec], which will give a uniform resist layer in thickness <90 nm

4) Bake the coated wafer under 180 ^{o}C for 90 sec

2. E-beam writing

2.1 Mount Sample

1) Scratch 4 corners of the wafer

2) Load 3 sample onto the SEM stage: Gold standard/ Ferriday Cup/ Coated wafer

3) Switch to "C" in the chamber mode, close the chamber door and pump down

4) Connect stage wire for EBL mode, open the nano-ampmeter and select picometer/ ZCHK

2.2 Software

1) Load the **.dc2* file and record the *max mag* of the file

[Rule of thumb: for the feature size of 1000 um×2000 um → max mag= 113]

2) Import the loaded file to the right folder, E:\NPGS\Projects\your name

3) Open the NPGS app, right click the **.dc2* file and hit *Run File Editor*

4) Select Yes/No/No/No in the main menu

5) Use the rule in the follow table to fill the parameters of the *Run file*:

Max mag	90% of the mm value recorded above
Center to Center/ Line Space	Minimum number available for highest accuracy/ limited by the spot size selection
Configuration #	Corresponding to the spot size in SEM configuration/ "1" indicates highest accuracy and lowest speed
Beam current	To be read later from ZCHK
Dose	0.3-1.3 nC/cm (PMMA, line dose) 30-250 uC/cm^2 (Man negative, area dose)

2.3 SEM focus

1) Set voltage as 30 kV, Spot size as 3

2) Confirm that the stage position is off the wafer, and Scan Rotation is zero

3) Start the electron beam

4) Focus under 2,000X using gold particle sample and then confirm the sample height

5) Change height to 6.5 mm using "go to" button

6) Focus under 2,000X and then confirm the sample height, AGAIN

7) Focus under 10,000X, following alignment and stigmation. The beam should be ready after these steps

8) Shift the beam to the Ferriday Cup and read the current using the nano-ampmeter, then write the reading into the runfile

[Rule of Thum: spot 1 gives 27 pA while spot 4 corresponds to 646 pA roughly]

2.4 Edges focus

1) Find the scratch on the wafer, then focus by ONLY rotating the z-knob clockwise under 8000X

[Rule of thumb, the optimized height should be around 5 mm]

2) Focus under 50,000X

3) Click magnification>>reference>>display

4) Click NPGS >>Command >>Direct stage control, then hit Enter / Enter / Space

5) Move to the 2nd edge of the wafer and focus, then hit Space

6) Move to the 3rd edge of the wafer and focus, then hit Space

7) Move to the 4^{th} edge of the wafer and focus, then hit Space / Enter

8) Check the RMS is smaller than 0.02, then hit Enter / Esc

2.5 Pre-writing

1) Open the beam blanker

2) Hit NPGS>>"Read WD", then hit Enter

3) Hit NPGS>>Commands>>Set Blanker>> beam on. The live image should show up

4) Hit NPGS>>Commands>>Set Blanker>> beam off. The live image should disappear

5) Hit Scan>>External XY, then hit NPGS>>Command>>Digital imaging>>New file

6) Hit acquire image. Should observe image. Then hit close>>yes (without saving)

7) Double check that the beam is blanked, move the stage to the center of the substrate

2.6 Writing

1) Hit NPGS>>command>>calibrate DACs and wait 40sec, then hit NPGS>> DAC [+3.6, +5.0]

2) Hit Run file>>process

2.7 Shut down SEM

1) Shut off the beam, lower the stage to height= 30, then hit Venting

2) Hit Mag>>Reference>>Videopoint, then switch the beam parameters to (5kV; spot 3; full frame)

3) Shut off the beam blanker, then removed the black cable connected to the SEM chamber

4) Turn off the picometer, open the chamber, switch the SEM to A mode

5) Unload the wafer, pump down the SEM chamber and then log off on computer

3. Develop

1) Use developer (3:1 MIBK:IPA) to soak the wafer for 70 sec then rinse it with water

2) Blow it dry with Nitrogen

3) Tune TMAH recipe for undercut structure to eliminate the side-wall deposition

[Rule of thumb: for feature size around 100 nm, 5 sec should be sufficient]

Appendix-3

Rutherford backscattering spectroscopy (RBS) and X-ray photoelectron spectroscopy (XPS) data of samples (S_{asgrn} and S_{ann})

1. RBS experimental methods:

The high-resolution RBS experiments were performed at the Environmental Molecular Sciences Laboratory (EMSL) in Pacific Northwest National Laboratory (PNNL), using National Electrostatic Corporation (NEC) 3MV Electrostatic Tandem Ion Accelerator with 2MeV He^{++} ions at 7° angle of incidence from the sample normal. Data were collected from a silicon surface barrier detector at a scattering angle of 150°. Data analysis was performed with the SIMNRA simulation code, where details of SIMNRA simulation in order to obtain atomic concentration and stoichiometry can be found in peer reviewed research papers [E9,E10].

2. Backscattering spectra results:

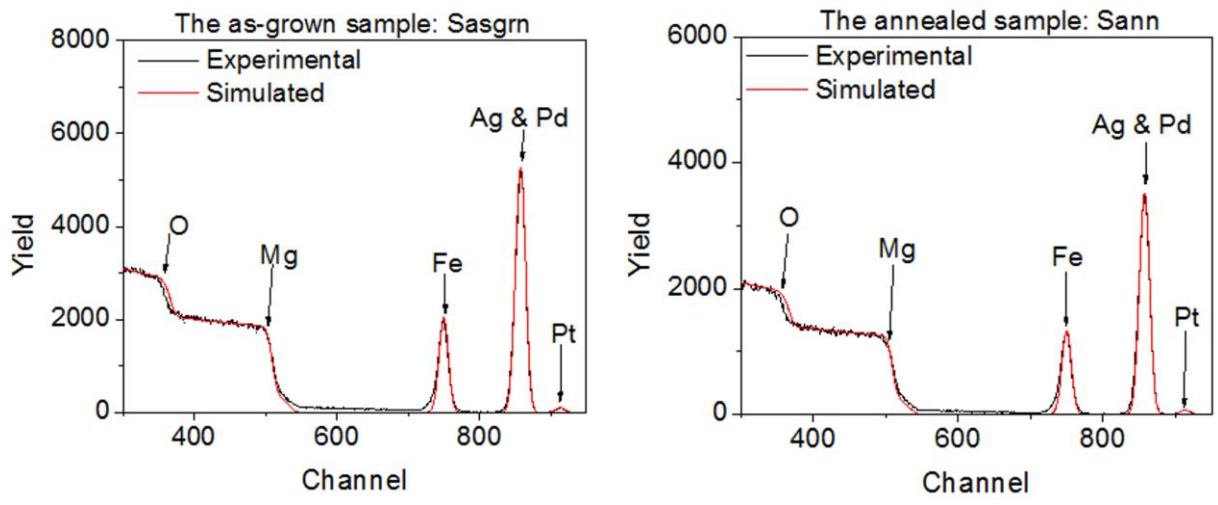

3. Simulated RBS results:

Samples ID		Elements					
Sample A as grown	**Thickness**	**Ag**	**Fe**	**Pd**	**Pt**	**O**	**Mg**
	(Atoms/cm2)	**%**	**%**	**%**	**%**	**%**	**%**
Layer 1 (1E15 Atoms/cm2)	1	100					
Layer 2 (1E15 Atoms/cm2)	15		20	30	0.05	49.95	
Layer 3 (1E15 Atoms/cm2)	15		16	45	0.05	38.95	
Layer 4 (1E15 Atoms/cm2)	30		11	36	0.05	52.95	
Layer 5 (1E15 Atoms/cm2)	40		33	16	0.15	50.85	
Layer 6 (1E15 Atoms/cm2)	40		35	10	0.17	54.83	
Layer 7 (1E15 Atoms/cm2)	50		28	22	0.25	49.75	
Layer 8 (1E15 Atoms/cm2)	100000000					50	50
Sample B Annealed	**Thickness**	**Ag**	**Fe**	**Pd**	**Pt**	**O**	**Mg**
	(Atoms/cm2)	**%**	**%**	**%**	**%**	**%**	**%**
Layer 1 (1E15 Atoms/cm2)	1	100					
Layer 2 (1E15 Atoms/cm2)	15		20	30	0.05	49.95	
Layer 3 (1E15 Atoms/cm2)	15		17	40	0.05	42.95	
Layer 4 (1E15 Atoms/cm2)	30		15	36	0.05	48.95	
Layer 5 (1E15 Atoms/cm2)	40		31	16	0.15	52.85	
Layer 6 (1E15 Atoms/cm2)	40		29.5	10	0.15	60.35	
Layer 7 (1E15 Atoms/cm2)	50		28	22	0.25	49.75	
Layer 8 (1E15 Atoms/cm2)	1000000000					50	50

4. XPS experiments and results:

The take-off angles (the angle between the sample normal and the input axis of the energy analyzer) were 0°, 30°, 60°, and 75°, corresponding to sampling depths of approximately 100, 75, 50, and 25 Å, respectively. The same measurements were carried out for both samples, S_{asgrn} and S_{ann}. Thus, it qualitatively represents the depth profile of Ag composition. For example, 0° data was measured where the X-ray beam penetrates the sample surface, where the least surface information was collected. On the other hand, beam at high angle (75°) interacts more with the sample surface and hence gives us more surface compositional information.

As shown in fig A3.2, both curves share a similar shape. Although there is a vertical shift, it is likely attributed to the background, which is inevitable. Given that, the Ag distribution along the normal direction should remain the same after annealing. Thus, we concluded that Ag is at least mostly at the surface.

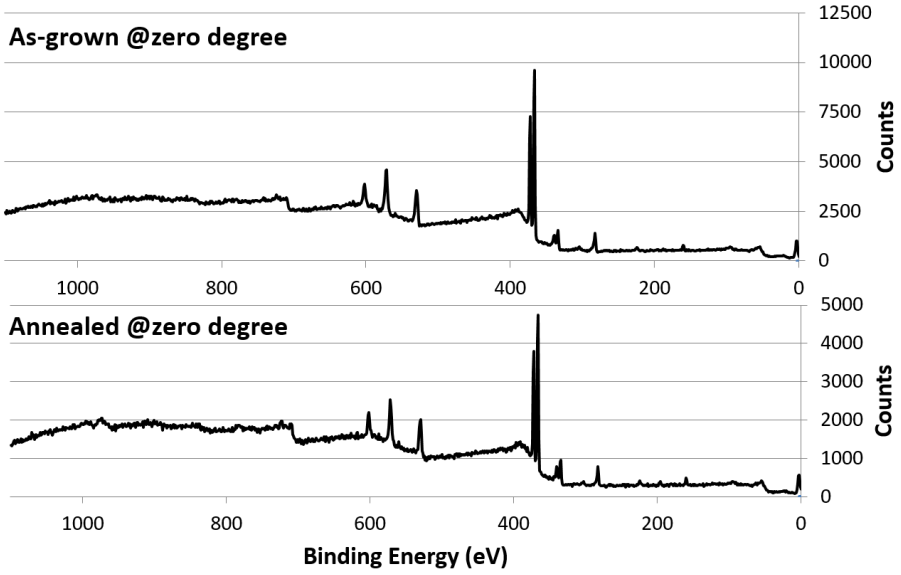

Fig A3.1 XPS data at 0° for both samples.

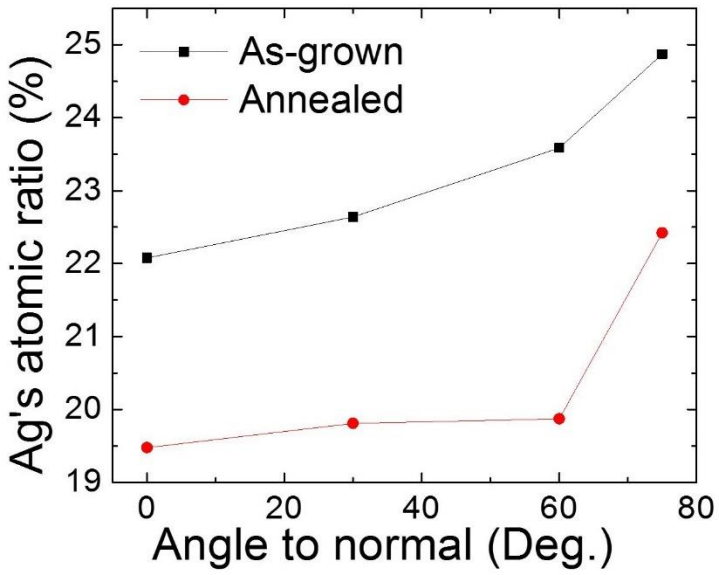

Fig A3.2 Curves of Ag's atomic ratio versus incident photon beam angle for bot samples.

Tab A3.1 The atomic percentage of all elements at 0° (normal) and 75° (glancing)

XPS Line	(as grown)		(annealed)	
Atom %	0°	75°	0°	75°
Fe 2p	6.8	5	8	5.5
O 1s	33.5	26.9	33.5	29.6
Ag 3d	22.1	24.9	19.5	22.4
Pd 3d	3.5	2.7	4	3.3
C 1s	34.1	40.5	35.1	39.2

Bibliography

*** Chapter 1 ***

[A1] K. Uchida, S. Takahashi, K. Harii, J. Ieda, W. Koshibae, K. Ando, S. Maekawa, E. Saitoh, "Observation of the spin Seebeck effect", *Nature* **455** 778 (2008)

[A2] Sarah M Thompson, "The discovery, development and future of GMR: The Nobel Prize 2007", *J. Phys. D: Appl. Phys.* **41** 093001 (2008)

[A3] SY Chou1, PR Krauss and PJ Renstrom, "Nanoimprint lithography", *J. Vac. Sci. Technol. B* **14** 4129 (1996)

[A4] G Srajer, LH Lewis, SD Bader, AJ Epstein, CS Fadley, EE Fullerton, A Hoffmann, JB Kortright, KM Krishnan, SA Majetich, TS Rahman, CA Ross, MB Salamon, IK Schuller, TC Schulthess, JZ Sun, "Advances in nanomagnetism via X-ray techniques", *J. Mag. Mag. Mat.* **307** 1 (2006)

[A5] Gerrit E. W. Bauer, Eiji Saitoh & Bart J. van Wees, "Spin caloritronics", *Nature Materials* **11** 391 (2012)

[A6] DA Allwood, G Xiong, CC Faulkner, D Atkinson, D Petit, RP Cowburn, "Magnetic Domain-Wall Logic", *Science* **309** 1688 (2005)

[A7] S. Y. Huang, X. Fan, D. Qu, Y. P. Chen, W. G. Wang, J. Wu, T. Y. Chen, J. Q. Xiao, and C. L. Chien, "Transport Magnetic Proximity Effects in Platinum", *Phys. Rev. Lett.* **109** 107204 (2012)

[A8] W. H. Meiklejohn, C. P. Bean, "New Magnetic Anisotropy", *Phys. Rev.* **105** 904 (1957)

[A9] S. S. P. Parkin, M. Hayashi and L. Thomas, “Magnetic Domain-Wall Racetrack Memory”, *Science* **320** 190 (2008)

[A10] N Thiyagarajah, S Bae, HW Joo, YC Han and J Kim, “Effects of perpendicular anisotropy on the interlayer coupling in perpendicularly magnetized [Pd/Co]/Cu/[Co/Pd] spin valves”, *Appl. Phys. Lett.* **92** 062504 (2008)

[A11] VD Nguyen, L Vila, A Marty, JC Pillet, L Notin, C Beigné, S Pizzini and JP Attané, “Dimensionality effects on the magnetization reversal in narrow FePt nanowires”, *Appl. Phys. Lett.* **100** 252403, (2012)

[A12] M Bowen, V Cros, F Petroff, A Fert, CM Boubeta, JL Costa-Krämer, JV Anguita, A Cebollada, F Briones, JM de Teresa, L Morellón, MR Ibarra, F Güell, F Peiró and A Cornet, "Large magnetoresistance in Fe/MgO/FeCo(001) epitaxial tunnel junctions on GaAs(001)". *Appl. Phys. Lett.* **79** 1655 (2001)

[A13] Y. Yafet, “Ruderman-Kittel-Kasuya-Yosida range function of a one-dimensional free-electron gas”, *Phys. Rev. B* **36** 3948 (1987)

[A14] J. Ping Liu, Eric Fullerton, Oliver Gutfleisch, David J. Sellmyer, “Nanoscale Magnetic Materials and Applications”, *Springer* (2010)

[A15] Gaussian unit system will be used consistently in this thesis and should not be mentioned later

[A16] P. Vavassori, V Bonanni, G. Gubbiotti, AO Adeyeye, S Goolaup and N Singh, “Cross-over from coherent rotation to inhomogeneous reversal mode in interacting ferromagnetic nanowires”, *J. Mag. Mag. Mat.* **316** e31 (2007)

[A17] T Klemmer, D Hoydick, H Okumura, B Zhang, and WA Soffa, “Magnetic hardening and coercivity mechanisms in $L1_0$ ordered FePd ferromagnets”, *Scr. Metall. Mater.* **33** 1793 (1995)

[A18] Amikam Aharoni, “Introduction to the Theory of Ferromagnetism”, *Oxford* (2001)

[A19] http://en.wikipedia.org/wiki/Stoner%E2%80%93Wohlfarth_model

[A20] A. Imre, G. Csaba, L Ji, A. Orlov, GH Bernstein and W. Porod, “Majority Logic Gate for Magnetic Quantum-Dot Cellular Automata”, *Science* **311** 205 (2006)

[A21] DB Carlton, NC Emley, E Tuchfeld and J Bokor, “Simulation studies of nanomagnet-based logic architecture”, *Nano Letters* **8** 4173 (2008)

[A22] T. Hesjedal and T. Phung, “Magnetic logic element based on an S-shaped Permalloy structure”, *Appl. Phys. Lett.* **96** 072501 (2010)

[A23] MT Niemier, E Varga, GH Bernstein, W Porod, MT Alam, A Dingler, A Orlov and XS Hu, “Shape Engineering for Controlled Switching With Nanomagnet Logic”, *IEEE Trans. Nanotech* **11** 220 (2012)

[A24] B Lambson, Z Gu, D Carlton, S Dhuey, A Scholl, A Doran, A Young and J Bokor, “Cascade-like signal propagation in chains of concave nanomagnets”, *Appl. Phys. Lett.* **100** 152406 (2012)

[A25] X Ju, MT Niemier, M Becherer, W Porod, P Lugli and G Csaba, “Systolic pattern matching hardware with out-of-plane nanomagnet logic devices”, *IEEE Trans. Nanotech.* **12** 399 (2013)

[A26] H. Cho, and E. E. Swartzlander, “Adder designs and analyses for quantum-dot cellular automata”, *IEEE Trans. Nanotech.* **6** 374 (2007)

[A27] Edit Varga, G. Csaba, G. H. Bernstein, and W. Porod, “Implementation of a nanomagnetic full adder circuit”, *IEEE nanotech conference on Nanotech.* (2011)

[A28] Edit Varga, Michael T. Niemier, Gyorgy Csaba, Gary H. Bernstein, and Wolfgang Porod, “Experimental realization of a nanomagnet full adder using slanted-edge magnets”, *IEEE Trans. Mag.* **49** 4452 (2013)

[A29] M.R.Scheinfein, LLG Micromagnetic Simulator™

[A30] A Moser, K Takano, DT Margulies, M Albrecht, Y Sonobe, Y Ikeda, SH Sun, and EE Fullerton, “Magnetic recording: advancing into the future”, *J. Phys. D* **35** R157 (2002)

[A31] HJ Richter, “Recent advances in the recording physics of thin-film media”, *J. Phys. D* **32** R147 (1999)

[A32] PF Carcia, AD Meinhaldt and A Suna, “Perpendicular magnetic anisotropy in Pd/Co thin film layered structures”, *Appl. Phys. Lett.* **47** 178 (1985)

[A33] S Hashimoto, Y Ochiai and K Aso, “Perpendicular magnetic anisotropy and magneto-striction of sputtered Co/Pd and Co/Pt multilayered films”, *J. Appl. Phys.* **66** 4909 (1989)

[A34] D Weller, H Brändle, G Gorman, CJ Lin and H Notarys, “Magnetic and magneto-optical properties of cobalt-platinum alloys with perpendicular magnetic anisotropy”, *Appl. Phys. Lett.* **61** 2726 (1992)

[A35] RH Victora and X Shen, “Composite media for perpendicular magnetic recording”, *IEEE Trans. Magn.* **41** 537 (2005)

[A36] KM Krishnan, “Fundamental and Applications of Magnetic Materials”, *Oxford* (2015)

[A37] T. Suzuki, “Perpendicular magnetic recording--Its basics and potential for the future”, *IEEE Trans. Mag.* **20**, 675 (1984)

[A38] D. Weller and A. Moser, *IEEE Trans. Magn*. **35** 4423 (1999)

[A39] Roger Wood, *IEEE Trans. Magn*. **36** 36 (2000)

[A40] T Shima, K Takanashi, YK Takahashi and K Hono, *Appl. Phys. Lett.* **81** 1050 (2002)

[A41] T Shima, K Takanashi, YK Takahashi and K Hono, *Appl. Phys. Lett.* **85** 2571 (2004)

[A42] A Perumal, YK Takahashi, TO Seki, and K. Hono, *Appl. Phys. Lett.* **92** 132508 (2008)

[A43] T Klemmer, D Hoydick, H Okumura, B Zhang and WA Soffa, *Scr. Metall. Mater.* **33** 1793 (1995)

[A44] JS Chen, BC Lim, JF Hu, B Liu, GM Chow and G Ju, *Appl. Phys. Lett*. **91** 132506 (2007)

[A45] H Bernas, JP Attané, KH Heinig, D Halley, D Ravelosona, A Marty, P Auric, C Chappert and Y Samson, *Phys. Rev. Lett.* **91** 077203 (2003)

[A46] Chih-Huang Lai, Cheng-Han Yang, and C. C. Chiang, *Appl. Phys. Lett.* **83** 4550 (2003)

[A47] SR Lee, S Yang, YK Kim, and JG Na, *Appl. Phys. Lett.* **78** 4001 (2001)

[A48] WY Zhang, H Shima, F Takano, H Akinaga, XZ Yu, T Hara, WZ Zhang, K Kimoto, Y Matsui, and S Nimori, *J. Appl. Phys.* **106** 033907 (2009)

[A49] Dustin A. Gilbert et al., *APL Mat.* **2** 086106 (2014)

[A50] CL Platt, KW Wierman, EB Svedberg, R van de Veerdonk, JK Howard, AG Roy and DE Laughlin, *J. Appl. Phys*. **92** 6104 (2002)

[A51] B. Wang and K. Barmak, *J. Appl. Phys.* **109** 123916 (2011)

[A52] S Jeong, A G. Roy, DE Laughlin and ME McHenry, *J. Appl. Phys*. **91** 8813 (2002)

[A53] M Ohtake, O Yabuhara K Tobari, F Kirino and M Futamoto, *J. Appl. Phys.* **109** 07B757 (2011)

[A54] T. Ichitsubo, S. Takashima, E. Matsubara, Y. Tamada, and T. Ono, *Appl. Phys. Lett.* **97** 182508 (2010)

[A55] JE Davies, O Hellwig, EE Fullerton, JS Jiang, SD Bader, GT Zimányi and K Liu, *Appl. Phys. Lett.* **86** 262503 (2005)

[A56] CI Dobrotă and A Stancu, *J. Appl. Phys.* **113** 043928 (2013)

[A57] H.J. Richter, *J. Phys. D. Appl. Phys.* **40** R149 (2007)

[A58] MH Kryder, EC Gage, TW McDaniel, WA Challener, RE Rottmayer, G Ju and MF Erden, *Proceedings of the IEEE* **96** 1810 (2008)

[A59] R. H. Vaictora and X. Shen, *IEEE Trans. Magn.* **41** 2828 (2005)

[A60] HJ Richter, AY Dobin, O Heinonen, KZ Gao, R. Veerdonk, RT Lynch and R Brockie, *IEEE Trans. Magn*. **42** 2255(2006)

[A61] K Srinivasan and SN Piramanayagam, 'chapter 4. Perpendicular recording media' in 'Developments in Data Storage: Materials Perspective', SN Piramanayagam and TC Chong, *John Wiley & Sons* (2011)

[A62] EADobisz, ZZ Bandić, Tsai-Wei Wu, 'Patterned Media: nanofabrication Challenges of Future Disk Drives', *Proceedings of the IEEE* **96** 1836 (2008)

[A63] T Thomson, G Hu and BD Terris, "Intrinsic Distribution of Magnetic Anisotropy in Thin Films Probed by Patterned Nanostructures", *Phys. Rev. Lett.* **96** 257204 (2006)

[A64] T. Bublat and D. Goll, *Nanotechnology* **22** 315301 (2011)

[A65] B. D. Terris and T. Thomson, *J. Phys. D. Appl. Phys.* **38** R199 (2005)

[A66] B.D. Terris, *J. Magn. Magn. Mater.* **321** 512 (2009)

[A67] S. Y. Chou, P. R. Krauss and P. J. Renstrom, *J. Vac. Sci. & Tech. B* **14** 4129 (1996)

[A68] LJ Guo, *Advanced Materials* **19** 495 (2007)

[A69] A Breitling, T Bublat and D Goll, *Physica Status Solidi (RRL)-Rapid Research Letters* **3** 130 (2009)

[A70] Q Dong, G Li, CL Ho, M Faisal, CW Leung, PWT Pong and WY Wong, *Advanced Materials* **24** 1033 (2012)

[A71] T. Bublat and D. Goll, *J. Appl. Phys.* **110** 073908 (2011)

*** Chapter 2 ***

[B1] M. Ohring, "Materials Science of Thin Films", *Elsevier Press* (2006)

[B2] R. Advincula and W. Knoll, "Functional Polymer Films", *Wiley* (2011).

[B3] B Lewis and JC Anderson, "Nucleation and Growth of Thin Films", *Academic Press* New York (1978)

[B4] DL Smith, "Thin film deposition, principles & practice", *McGraw-Hill INC* (1995)

[B5] M. Brünglinghaus, "Mean free path". *European Nuclear Society* (2011)

[B6] B Wolf, "Handbook of ion sources", *CRC Press* **pp.222** (1995)

[B7] Y Hou,Q Zhan and KM Krishnan "Magnetization reversal in exchange biased IrMn/Fe ring arrays", *Appl. Phys. Lett.* **98** 042510 (2011)

[B8] W Zhang, ME Bowden and KM Krishnan, "Competing effects of magnetocrystalline anisotropy and exchange bias in epitaxial Fe/IrMn bilayer", *Appl. Phys. Lett.* **98** 092503 (2011)

[B9] JJ Cuomo, SM Rossnagel and HR Kaufman, 'Handbook of ion beam processing technology, principles, deposition, film modification and synthesis', *Noyes Publications* (1989)

[B10] MA McCord and MJ Rooks, "SPIE Handbook of Microlithography", *Micromachining and Microfabrication* (2000)

[B11] *Microchem*, http://microchem.com/pdf/PMMA_Data_Sheet.pdf

[B12] *Microchem*, http://www.microchem.com/pdf/removerpg.pdf

[B13] SY Chou, PR Krauss, PJ Renstrom, "Imprint Lithography with 25-Nanometer Resolution", *Science* **272** 5258 (1996)

[B14] R Sbiaa and SN Piramanayagam, "Patterned Media Towards Nano-bit Magnetic Recording: Fabrication and Challenges", *Recent Patents on Nanotechnology* **1** 29 (2007)

[B15] W. Zhang and K. M. Krishnan, *J. Micromech. Microeng.* **24** 093001 (2014)

[B16] W Zhang, DN Weiss, KM Krishnan, *J. Appl. Phys.* **107** 09D724 (2010)

[B17] W Zhang, DN Weiss, KM Krishnan, *J. Microm. & Microe.* **21** 045024 (2011)

[B18] Jon Orloff, "Fundamental limits to imaging resolution for focused ion beams", *J. Vac. Sci. & Tech. B* **14** 3759 (1996)

[B19] GS Rohrer, "Structure and bonding in crystalline materials", *Cambridge University Press* (2001)

[B20] BE Warren, "X-ray diffraction", *Dover Publications Inc*. (1990)

[B21] H. Feng, "X-ray reflectivity studies of thin film", *Center for Materials for information Technology, University of Alabama, Tuscaloosa, AL* (2005)

[B22] JE Davies, O Hellwig, EE Fullerton, JS Jiang, SD Bader, GT Zimányi and K Liu, "Anisotropy dependence of irreversible switching in Fe/SmCo and FeNi/FePt exchange spring magnet films", *Appl. Phys. Lett.* **86** 262503 (2005)

[B23] CI Dobrotă and A Stancu, "What does a first-order reversal curve diagram really mean? A study case: Array of ferromagnetic nanowires", *J. Appl. Phys.* **113** 043928 (2013)

[B24] http://www.asylumresearch.com/ProbeStore/TIP_RADIUS?Entry=JustLooking

[B25] M Mayer (edit), "SIMNRA User's Guide", *Garching: Max-Planck-Institut fur Plasmaphysik* (2008)

[B26] CV Ramana, RJ Smith, OM Hussain, CC Chusuei, CM Julien, "Correlation between Growth Conditions, Microstructure, and Optical Properties in Pulsed-Laser-Deposited V_2O_5 Thin Films", *Chem. Mater.* **17** 1213 (2005)

[B27] A Aharoni, 'Introduction to the Theory of Ferromagnetism', *Oxford University Press* (2001)

[B28] J. Fidler, R. W. Chantrell, T. Schrefl, and M. A. Wongsam, *Elsevier Science* (2001)

[B29] HX Wei, FQ Zhu, XF Han, ZC Wen, and CL Chien, *Phys. Rev. B* **77** 224432 (2008)

[B30] G. Bertotti, 'Tutorial Session Notes: Micromagnetics and Nonlinear Magnetization Dynamics', *10th Biennal Conference on Electromagnetic Fields Computation*, Perugia (2002)

[B31] LD Landau, EM Lifshitz, 'Theory of the dispersion of magnetic permeability in ferromagnetic bodies', *Phys. Z. Sowietunion* **8** 153 (1935)

[B32] M.R.Scheinfein, LLG Micromagnetic Simulator™

[B33] More details about the software could be found at http://llgmicro.home.mindspring.com

[B34] J. Ping Liu, Eric Fullerton, Oliver Gutfleisch, David J. Sellmyer, "Nanoscale Magnetic Materials and Applications", *Springer* (2010)

*** Chapter 3 ***

[C1] A. Imre, G. Csaba, L. Ji, A. Orlov, G. H. Bernstein and W. Porod, "Majority Logic Gate for Magnetic Quantum-Dot Cellular Automata", *Science* **311** 205 (2006)

[C2] Amikam Aharoni, "Introduction to the Theory of Ferromagnetism", *Oxford* (2001)

[C3] André Thiaville, "Extensions of the geometric solution of the two dimensional coherent magnetization rotation model", *J. Magn. Magn. Mat.* **182** 5 (1998)

[C4] Zheng Li and Kannan M. Krishnan, "Highly stable signal propagation in a consecutively tuned nanomagnet array", *J. Appl. Phys.* **113** 17B901 (2013)

[C5] Zheng Li, Byung Seok Kwon and Kannan M. Krishnan, "Misalignment-free signal propagation in nanomagnet arrays and logic gates with 45°-clocking field", *J. Appl. Phys.* **115** 17E502 (2014)

[C6] M.R.Scheinfein, LLG Micromagnetic Simulator™

[C7] BS Kwon, W Zhang, Z Li, KM Krishnan, “Direct release of sombrero-shaped magnetite nanoparticles via nanoimprint lithography”, *Adv. Mater. Interfaces* **2** 1400511 (2015)

[C8] Xueming Ju, Michael T. Niemier, Markus Becherer, Wolfgang Porod, Paolo Lugli and Gyorgy Csaba, “Systolic pattern matching hardware with out-of-plane nanomagnet logic devices”, *IEEE Trans. Nanotech.* **12** 399 (2013)

[C9] H. Cho, and E. E. Swartzlander, “Adder designs and analyses for quantum-dot cellular automata”, *IEEE Trans. Nanotech.* **6** 374 (2007)

[C10] Xiaokuo Yang, Li Cai, Qiang Kang, Xiaohui Zhao, “Clocking misalignment tolerance of pipelined magnetic QCA architectures”, *Microelec. Journal* **43** 386 (2012)

[C11] Edit Varga, Michael T. Niemier, Gyorgy Csaba, Gary H. Bernstein, and Wolfgang Porod, “Experimental realization of a nanomagnet full adder using slanted-edge magnets”, *IEEE Trans. Mag.* **49** 4452 (2013)

[C12] MT Niemier , XS Hu, M Alam, G Bernstein, W Porod, M Putney, and J DeAngelis, “Clocking structures and power analysis for nanomagnet-based logic devices”, *Proc. of ISLPED* **pp.26** (2007)

[C13] RL Stamps et al, “The 2014 magnetism roadmap”, *J. Phys. D: Appl. Phys.* **47** 333001 (2014)

[C14] S. Bandyopadhyay and M. Cahay, “Electron spin for classical information processing: a brief survey of spin-based logic devices, gates and circuits”, *Nanotechnology* **20** 412001 (2009)

[C15] M. T. Niemier , X. S. Hu , M. Alam , G. Bernstein , W. Porod , M. Putney and J. DeAngelis, “Clocking structures and power analysis for nanomagnet-based logic devices”, *Proc. Int. Symp. Low Power Electron. Design* **26** (2007)

[C16] http://www.avtechpulse.com/

[C17] Mohmmad Tanvir Alam, Mohammad Jafar Siddiq, Gary H. Bernstein, Michael Niemier, Wolfgang Porod and Xiaobo Sharon Hu, “On-Chip Clocking for Nanomagnet Logic Devices”, *IEEE Trans. Nanotech.* **9** 348 (2010)

[C18] A. Lyle, A. Klemm, J. Harms, Y. Zhang, H. Zhao, and J.-P. Wang, “Probing dipole coupled nanomagnets using magnetoresistance read”, *Appl. Phys. Lett.* **98** 092502 (2011).

[C19] A. Lyle, J. Harms, T. Klein, A. Lentsch, D. Martens, A. Klemm, and JPWang, "Spin transfer torque programming dipole coupled nanomagnet arrays", *Appl. Phys. Lett.* **100** 012402 (2012)

[C20] J. Zhu, X. Chen, Q. Kang, B. Liu, L. Cai, and M. Zhang, "On-chip readout circuit for nanomagnetic logic", *IET Circuits, Devices Syst.* **8** 65 (2014)

[C21] Luqiao Liu, Chi-Feng Pai, Y. Li, HW Tseng, DC Ralph, RA Buhrman, "Spin-Torque Switching with the Giant Spin Hall Effect of Tantalum", *Science* **336** 555 (2012)

[C22] D. Bhowmik, L. You, and S. Salahuddin, "Spin Hall effect clocking of nanomagnetic logic without a magnetic field", *Nat. Nanotechnol.* **9** 59 (2014)

*** Chapter 4 ***

[D1] Kevin R. Coffey, Thomas Thomson and Jan-Ulrich Thiele, "Angle dependent magnetization reversal of thin film magnetic recording media", *J. Appl. Phys.* **93** 8471 (2003)

[D2] G. Hu, T. Thomson, C. T. Rettner, S. Raoux and B. D. Terris, "Magnetization reversal in Co/Pd nanostructures and films", *J. Appl. Phys.* **97** 10J702 (2005)

[D3] S. P. Li, A. Lebib1, Y. Chen, Y. Fu, and M. E. Welland, *J. Appl. Phys.* **91** 9964 (2002)

[D4] T. Thomson, G. Hu, and B. D. Terris, "Intrinsic Distribution of Magnetic Anisotropy in Thin Films Probed by Patterned Nanostructures", *Phys. Rev. Lett.* **96** 257204 (2006)

[D5] JW Lau, X Liu, RC Boling, JM Shaw, "Decoupling nucleation and domain-wall propagation regimes in (Co/Pd)n multilayer nanostructures", *Phys. Rev. B* **84** 214427 (2011)

[D6] Justin M. Shaw, Miles Olsen, June W. Lau, Michael L. Schneider, T. J. Silva, Olav Hellwig, Elizabeth Dobisz, and Bruce D. Terris, "Intrinsic defects in perpendicularly magnetized multilayer thin films and nanostructures", *Phys. Rev. B* **82** 144437 (2010)

[D7] J.-P. Jamet, S. Lemerle, P. Meyer, J. Ferré, B. Bartenlian, N. Bardou, C. Chappert, P. Veillet, F. Rousseaux, D. Decanini, and H. Launois, "Dynamics of the magnetization reversal in Au/Co/Au micrometer-size dot arrays", *Phys. Rev. B* **57** 14320 (1998)

[D8] A. Moser, K. Takano, D. T. Margulies, M. Albrecht, Y. Sonobe, Y. Ikeda, S. H. Sun, and E. E. Fullerton, "Magnetic recording: advancing into the future", *J. Phys. D* **35** R157 (2002)

[D9] H. J. Richter, "Recent advances in the recording physics of thin-film media", *J. Phys. D* **32** R147 (1999)

[D10] R. H. Victora and X. Shen, "Composite media for perpendicular magnetic recording", *IEEE Trans. Magn.* **41** 537 (2005)

[D11] T. Shima, K. Takanashi, Y. K. Takahashi, and K. Hono, "Preparation and magnetic properties of highly coercive FePt films", *Appl. Phys. Lett.* **81** 1050 (2002)

[D12] T. Shima, K. Takanashi, Y. K. Takahashi, and K. Hono, "Coercivity exceeding 100kOe in epitaxially grown FePt sputtered films", *Appl. Phys. Lett.* **85** 2571 (2004)

[D13] A. Perumal, Y. K. Takahashi, T. O. Seki, and K. Hono, "Particulate structure of L10 ordered ultrathin FePt films for perpendicular recording", *Appl. Phys. Lett.* **92** 132508 (2008)

[D14] T Klemmer, D Hoydick, H Okumura, B Zhang, and WA Soffa, "Magnetic hardening and coercivity mechanisms in $L1_0$ ordered FePd ferromagnets", *Scr. Metall. Mater.* **33** 1793 (1995)

[D15] E. F. Kneller and R. Hawig, "The exchange-spring magnet: a new material principle for permanent magnets", *IEEE Trans. Mag.* **27** 3588 (1991)

[D16] SR Lee, S Yang, YK Kim, and JG Na, "Rapid ordering of Zr-doped FePt alloy films", *Appl. Phys. Lett.* **78** 4001 (2001)

[D17] Tomoyuki Maeda, Tadashi Kai, Akira Kikitsu, Toshihiko Nagase, and Jun-ichi Akiyama, "Reduction of ordering temperature of an FePt-ordered alloy by addition of Cu", *Appl. Phys. Lett.* **80** 2147 (2002)

[D18] W. Y. Zhang, H. Shima, F. Takano, H. Akinaga, X. Z. Yu, T. Hara, W. Z. Zhang, K. Kimoto, Y. Matsui, and S. Nimori, "Enhancement in ordering of Fe50Pt50 film caused by Cr and Cu additives", *J. Appl. Phys.* **106** 033907 (2009)

[D19] CL Platt, KW Wierman, EB Svedberg, RVD Veerdonk, JK Howard, AG Roy, and DE Laughlin, "$L1_0$ ordering and microstructure of FePt thin films with Cu, Ag, and Au additive", *J. Appl. Phys.* **92** 6104 (2002)

[D20] B. Wang and K. Barmak, "Re-evaluation of the impact of ternary additions of Ni and Cu on the A1 to $L1_0$ transformation in FePt films", *J. Appl. Phys.* **109** 123916 (2011)

[D21] SK Jeong, AG Roy, DE Laughlin, and ME McHenry, "Nanostructure and magnetic properties of polycrystalline FePdPt/MgO thin films", *J. Appl. Phys.* **91** 8813 (2002)

[D22] M. Ohtake, O. Yabuhara, K. Tobari, F. Kirino, and M. Futamoto, "Structure and magnetic properties of FePd-alloy epitaxial thin films grown on MgO single-crystal substrates with different orientations", *J. Appl. Phys.* **109** 07B757 (2011)

[D23] T. Ichitsubo, S. Takashima, E. Matsubara, Y. Tamada, and T. Ono, "Exchange-coupling of c-axis oriented L10–FePd and Fe in FePd/Fe thin films", *Appl. Phys. Lett.* **97** 182508 (2010)

[D24] Joseph E. Davies, Olav Hellwig, Eric E. Fullerton, J. S. Jiang, S. D. Bader, G. T. Zimányi and Kai Liu, "Anisotropy dependence of irreversible switching in Fe/SmCo and FeNi/FePt exchange spring magnet films", *Appl. Phys. Lett.* **86** 262503 (2005)

[D25] CI Dobrotă and A Stancu, "What does a first-order reversal curve diagram really mean? A study case: Array of ferromagnetic nanowires", *J. Appl. Phys.* **113** 043928 (2013)

[D26] W Zhang, ME Bowden, and KM Krishnan, "Competing effects of magnetocrystalline anisotropy and exchange bias in epitaxial Fe/IrMn bilayers", *Appl. Phys. Lett.* **98** 092503 (2011)

[D27] Zheng Li and Kannan M. Krishnan, "Highly stable signal propagation in a consecutively tuned nanomagnet array", *Jour. Appl. Phys.* **113** 17B901 (2013)

[D28] W.B. Pearson, "A handbook of lattice spacings and structures of metals and alloys", *Pergamon Press* (1967)

[D29] ZL Zhao, JS Chen, J Ding, JB Yi, BH Liu, and J. P. Wang, "Fabrication and microstructure of high coercivity FePt thin films at 400 °C", *Appl. Phys. Lett.* **88** 052503 (2006)

[D30] See Appendix-3 for RBS raw data of both samples (S_{asgrn} and S_{ann})

[D31] S. Okamoto, N. Kikuchi, O. Kitakami, T. Miyazaki, and Y. Shimada, and K. Fukamichi, *Phys. Rev. B* **66** 024413 (2002)

[D32] A. Stancu, C.Pike, L. Stoleriu, P. Postolache and D. Cimpoesu, "Micromagnetic and Preisach analysis of the first order reversal curves (FORC) diagram", *J. Appl. Phys.* **93** 6620 (2003)

[D33] D. Goll and A. Breitling, "Coercivity of ledge-type L10-FePt/Fe nanocomposites with perpendicular magnetization", *Appl. Phys. Lett.* **94** 052502 (2009)

[D34] T Suzuki, K Harada, N Honda and K Ouchi, "Preparation of ordered Fe-Pt thin films for perpendicular magnetic recording media", *J. Magn. Magn. Mat.* **193** 85 (1999)

[D35] www.ntt-at.com/product/Nanoimprint_custom

[D36] W. Zhang and K. M. Krishnan, *J. Micromech. Microeng.* **24** 093001 (2014)

[D37] W Zhang, DN Weiss, KM Krishnan, *J. Appl. Phys.* **107** 09D724 (2010)

[D38] BS Kwon, Z Li, W Zhang, KM Krishnan, *J. Appl. Phys.* **115** 17B506 (2014)

[D39] BS Kwon, W Zhang, Z Li, KM Krishnan, *Adv. Mater. Interfaces* **2** 1400511 (2015)

[D40] W Zhang, DN Weiss, KM Krishnan, *J. Microm. & Microe.* **21** 045024 (2011)

[D41] B.D. Terris, *J. Magn. Magn. Mater.* **321** 512 (2009)

[D42] G.Q. Li, H.Takahoshi, H.Ito, H.Saito, S.Ishio, T.Shima and K.Takanashi, *J. Appl. Phys.* **94** 5672 (2003)

[D43] D.Mauri, H.C.Siegmann, P.S.Bagus and E. Kay, *J. Appl. Phys.* **62** 3047(1987)

[D44] H J Richter, "*The transition from longitudinal to perpendicular recording*", *J. Phys. D: Appl. Phys.* **40** R149 (2007)

[D45] through discussion with Dr. Bruce Terris.

[D46] Rok Dittrich, Guohan Hu, Thomas Schrefl, Thomas Thomson, Dieter Suess, Bruce D. Terris, and Josef Fidler, *J. App. Phys.* **97** 10J705 (2005)

[D47] D. Eckert, *J. Magn. Magn. Mater* **83** 197 (1990)

[D48] D Suess, T Schrefl, S Fähler, M Kirschner, G Hrkac, F Dorfbauer, and J Fidler, 'Exchange spring media for perpendicular recording', *Appl. Phys. Lett.* **87** 012504 (2005)

[D49] S Okamoto, O Kitakami, N Kikuchi, T Miyazaki, Y Shimada, and T Chiang, *J. Phys.: Condens. Matter* **16** 2109 (2004)

[D50] D. Suess, *Appl. Phys. Lett.* **89** 113105 (2006)

[D51] P Krone, D Makarov, T Schrefl, and M Albrecht, ‘Exchange coupled composite bit patterned media’, *Appl. Phys. Lett.* **97** 082501 (2010)

[D52] M Albrecht, CT Rettner, A Moser, ME Best, and BD Terris, Appl.Phys. Lett. 81 2875 (2002)

[D53] M Grobis, E Dobisz, O Hellwig, ME Schabes, G Zeltzer, T Hauet, and TR Albrecht, Appl. Phys. Lett. 96 052509 (2010)

*** Appendix 1 ***

[E1] Andreas Neudert, Jeffrey McCord, Dmitry Chumakov, Rudolf Schäfer, and Ludwig Schultz, *Phys. Rev. B* **71** 134405 (2005)

[E2] Joseph E. Davies, Olav Hellwig, Eric E. Fullerton, J. S. Jiang, S. D. Bader, G. T. Zimányi and Kai Liu, “Anisotropy dependence of irreversible switching in Fe/SmCo and FeNi/FePt exchange spring magnet films”, *Appl. Phys. Lett.* **86** 262503 (2005)

[E3] CI Dobrotă and A Stancu, “What does a first-order reversal curve diagram really mean? A study case: Array of ferromagnetic nanowires”, *J. Appl. Phys.* **113** 043928 (2013)

[E4] CR Pike, CA Ross, RT Scalettar, and G Zimanyi, "First-order reversal curve diagram analysis of a perpendicular nickel nanopillar array", *Phys. Rev. B* **71** 134407 (2005)

[E5] A. Markou, I. Panagiotopoulos, T. Bakas, P. Postolache, L. Stoleriu *et al*, *J. Appl. Phys.* **112** 123914 (2012)

[E6] Costin-Ionuţ Dobrotă and Alexandru Stancu, *J. Appl. Phys.* **113** 043928 (2013)

[E7] A. Stancu, C. Pike, L. Stoleriu, P. Postolache and D. Cimpoesu, “Micromagnetic and Preisach analysis of the first order reversal curves (FORC) diagram”, *J. Appl. Phys.* **93** 6620 (2003)

[E8] D. Eckert, *J. Magn. Magn. Mater* **83** 197 (1990)

[E9] M Mayer (edit), “SIMNRA User’s Guide”, *Garching: Max-Planck-Institut fur Plasmaphysik* (2008)

[E10] C Ramana, R Smith, O Hussain, C Chusuei, C Julien, *Chem. Mater.* **17** 1213 (2005)